

A critical look at low-scale cosmological phase transitions in the PTA era

Simone Biondini^{a,*} and Philipp Schicho^{b,†}

^a*Institute of Physics, University of Freiburg,
Hermann-Herder-Straße 3, 79014 Freiburg, Germany*

^b*Département de Physique Théorique, Université de Genève,
24 quai Ernest Ansermet, CH-1211 Genève 4, Switzerland*

Abstract

Motivated by the recent evidence for a stochastic gravitational-wave (GW) background reported by pulsar timing array (PTA) collaborations, we perform a precision study of low-scale phase transitions in a dark Abelian Higgs sector, a minimal gauge theory of spontaneous symmetry breaking relevant for cosmological phase transitions. Using dimensionally reduced high-temperature effective field theory, we quantify the impact of thermal resummation, higher-order matching corrections, and higher-dimensional operators on the phase-transition thermodynamics and the resulting GW signal. We find that the parameter region favored by current PTA observations lies close to the boundary of validity of the effective field theory, where higher-dimensional operators become increasingly important. Even within this controlled region, the predicted signal remains disfavored by the PTA data, despite the substantial shifts induced by higher-order thermal corrections. We further delineate parameter regions where the dark and visible sectors are thermally and hydrodynamically coupled or decoupled, and revisit the dark matter phenomenology, identifying asymmetric freeze-out as naturally compatible with both the observed relic abundance and the gauge couplings favored by strong phase transitions. Our results underscore the importance of systematically controlled finite-temperature calculations for reliable GW predictions from low-scale cosmological phase transitions.

*simone.biondini@physik.uni-freiburg.de

†philipp.schicho@unige.ch

Contents

| | | |
|----------|---|-----------|
| 1 | Introduction | 2 |
| 2 | Model setup | 4 |
| 2.1 | Portal interactions | 7 |
| 2.2 | Thermal equilibrium between dark and visible sectors | 9 |
| 3 | Gravitational waves from first-order phase transitions | 14 |
| 3.1 | Dimensionally reduced effective action | 14 |
| 3.2 | Phase transition thermodynamics | 20 |
| 3.3 | Gravitational wave spectrum | 26 |
| 4 | Dark matter freeze-out | 28 |
| 4.1 | Symmetric dark matter scenario | 30 |
| 4.2 | Asymmetric dark matter scenario | 34 |
| 5 | Reconciling first-order phase transitions with PTA data | 37 |
| 5.1 | Breakdown of high-temperature expansion | 40 |
| 5.2 | Implications for the PTA-favored region | 43 |
| 6 | Conclusions | 47 |
| A | Master integrals | 49 |
| A.1 | Zero-temperature master integrals | 49 |
| A.2 | Thermal master integrals | 51 |
| B | Zero-temperature vacuum structure | 53 |
| B.1 | Renormalization and one-loop β -functions | 53 |
| B.2 | Relations between $\overline{\text{MS}}$ -parameters and physical observables | 54 |
| C | Dimensional reduction details | 57 |
| D | Annihilation cross-sections across the phase transition | 60 |
| D.1 | Symmetric phase | 60 |
| D.2 | Broken phase | 61 |

1. Introduction

Despite the remarkable success of the Standard Model of particle physics (SM) in describing a vast range of phenomena with few fundamental particles and interactions, several observations remain unexplained. On the particle-physics front, the origin of neutrino masses still motivates extensive theoretical and experimental efforts [1–3]. On the cosmological side, the existence of dark matter (DM) [4–7], the dominant matter component of the Universe, and the observed baryon asymmetry [6, 8] both call for physics beyond the SM (BSM). Despite decades of dedicated searches, no conclusive evidence for a weakly interacting massive particle (WIMP) near the electroweak scale has emerged, and increasingly stringent constraints have excluded large parts of the simplest scenarios [7, 9]. While this does not rule out the WIMP paradigm, it has motivated a broader exploration of dark-sector frameworks with sub-electroweak-scale particles and alternative signatures.

Gravitational-wave (GW) astronomy has opened a new observational window on such hidden sectors, since a stochastic GW background (SGWB) may hold information about phase transitions and other dynamical processes in the early Universe. Gravitational-wave production associated with an electroweak-scale phase transition typically requires new particles with masses of $\mathcal{O}(100)$ GeV to $\mathcal{O}(1)$ TeV and sizable couplings to the Higgs sector. In such scenarios, the resulting SGWB is expected to peak in the mHz frequency range, making it a prime target for future space-based interferometers such as LISA [10, 11] or Taiji [12]. Gravitational-wave observations thus provide a powerful complement to collider searches for new physics [13–15].

A dark sector with its own gauge interactions and symmetry-breaking pattern may undergo a first-order phase transition that sources such a background. Recent measurements by several pulsar timing arrays (PTAs), such as NANOGrav [16, 17], EPTA [18–20], PPTA [21, 22], CPTA [23], and MPTA [24] have provided strong evidence for a SGWB in the nHz frequency range, reporting the quadrupolar Hellings-Downs correlations [25] expected to be of GW origin. While the signal may ultimately be explained by a population of merging supermassive black-hole binaries [26–28], reproducing its amplitude and spectral shape is non-trivial, not least because of the unresolved final-parsec problem [29]. Hence, the possibility that the signal originates from BSM physics remains an intriguing alternative.

Several cosmological mechanisms have been proposed to account for the SGWB reported by PTA collaborations, most notably cosmic strings, primordial black holes, and first-order phase transitions [20, 30, 31]. In this work, we focus on first-order phase transitions in a dark sector. For the resulting GW spectrum to peak in the nHz frequency range, the transition must occur well below the electroweak scale, typically at temperatures of $\mathcal{O}(1)$ – $\mathcal{O}(100)$ MeV.¹

¹A delayed electroweak phase transition could in principle also produce nHz gravitational waves, but such scenarios have been ruled out [32].

Such low-scale transitions point to new-physics states with masses well below the electroweak scale, giving rise to a rich phenomenology that connects GW observations with collider and fixed-target experiments as well as cosmological probes such as Big Bang Nucleosynthesis (BBN) and ΔN_{eff} .

The many particle-physics realizations of dark-sector phase transitions range from classically conformal models [33–42] to (multi-)scalar extensions [43–45]. Among them, the Abelian Higgs model is the simplest Higgs-gauge theory of spontaneous symmetry breaking and represents a broader class of models in which a radiatively generated, gauge-boson-induced cubic barrier renders the transition first order. This makes the model a long-standing benchmark exposed to finite-temperature methods, from thermal resummation to lattice simulations [46]. A dark Abelian Higgs sector therefore provides a minimal realization of a first-order phase transition capable of generating a PTA-scale SGWB if the dark scalar and gauge boson masses lie well below the electroweak scale, often in the MeV range.² Its proximity to BBN, however, introduces significant cosmological constraints. Relativistic dark-sector particles present during BBN contribute to N_{eff} , whereas unstable ones must decay early enough to preserve predictions of BBN [47–49].

A large body of recent work has explored the possibility that MeV-scale phase transitions could account for the PTA signal and is divided into two complementary directions:

- (i) model-independent descriptions via macroscopic quantities such as the transition temperature, latent heat, and inverse duration [49–53];
- (ii) specific particle-physics realizations that directly relate masses and couplings to the GW signal [50, 53–58].

Our work focuses on the second category. Whereas previous studies identified parameter regions compatible with PTA observations, whether genuinely or only through tuning, our primary objective is to provide a state-of-the-art thermodynamic analysis that tests the theoretical robustness of those predictions. To this end, we perform a precision thermodynamics analysis using high-temperature three-dimensional (3d) effective field theory (EFT) [59–64], which systematically incorporates thermal corrections and infrared (IR) effects in a gauge-invariant manner [65–67], allowing for controlled thermal resummation together with renormalization-group improvement [68]. We quantify theoretical uncertainties in the critical and percolation temperatures and compare with non-perturbative results [46]. We find that the PTA-favored region is particularly sensitive to higher-dimensional operators and lies close to the limit of validity of the high-temperature expansion and perturbativity.

²During radiation domination, the Hubble rate scales as $H \propto T^2/M_{\text{Pl}}$. Since the observed GW frequency today satisfies $f_0 = (a_*/a_0)f_*$ with $a_*/a_0 \propto T_0/T_*$, one finds the parametric scaling $f_0 \sim T_*T_0/M_{\text{Pl}}$, where T_0 is the present CMB temperature. A phase transition occurring at $T_* \sim 1$ MeV therefore naturally produces a signal in the nHz frequency range.

As emphasized in [49], a *decaying* dark sector is favored if a MeV-scale phase transition underlies the PTA signal, requiring portal interactions that allow the dark scalar and gauge boson to decay before BBN and thereby avoiding stringent constraints on the effective number of relativistic species, ΔN_{eff} . Motivated by this, we extend the minimal Abelian Higgs model with a fermionic dark matter candidate charged under the dark gauge group [54, 56], rendering it stable. This setup allows us to study both the GW phenomenology of the phase transition and the dark matter implications of the model. In particular, we analyze symmetric and asymmetric freeze-out scenarios, including Sommerfeld enhancement and bound-state formation, and assess the complementarity between couplings favored by the observed dark matter abundance and those required for a strong first-order phase transition.

In addition, we revisit the thermalization between the dark and visible sectors. Because cosmological constraints require small portal couplings, thermal equilibrium is not guaranteed *a priori*. We therefore compute the relevant interaction rates and identify the dominant processes that maintain thermal contact between the two sectors during the epoch relevant for the phase transition. Beyond thermal equilibrium, we examine hydrodynamic equilibrium between the two sectors during the phase transition. We identify parameter regions where the SM plasma decouples from the bubble dynamics. In this regime, the hydrodynamic evolution on scales of the bubble size and below is governed only by the dark sector, while the total radiation density still determines the expansion history and GW amplitude.

The structure of the paper is as follows. Section 2 introduces the dark-sector model and discusses its phenomenology, including the thermalization conditions between the dark and visible sectors. The thermodynamic framework for the phase transition is outlined in sec. 3, where we derive the thermal EFT. The dark matter phenomenology is discussed in sec. 4, while sec. 5 addresses the GW spectra and their reconciliation with PTAs. Finally, we present our conclusions in sec. 6, while additional technical details are collected in the appendices.

2. Model setup

The primary goal of this work is to investigate the thermodynamics of a phase transition at *low energy scales*, specifically in the range $\mathcal{O}(1\text{--}100)$ MeV, and to determine the associated SGWB signal. To this end, we consider an Abelian dark Higgs model, consisting of a complex scalar field (S), a dark gauge boson (V_μ), and a $U(1)_d$ gauge symmetry. This constitutes a minimal field content, an archetypal framework, that may trigger a first-order phase transition [46, 66, 67, 69–73] in a dark sector [49, 74]. We introduce portal interactions with the SM through renormalizable operators. The Higgs portal [75–77] for the dark scalar and kinetic mixing [78, 79] for the dark gauge boson V_μ . These couplings allow for efficient decays into the SM, ensuring that both dark particles decay away before BBN.

To remain compatible with Big Bang Nucleosynthesis (BBN), these decays must occur at

lifetimes below $\tau_{\text{BBN}} \approx 0.1$ s to avoid disrupting light element abundances [80]. Furthermore, late-time energy injection from light particles can affect the Cosmic Microwave Background (CMB) through changes in the effective number of relativistic degrees of freedom N_{eff} [81], spectral distortions from black-body radiation [82,83], and the ionization history [84]. Details regarding the portal interactions and constraints on the corresponding couplings are presented in sec. 2.1.

Since we also aim to inspect the interplay between the dark phase transition and a stable relic DM particle, which may account for the observed DM energy density $\Omega_{\text{DM}} h^2 = 0.1200 \pm 0.0012$ [85], we consider a next-to-minimal dark sector that comprises a dark fermion (X). The dark fermion is taken to be a SM gauge singlet, whereas it is charged under $U(1)_d$. As a result, we end up in a class of DM models that have been extensively studied [76, 86–91]. Here, the DM relic abundance is mainly determined by interactions internal to the dark sector with little or no involvement of the SM degrees of freedom.³ For a thermalized dark sector and a dark fermion heavier than the bosonic degrees of freedom, the DM relic density is fixed via fermion-antifermion annihilations that drive a freeze-out dynamics.

We take the dark fermion to be of Dirac type, with its bare mass parameter μ_X a free input of the model, fixed at the input scale to the physical fermion mass, $\mu_X(\bar{\mu}_0) = m_X$ (cf. sec. B.2). This is the most convenient choice for our purpose of addressing the phase transition within a viable dark matter model, and it allows a direct comparison with [54, 56], where the same model was invoked to explain the PTA data. Alternative realizations comprise e.g. a Majorana dark fermion [89, 90] or chiral fermions with different charge assignments [46, 56, 93], whose mass is generated only after the spontaneous breaking of the $U(1)_d$ symmetry.⁴

The phase transition of the model has been studied on the lattice, both without fermions and with Yukawa-coupled fermions, and the corresponding phase diagram was obtained in [46]. It features a tricritical endpoint that separates first-order (type I superconductor) from second-order (type II superconductor) transitions, located non-perturbatively in [94] and perturbatively in [95, 96]. In the case with Yukawa-coupled fermions, the fermions are not simulated directly but integrated out in the dimensional reduction, so that their effect enters only through the matching relations (cf. sec. C).

The four-dimensional (4d) model Lagrangian (cf. e.g. [91, 97]) in Minkowski space-time is

$$\mathcal{L} = \bar{X}(i\mathcal{D} - \mu_X)X - \frac{1}{4}V_{\mu\nu}V^{\mu\nu} + (D^\mu S)^*(D_\mu S) - V(S^*S) + \mathcal{L}_{\text{portal}},$$

$$V(S^*S) = -\mu_s^2 S^*S + \lambda_s(S^*S)^2, \quad (2.1)$$

³There are various possibilities for naming such a model class, such as *two-mediator* models [89–91] or hidden/secluded sectors [76, 86]. The model realization that we consider in this paper features a Dirac fermion dark matter, similarly to [92].

⁴The latter case introduces no additional parameters, since a Yukawa coupling replaces the bare mass, but the fermion then enters the phase-transition thermodynamics directly, which makes the freeze-out and phase-transition dynamics harder to disentangle; we leave this option for future work.

where $D_\mu = \partial_\mu - ig_d Y_i V_\mu$ is the covariant derivative, g_d is the dark gauge coupling, Y_i the corresponding hypercharge of the fermion and scalar field, and V_μ the gauge field of the dark sector with the field strength tensor $V_{\mu\nu}$. Since the DM is a Dirac fermion, a trilinear coupling of the form $\bar{X}XS$ is absent, unless either the fermion or the scalar is a $U(1)_d$ singlet (namely $Y_s = 0$ or $Y_X = 0$). We assign equal $U(1)_d$ charges to the fermion and the scalar, taking $Y_X = Y_s = 1$.⁵ The portal interactions, which induce a mixing of the dark and SM states, are addressed in sec. 2.1.

The scalar potential contains the parameters $\mu_s^2 > 0$ and $\lambda_s > 0$. We parametrize the complex scalar field by its vacuum expectation value (VEV), v_s , and two real degrees of freedom, s and χ . Here, χ is the Goldstone boson associated with the symmetry breaking,

$$S = \frac{1}{\sqrt{2}}(v_s + s + i\chi), \quad v_s = \sqrt{\frac{\mu_s^2}{\lambda_s}}, \quad (2.2)$$

when promoting v_s to a background field, we later use $v_s = \phi$ in sec. 3. After spontaneous symmetry breaking of the dark gauge group, we find the following Lagrangian

$$\begin{aligned} \mathcal{L} = & \mathcal{L}_V + \mathcal{L}_s + \mathcal{L}_\chi + \mathcal{L}_X \\ & + \frac{g_d^2}{2} V_\mu V^\mu s^2 + \frac{g_d^2}{2} V_\mu V^\mu \chi^2 + g_d m_V V_\mu V^\mu s + g_d V^\mu (\chi \partial_\mu s - s \partial_\mu \chi) \\ & - \frac{\lambda_s}{4} s^4 - \frac{\lambda_s}{4} \chi^4 - \frac{\lambda_s}{2} s^2 \chi^2 - m_s \sqrt{\frac{\lambda_s}{2}} s \chi^2 - m_s \sqrt{\frac{\lambda_s}{2}} s^3 + g_d \bar{X} \Psi X + \mathcal{L}_{\text{portal}}. \end{aligned} \quad (2.3)$$

The first line contains the free Lagrangian terms for each field. The second line encodes the interactions between the scalar fields s and χ and the gauge boson; the third line includes scalar self-interactions, and the fermion–gauge boson interaction, analogous to QED, as well as the portal Lagrangian. The resulting particle masses, including those of the Goldstone boson and the ghost field c , are⁶

$$m_s^2 = 2v_s^2 \lambda_s, \quad m_V^2 = (g_d v_s)^2, \quad m_\chi^2 = m_c^2 = \xi m_V^2. \quad (2.4)$$

Following the generalized gauge fixing choices of [98], all computations are performed in a general R_ξ (or Fermi) gauge. The corresponding gauge fixing functional that enters the gauge fixing Lagrangian $\mathcal{L}_{\text{GF}} = \frac{1}{2\xi} [F(v_s)]^2$ is $F(v_s) = \partial_\mu V^\mu + \xi g_d v_s \chi$. Since gauge invariance is manifest in all our computations, we display results in Landau gauge ($\xi \rightarrow 0$) throughout the paper when dealing with the thermodynamics of the phase transitions. For the dark matter annihilation cross-sections, on the other hand, we work in Feynman gauge ($\xi \rightarrow 1$).

⁵In the appendix, we keep a generic hypercharge in the matching equations for the 3d theory.

⁶The ghost Lagrangian, including its interaction with the scalar s , reads $\mathcal{L}_c = \bar{c}[-\partial^2 - \xi m_V^2(1 + \frac{s}{v_s})]c$.

2.1. Portal interactions

Portal interactions can be naturally incorporated via renormalizable operators such as the Higgs portal [75–77] and kinetic mixing [78, 79]. The corresponding portal Lagrangian is [90, 91]

$$\mathcal{L}_{\text{portal}} = -\frac{\epsilon_V}{2c_w} V^{\mu\nu} B_{\mu\nu} - \epsilon_s S^* S H^\dagger H, \quad (2.5)$$

where ϵ_V and ϵ_s parametrize the couplings of the visible-to-dark sector interactions; θ_w is the Weinberg angle with $\cos \theta_w \equiv c_w$ and $\sin \theta_w \equiv s_w$; $B_{\mu\nu}$ is the field strength tensor of the SM $U(1)_Y$ gauge group; and H is the SM Higgs doublet. The SM gauge coupling of $SU(2)$ is denoted by g_2 and for $U(1)_Y$ by g_1 . The portal couplings, assumed to be $\epsilon_V, \epsilon_s \lesssim 1$, are constrained by numerous experimental bounds, which we summarize in the following.

The presence of portal interactions induces mixing between the dark and SM states. After the spontaneous symmetry breaking of both sectors, the dark Higgs mixes with the SM Higgs boson, and the dark photon mixes with both the SM photon and the Z boson (see e.g. [91]). This induces tree-level couplings of the dark scalar to SM fermions and gauge bosons, and of the dark photon to SM fermions. Consequently, decay channels $s \rightarrow \text{SM SM}$ and $V \rightarrow \text{SM SM}$ are generically allowed whenever kinematically accessible. These portal interactions not only enable experimental searches for dark states, but also govern the thermal contact between the visible and dark sectors in the early universe; see sec. 2.2.

We focus on dark-sector mass scales below $\mathcal{O}(100)$ MeV, where both the dark scalar and dark photon are much lighter than their SM counterparts: $m_s \ll m_h$ and $m_V \ll m_Z$. In this limit of small mixing and hierarchical masses, the portal couplings relate directly to the physical mixing angles. To leading order (LO), one finds (see, e.g., [91])

$$\sin \theta_s \simeq \epsilon_s \frac{v_h v_s}{m_h^2}, \quad \sin \theta_V \simeq \epsilon_V \tan \theta_w. \quad (2.6)$$

2.1.1. Dark scalar portal

The model is subject to a variety of laboratory, astrophysical, and cosmological constraints. Even independently of the dark fermion X , stringent bounds apply to both the dark Higgs s and the dark photon V_μ . The portal interaction $\epsilon_s S^* S H^\dagger H$ induces a mixing between the dark scalar and the SM Higgs, allowing for direct searches in rare meson decays and fixed-target experiments. In the range of phase-transition energy scales relevant for this work, $\mathcal{O}(1)$ – $\mathcal{O}(100)$ MeV, accelerator constraints are complemented by bounds from stellar cooling as well as from BBN and the CMB [99–103].

For the dark scalar, the most stringent laboratory constraints in the sub-GeV mass range arise from rare kaon decays. In particular, NA62 and E949 constrain the branching ratio of $K^+ \rightarrow \pi^+ s$, implying an approximate upper bound $\sin \theta_s \lesssim 2 \times 10^{-4}$ for $m_s \lesssim 100$ MeV [104,

105]. In addition, light scalars with masses below ~ 150 MeV are constrained by observations of core-collapse supernovae, excluding the mixing-angle window $3.9 \times 10^{-7} \lesssim \sin \theta_s \lesssim 7.0 \times 10^{-6}$ [106]. Cosmological bounds from BBN and the CMB depend sensitively on the scalar lifetime and its visible branching fractions. Unstable light particles can also significantly affect the thermal history of the universe. Their impact on BBN and the CMB depends sensitively on their lifetime. Dark scalars with lifetimes $\tau \lesssim 0.1$ s decay sufficiently early to evade cosmological bounds. Conversely, longer lifetimes, as favored by current laboratory constraints, can inject energetic particles into the primordial plasma, thereby modifying light-element abundances through electromagnetic or hadronic processes, and distorting the CMB anisotropy spectrum. A comprehensive analysis of these effects for Higgs-mixed scalars can be found in [99–101, 103]. Adopting the most recent analysis of [103], we therefore focus on the representative parameter region⁷

$$m_s \in [3.8, 100] \text{ MeV}, \quad \sin \theta_s \in [2 \times 10^{-5}, 2 \times 10^{-4}]. \quad (2.7)$$

These bounds on m_s and $\sin \theta_s$ can be reinterpreted as constraints on the dark scalar self-coupling λ_s . Using the relation

$$\lambda_s = \left(\frac{\epsilon_s}{\sin \theta_s} \right)^2 \frac{1}{4\lambda_h} \left(\frac{m_s}{m_h} \right)^2, \quad (2.8)$$

and the measured SM Higgs parameters, we infer the allowed range of λ_s for representative choices of the portal coupling ϵ_s . Since experimental constraints are most directly expressed through the physical mass m_s and mixing angle $\sin \theta_s$, we trade the portal coupling ϵ_s for the parameter set $(m_s, \lambda_s, \sin \theta_s)$. For each scan point, the value of ϵ_s is fixed by eq. (2.8), which follows from the scalar mass matrix in the small-mixing limit.

We close this section with an important phenomenological implication for the parameter scan in sec. 5. The relation in eq. (2.8) imposes a constraint on the dimensionful ratio λ_s/m_s^2 . Using the Higgs boson mass, $m_h = 125.1$ GeV, its derived self-coupling, $\lambda_h \simeq 0.13$ [107], and the allowed range of the mixing angle in eq. (2.7) for the dark scalar masses considered here, we obtain

$$\frac{\epsilon_s^2}{(\sin \theta_s^{\max})^2} \leq \frac{\lambda_s}{1.2 \times 10^{-10}} \left(\frac{\text{MeV}}{m_s} \right)^2 \leq \frac{\epsilon_s^2}{(\sin \theta_s^{\min})^2}, \quad (2.9)$$

where the minimal and maximal mixing angles are given by eq. (2.7). This relation guides the phenomenologically viable parameter space of the model and may impose additional restrictions on the parameter scan presented in tab. 2 through the requirement $\epsilon_s < 1$.

⁷The same range is adopted in [53]. The analyses of [99, 103] consider one mediator at a time and do not explicitly incorporate an underlying $U(1)_d$ gauge structure. In the model (2.1), additional decay channels such as $s \rightarrow VV$ could in principle open up at $g_d \sim \mathcal{O}(1)$ and modify the scalar lifetime and branching fractions. The barrier-induced phase transitions in sec. 3, however, require $m_V \gg m_s$ (cf. sec. 3), which also holds at $T = 0$, so that $s \rightarrow VV$ remains kinematically closed.

2.1.2. Dark photon portal

Constraints on massive dark photons are typically parametrized by the kinetic mixing parameter ϵ_V , which controls the coupling of V_μ to the electromagnetic current after electroweak symmetry breaking. Comprehensive bounds are summarized in [108]. For the dark photon mass range relevant to this work, $m_V \sim \mathcal{O}(1\text{--}100)$ MeV, the most stringent constraints arise from astrophysical and cosmological probes sensitive to production and decay of weakly-coupled light vectors in supernova cores and the early universe.

In particular, SN1987A cooling arguments constrain the emission of dark photons from the supernova core and typically exclude intermediate values of the kinetic mixing [109]. Additional limits follow from the non-observation of γ -rays associated with late decays of supernova-produced dark photons [110], as well as from envelope and trapping effects in core-collapse supernovae [111]. At the same time, BBN bounds derived from photo-dissociation and neutron-proton conversion processes exclude scenarios in which long-lived dark photons inject electromagnetic energy during or after nucleosynthesis [99, 100]. Together, these considerations imply that for $m_V \sim \mathcal{O}(1\text{--}100)$ MeV, the viable parameter space typically lies at very small kinetic mixing, often $\epsilon_V \lesssim 10^{-9}\text{--}10^{-10}$, with details depending on the precise mass range and decay channels.

If the dark photon also couples to the dark fermion X , additional constraints arise from direct-detection searches mediated by V_μ . For representative dark matter masses $10 \text{ GeV} \lesssim m_X \lesssim 100 \text{ GeV}$, the PandaX-II experiment excludes a broad region of parameter space, roughly $10^{-11} \lesssim \epsilon_V \lesssim 5 \times 10^{-9}$ [112]. Complementary constraints on ϵ_V in this mass range arise from fixed-target and beam-dump experiments, although for the small mixing angles relevant here, astrophysical and cosmological limits dominate [108].

In summary, thermal contact between the Standard Model and the dark sector is primarily established through the scalar portal, namely the Higgs-dark scalar mixing angle $\sin \theta_s$, while the kinetic mixing of the dark photon is negligible in the parameter region considered in this work. Thermal equilibrium within the dark sector, on the other hand, is efficiently maintained by the dark gauge interactions for the values of the gauge coupling $g_d \sim \mathcal{O}(1)$ considered throughout this study.

In the following section, we present our strategy for determining whether the two sectors remain in thermal equilibrium and for estimating the temperature at which they eventually decouple.

2.2. Thermal equilibrium between dark and visible sectors

In this section, we investigate whether the dark and visible sectors remain in thermal equilibrium throughout the epoch relevant for the dark-sector phase transition. Throughout this analysis, we assume that the hidden-sector particles, the dark matter fermion X and the

dark bosons S, V_μ , efficiently thermalize among themselves, such that the dark sector can be characterized by a single temperature T_{DS} . This assumption is well justified for the values of the gauge coupling g_d considered in this work, which lie in the range $0.1 \lesssim g_d \lesssim 1$.

In this work, we assume that thermal contact between the dark and visible sectors is established exclusively through the scalar portal. We therefore neglect processes involving the dark gauge boson and SM particles induced by kinetic mixing in eq. (2.5). This approximation is well motivated in the parameter region of interest, where current constraints require the kinetic mixing parameter to be significantly smaller than the scalar mixing angle for the dark scalar and vector boson masses considered in our analysis.

Whenever the two sectors are in thermal equilibrium, the same temperature also describes the SM plasma, which we denote by T . Determining whether, and down to which temperature, the two sectors remain thermally coupled is particularly relevant for the computation of the GW signal discussed in sec. 3. In particular, whether the dark and visible sectors share a common temperature determines which relativistic degrees of freedom enter the redshift factors of the GW signal, and hence its peak frequency and amplitude, as well as justifying the use of a single temperature throughout the computation.

Thermal equilibrium is assessed by comparing the interaction rate with the Hubble expansion rate, requiring the condition

$$C_T^{\text{eq}} : \quad \Gamma_{\text{int}}(T) > H(T). \quad (2.10)$$

Here, Γ_{int} denotes the total interaction rate, including all relevant $1 \rightarrow 2$ and $2 \rightarrow 2$ processes involving dark-sector and SM particles, both number-changing and number-conserving. The value of the Hubble rate during the radiation-dominated era at fixed temperature is

$$H^2(T) = \frac{8\pi}{3} \frac{\rho_r(T)}{m_{\text{Pl}}^2}, \quad \rho_r(T) = \frac{\pi^2}{30} g_{\text{eff,tot}}(T) T^4, \quad m_{\text{Pl}} = 1.22 \times 10^{19} \text{ GeV}, \quad (2.11)$$

where $g_{\text{eff,tot}} = g_{\text{eff,SM}} + g_{\text{eff,DS}}$ is the total effective number of relativistic degrees of freedom of the SM and the dark sector (DS). For the SM contribution, we use the results of [113], supplemented by the relativistic bosonic degrees of freedom of the dark sector.⁸

For dark-sector phase transitions occurring well below the electroweak crossover temperature, $T_{\text{c,SM}} \simeq 160 \text{ GeV}$ [114], we can restrict our analysis to the regime where electroweak symmetry is already broken and all SM particles, except neutrinos, are massive. We therefore focus on the temperature interval $1 \text{ MeV} \lesssim T \lesssim 1 \text{ GeV}$. To obtain two separate phase transitions, $(0, 0) \rightarrow (v_h, 0) \rightarrow (v_h, v_s)$, we require the intermediate electroweak-broken phase

⁸Throughout this work we take $m_X \gtrsim 1 \text{ GeV}$, so that the dark fermion is non-relativistic across the entire temperature range of interest. Rather than explicitly computing thermodynamic quantities for the dark-sector states, we adopt a phenomenological prescription for their contribution to the energy density entering the Hubble rate. More precisely, the scalar and vector boson contributions are suppressed by Boltzmann factors $e^{-m_s/T}$ and $e^{-m_V/T}$, respectively.

to be stable against fluctuations in the singlet direction. This is controlled by the curvature of the finite-temperature effective potential near the electroweak transition,

$$\left. \frac{\partial^2 V}{\partial S \partial S^*} \right|_{S=0} = -\mu_s^2 + \frac{\epsilon_s}{2} v_h^2(T) + \left(\frac{\lambda_s}{3} + \frac{g_d^2}{4} \right) T^2, \quad (2.12)$$

where the LO thermal mass correction of the dark scalar is given in eq. (C.4). Following the standard treatment of Higgs-portal models, the zero-temperature contribution $\epsilon_s v_h^2/2$ induced after electroweak symmetry breaking is absorbed into a redefinition of the quadratic parameter μ_s^2 . The above stability condition is therefore imposed only for temperatures near the electroweak transition, where $v_h(T)$ differs from its zero-temperature value. Since $\epsilon_s > 0$, the Higgs condensate contributes positively to the curvature in the singlet direction, thereby favouring the stability of the intermediate electroweak-broken phase. We have explicitly verified that this condition is satisfied throughout the parameter space in tab. 2.

The relevant interaction channels depend on the phase of the dark sector. A key feature of the model is that mixing between the dark scalar and the SM Higgs boson arises only after spontaneous symmetry breaking in the dark sector, i.e. when $v_s \neq 0$. The cross term $\sim \epsilon_s v_h v_s$ then induces the physical mixing angle $\sin \theta_s$, opening decay and scattering channels into SM states that can substantially enhance thermal contact between the two sectors, allowing thermal equilibrium to be maintained even for relatively small values of $\sin \theta_s$.

For temperatures above the critical temperature of the dark sector, $T > T_{c,DS}$, the only relevant $1 \rightarrow 2$ process is the Higgs decay $h \rightarrow SS^*$ and the corresponding inverse decay. The associated $2 \rightarrow 2$ number-changing processes are

$$hh \rightarrow SS^*, \quad ZZ \rightarrow SS^*, \quad W^+W^- \rightarrow SS^*, \quad f\bar{f} \rightarrow SS^*, \quad (2.13)$$

where f denotes SM fermions. For brevity, only processes with dark scalars in the final state are shown. The corresponding reverse reactions are implicitly included. Additionally, there are number-conserving scattering processes and their conjugates,

$$Sh \rightarrow Sh, \quad ZS \rightarrow ZS, \quad W^-S \rightarrow W^-S, \quad fS \rightarrow fS. \quad (2.14)$$

The first class of $2 \rightarrow 2$ processes coincides with those encountered in Higgs-portal scalar dark matter models; see e.g. [115] for the corresponding cross-sections.

After spontaneous symmetry breaking in the dark sector, the physical dark scalar s acquires couplings to SM fermions through Higgs mixing. Consequently, in addition to the processes listed above (with the replacement $S \rightarrow s$), several new decay and scattering channels become relevant whenever kinematically allowed. Examples include the decays $s \rightarrow f\bar{f}$ and scattering processes such as $s\gamma \rightarrow f\bar{f}$ and $sf \rightarrow \gamma f$, where γ denotes the SM photon. Similar processes involving QCD gluons may also occur, whereas those involving the electroweak massive gauge bosons are strongly suppressed in the temperature range considered here. Related processes

have been investigated previously in [91, 103, 116]. In the present work, we independently compute all relevant rates and include them in the evaluation of the total interaction rate $\Gamma_{\text{int}}(T)$.

Compared to earlier studies [91, 103], we additionally include the class of processes induced by scalar self-interactions in eq. (2.3). Throughout, we work at LO in the small mixing angle $\sin \theta_s$ and keep only diagrams containing a single insertion of a mixing-induced vertex. For the thermal collision integrals associated with the $2 \rightarrow 2$ processes, we neglect Fermi-Dirac and Bose-Einstein statistical factors, following the standard approximation commonly adopted in phenomenological studies, including [91]. This approximation typically induces uncertainties at the $\mathcal{O}(10\%)$ level [117].⁹

In the temperature range of interest, $T < 1$ GeV, heavy SM particles are strongly Boltzmann suppressed. Hence, thermal equilibrium is maintained predominantly through interactions with the light SM degrees of freedom, namely leptons and light quarks. Below the QCD crossover temperature, $T \lesssim 155$ MeV [121], a hadronic description replaces the partonic one. Following [103], we implement the effective interactions between the dark scalar and pions and kaons, and find that their contribution to the interaction rate is subleading. In practice, processes involving quarks and hadrons play only a minor role throughout most of the temperature range considered here, either due to Boltzmann suppression of the heavier quarks or to the comparatively small hadronic interaction rates below the QCD crossover.

A similar hierarchy applies to leptons. The mixing-induced couplings to SM fermions scale as $\propto \sin \theta_s m_f/v_h$, suppressing processes involving very light fermions. At the same time, the tau lepton, with mass $m_\tau \simeq 1.7$ GeV, becomes rapidly Boltzmann suppressed below $T \lesssim 100$ MeV. Consequently, among the leptonic channels, muon-induced processes typically dominate the interaction rate.

We now discuss the results of the thermalization analysis. Figure 1 (left) shows the interaction rates in the broken phase of the dark sector, where three classes of $2 \rightarrow 2$ processes involving SM leptons contribute. Focusing on the muon channel, we find that processes induced by dark-scalar self-interactions dominate the interaction rate below the dark-sector phase transition. The vertical gray lines indicate the critical temperature for two benchmark choices of g_d , with $\lambda_s = 0.01$ and $m_s = 10$ MeV held fixed (for $g_d = 0.5$ and $g_d = 0.8$, corresponding to the leftmost and rightmost vertical lines, respectively). Higgs-mediated processes in the s - or t -channel are strongly suppressed by the Higgs mass. By contrast, the self-interaction-mediated channels are competitive with, and often dominate over, the QED-assisted processes $s\mu \rightarrow \mu\gamma$ and $s\gamma \rightarrow \mu\bar{\mu}$. This picture also holds when lowering λ_s and m_s

⁹Since improvements act in several directions simultaneously, and go beyond correcting statistical factors alone, we leave such an analysis for future work. A more refined computation would also require an accurate evaluation of dark scalar decays into SM leptons, accounting for multiple soft scatterings and thermal masses [118–120].

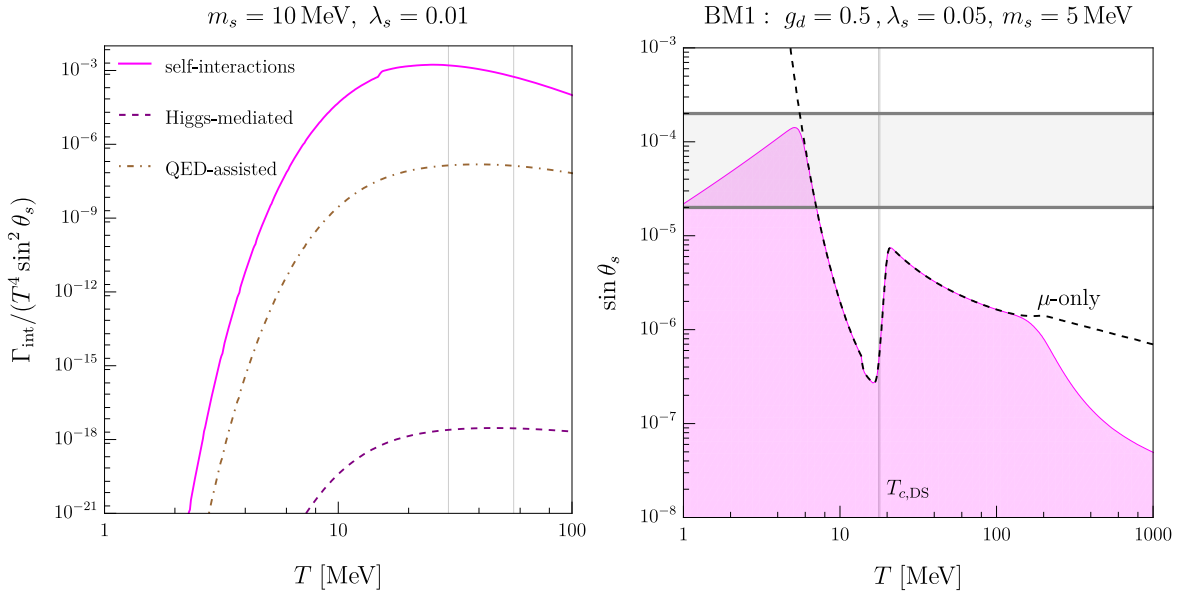


Figure 1: Left: Thermal interaction rate normalized by $T^4 \sin^2 \theta_s$ for processes involving muons. Three classes of $2 \rightarrow 2$ scatterings are shown: dark-scalar self-interaction mediated (solid magenta), Higgs mediated (dashed purple), and QED-assisted processes (dot-dashed brown). Right: Equilibration condition in the $(T, \sin \theta_s)$ plane for fixed values of the dark-sector couplings and masses. The magenta shaded region corresponds to $\Gamma_{\text{int}} < H$, where the two sectors lose thermal contact. The contribution obtained by including only muon-induced processes is also shown (black dashed), while the critical temperature $T_{c,DS}$, is indicated by the vertical gray line.

to the lower values relevant to our work. The enhancement induced by scalar self-interactions is also responsible for the sharp decrease of the mixing angle required to maintain thermal equilibrium below the critical temperature $T_{c,DS}$, as seen in fig. 1 (right).

Figure 1 (right) shows the thermalization condition $\Gamma_{\text{int}} \geq H$ (white region) for the benchmark point BM1 discussed in sec. 5. The magenta shaded region marks where thermal equilibrium between the two sectors is lost. We also superimpose a gray band indicating the phenomenologically viable range of $\sin \theta_s$ (2.7).

To illustrate the dominant role of muon-induced processes in most of the temperature range, we additionally display the contour obtained by including only processes involving muons (black dashed). This approximation underestimates the total interaction rate for temperatures $T \gtrsim 100$ MeV, where tau leptons and charm quarks still provide sizable contributions due to their relatively mild Boltzmann suppression. On the other hand, in the low-temperature regime, $T \lesssim 5$ MeV, muon-induced processes become exponentially suppressed and the dominant contribution instead arises from scalar decays into electrons, $s \rightarrow e\bar{e}$, which

constitute the only kinematically accessible decay channel. Decays into neutrinos instead remain negligible due to the tiny neutrino masses.

For the parameter scan in tab. 2 and the analysis of the stochastic GW background in sec. 5, we explicitly verified the thermalization condition using the interaction rates described in this section. We find that the two sectors do not always share the same temperature throughout the parameter space explored in this work. See the discussion in sec. 5.

3. Gravitational waves from first-order phase transitions

The model of eq. (2.1) can undergo a first-order phase transition in the early universe [46, 66, 67, 69–71, 73]. We focus on a dark-sector transition occurring well below the SM electroweak crossover, $T_{\text{c,DS}} \ll T_{\text{c,SM}}$. In this section, we outline the framework used to determine the corresponding thermodynamic and GW observables, starting from the thermal effective action in sec. 3.1, the phase-transition thermodynamic parameters in sec. 3.2, and the resulting GW spectrum in sec. 3.3.

3.1. Dimensionally reduced effective action

At high temperatures, equilibrium thermodynamics is most efficiently described via the effective action of a three-dimensional effective field theory (3dEFT) obtained via high-temperature dimensional reduction [59, 60, 62, 63, 122–124]. The latter is formulated in the imaginary-time formalism and in Euclidean space-time. Since the heat bath singles out a rest frame $u_\mu = (1, \mathbf{0})$, Lorentz invariance is no longer explicitly manifest [125] and additional interactions involving the temporal component of the gauge field, the temporal vector V_0 , can arise. For the model of eq. (2.1), the field V_0 acquires a Debye mass $m_{\text{D}} \sim \mathcal{O}(g_d T)$.

The corresponding 3dEFT Lagrangian is purely bosonic [46, 126–128] and up to mass dimension four, its super-renormalizable part is

$$\mathcal{L}^{3d} = \frac{1}{4} V_{ij}^2 + (D_i S)^* (D_i S) + \mu_{s,3}^2 S^* S + \lambda_{s,3} (S^* S)^2 + \mathcal{L}_\tau, \quad (3.1)$$

$$\mathcal{L}_\tau = \frac{1}{2} (\partial_i V_0)^2 + \frac{1}{2} m_{\text{D}}^2 V_0^2 + h_3 V_0^2 S^* S + \frac{\kappa_3}{4} V_0^4, \quad (3.2)$$

where \mathcal{L}_τ encodes the contributions of the temporal vector. The spatial covariant derivative with indices $i = \{1, \dots, d\}$ reads $D_i = \partial_i - i g_{d,3} V_i$, with $g_{d,3}$ the three-dimensional effective gauge coupling. In the broken phase, the gauge fixing functional takes the same form as in the fundamental 4d theory of sec. 2.

The matching of the super-renormalizable 3dEFT parameters to the fundamental 4d theory is performed automatically using DRalgo [129, 130]. Since fermions are non-dynamical at high temperatures, their effects enter only implicitly as ultraviolet (UV) corrections to the

effective parameters. The matching relations up to next-to-next-to-leading order (NNLO) in the coupling expansion and dimension four in mass dimension are listed in appendix C as well as in [67] and employed in our numerical scans of sec. 5. Compared to [67], we extend the matching by including fermionic mass effects at one-loop order.¹⁰

For the strongest transitions, higher-dimensional operators become relevant [73, 131] and it is in practice insufficient to consider only the super-renormalizable operators of eqs. (3.1) and (3.2). The full set of dimension-six operators in the dimensionally reduced Abelian Higgs model is derived in [73] and was recently generalized for generic models in DRalgo [130]. See also [132–134] for alternative automatic construction of static thermal EFTs. Including higher-dimensional operators in the thermal EFT can only extend the validity of the high-temperature expansion over a limited region of parameter space [73]. If the EFT breaks down at a given point due to the omission of dimension-six operators, then including those operators merely postpones the breakdown to the point where dimension-eight operators become important, and so on. Hence, we only indirectly include dimension-six operators in the construction of the EFT by inspecting the criteria (EFT1) and (EFT2) of [73] which determine if individual parameter points remain valid under the assumption of high-temperature expansion; cf. sec. 5.1.

The construction of the EFT proceeds in two steps. First, the hard modes $\sim \pi T$ are integrated out at vanishing scalar background $\phi = 0$, yielding the *soft-scale* EFT for the symmetric phase [73, 135]:

Symmetric phase (sym)

The temporal vector V_0 with Debye mass m_D are heavy, the two scalar degrees of freedom S are light, and vector bosons V_i are massless. The hierarchy is

$$m_{V,3}^2 \ll m_{s,3}^2 \ll m_D^2 \ll \pi T. \quad (3.3)$$

Second, allowing for a non-vanishing background in the soft 3dEFT, ϕ_3 , and using the scalar-field parametrization (2.2) in three-dimensions and Landau gauge ($\xi = 0$), also the spatial gauge bosons acquire a mass [67]

$$\begin{aligned} m_{s,3}^2 &= \mu_{s,3}^2 + 3\lambda_{s,3}\phi_3^2, & m_{\chi,3}^2 &= \mu_{s,3}^2 + \lambda_{s,3}\phi_3^2, \\ m_{V,3}^2 &= g_{d,3}^2\phi_3^2, & m_{V_0}^2 &= m_D^2 + h_3\phi_3^2. \end{aligned} \quad (3.4)$$

At the phase transition, vector and scalar masses are hierarchically separated such that $x \simeq m_{s,3}^2/m_{V,3}^2$ is the effective expansion parameter [66, 136, 137]; see eq. (3.8) for a precise

¹⁰ Since the dark fermion mass $m_X \sim \mathcal{O}(10\text{--}10^2)$ GeV is much larger than the MeV dark-sector phase transition scale, fermionic contributions remain Boltzmann suppressed for the entire parameter space range relevant to our analysis. Our matching relations (C.2)–(C.7) exhibit full fermion-mass dependence and are useful when the dark fermion is dynamical during the phase transition.

definition. The resulting broken-phase theory is a 3d Higgs EFT (HEFT) theory [46] also obtainable in DRalgo [129, 130]. The relevant scale hierarchies are:

Broken phase (bro) soft EFT

Spatial V_i and temporal vectors V_0 acquire a field-dependent mass of $\mathcal{O}(g_{d,3}\phi_3)$ and can be integrated out on the same footing. The hierarchy and validity range [73] is¹¹

$$m_{s,3}^2 \ll m_{V,3}^2 \sim m_{V_0}^2 \ll \pi T, \quad 0.051g_d^2 \ll x \ll 0.18. \quad (\text{EFT1})$$

In practice, another hierarchy can emerge in a setup known as the softer EFT setup (EFT2), where the temporal vector is heavier than the spatial gauge bosons:

Broken phase (bro) softer EFT

Spatial V_i and temporal vectors V_0 acquire a field dependent mass of $\mathcal{O}(g_{d,3}\phi_3)$ and can be integrated out successively. The hierarchy and validity range [73] is

$$m_{s,3}^2 \ll m_{V,3}^2 \ll m_{V_0}^2 \ll \pi T, \quad 0.18g_d \ll x \ll 0.18. \quad (\text{EFT2})$$

In this setup, higher-dimensional operators become significantly relevant in the strong transition regime, which reduces its region of validity. We will investigate how such a breakdown manifests in thermodynamic quantities in sec. 5.1.

The Abelian Higgs model at finite temperature, falls into a broader class of models with a generic radiatively induced cubic barrier. The LO broken-phase potential of EFT1 takes the form

$$V_{\text{eff}}^{\text{bro}}(\phi_3) = \frac{1}{2}\mu_{s,3}^2\phi_3^2 + \frac{1}{4}\lambda_{s,3}\phi_3^4 - \eta_1\phi_3^3 - (y_{\text{D}} + \eta_2^{2/3}\phi_3^2)^{3/2}, \quad (3.5)$$

where the barrier is induced by vector and temporal-scalar UV contributions; see e.g. [37, 73]. Concretely, for the Abelian Higgs model, the barrier is parametrized by the vector-induced cubic coupling $\eta_1 \sim g_{3,d}^3$, the Debye screening mass $y_{\text{D}} \sim m_{\text{D}}^2$, and the coupling between temporal and Lorentz scalars $\eta_2 \sim h_3^{3/2}$. In three dimensions, the mass dimensions are $[\phi_3] = 1/2$, $[\eta_1] = 3/2$, and $[m_{\text{D}}] = [\lambda_{\phi,3}] = 1$.

In the limit of a strong transition, the barrier is dominated by the field-dependent spatial contributions. Since then $y_{\text{D}} \ll \eta_2^{2/3}\phi_3^2$, the temporal vector contribution reduces to a pure

¹¹Here $m_{s,3}$ denotes the common mass scale of all light scalar degrees of freedom, comprising the physical scalar and its associated Goldstone boson $m_{\chi,3}$. Although in R_ξ gauge the Goldstone mass can reach $m_{\chi,3} \sim m_{V,3}$ individually, the Goldstone and ghost contributions combine to give a ultrasoft net correction [138].

cubic term, and the potential simplifies to the form

$$V_{\text{eff}}^{\text{bro}}(\phi_3) = \frac{1}{2}\mu_{s,3}^2\phi_3^2 + \frac{1}{4}\lambda_{s,3}\phi_3^4 - \eta\phi_3^3, \quad (3.6)$$

which has the same structure of the LO potential of (EFT2). Here, however, $\eta = \eta_1 + \eta_2$ is the effective cubic coupling where the first term is the pure vector contribution from $\eta_1 = g_{d,3}^3/(6\pi)$, and the second term is the contribution from the temporal vector. In the Abelian Higgs model, the temporal and vector induced radiative contributions combine to

$$(d-3)J_3(m_{V,3}) + J_3(m_{V_0}) = \frac{1}{12\pi} \left(2m_{V,3}^3 + m_{V_0}^3 \right) = \frac{g_{d,3}^3}{6\pi} \left(1 + \frac{1}{2}\tilde{h}_3^{3/2} \right) \phi_3^3 = g_{d,3}^3 \mathcal{E}_1 \phi_3^3, \quad (3.7)$$

where \tilde{h}_3 and \mathcal{E}_1 are defined in eqs. (3.12) and (3.13) and $J_3(m)$ is defined in eq. (A.12). The modified cubic barrier amounts to installing an effective gauge coupling $g_{\text{eff}}^2 = g_{d,3}^2 \mathcal{E}_1^{2/3}$ which in turn yields an effectively larger barrier giving rise to stronger transitions. Henceforth, we will display all quantities in units of $\eta \equiv g_{d,3}^3$.

Rescaling $\phi_3 = \eta^{1/3}\varphi$, with φ the dimensionless scalar background, the LO potential can be written in its dimensionless form [139–143]

$$\tilde{V}_{\text{eff}}^{\text{bro}} \equiv \frac{V_{\text{eff}}^{\text{bro}}(\phi_3)}{\eta^2} = \frac{1}{2}y\varphi^2 + \frac{1}{4}x\varphi^4 - \mathcal{E}_1\varphi^3, \quad x \equiv \frac{\lambda_{s,3}}{\eta^{2/3}}, \quad y \equiv \frac{\mu_{s,3}^2}{\eta^{4/3}}. \quad (3.8)$$

In this context, the strongest transitions occur for $x \lesssim 0.18$ [73], with larger values of η further enhancing the transition strength.

Both the symmetric- and broken-phase effective potentials are known to N⁴LO in this setup [72]. In our numerical scans, we modify those results by accounting for temporal vector effects up to NNLO, following [135] in Landau gauge [98],

$$\tilde{V}_{\text{eff}}^{\text{bro}}|_{\text{NLO}} = -\frac{\tilde{g}_{d,3}^4\varphi^2}{(4\pi)^2} \left[\mathcal{E}_2 + \mathcal{E}_3 \ln \frac{\tilde{\mu}_{3d}^2}{4m_V^2} \right], \quad (3.9)$$

$$\tilde{V}_{\text{eff}}^{\text{bro}}|_{\text{NNLO}} = -\frac{1}{12\pi} \left[(\tilde{m}_{s,3}^2)^{\frac{3}{2}} + (\tilde{m}_{\chi,3}^2)^{\frac{3}{2}} \right], \quad (3.10)$$

$$\tilde{V}_{\text{eff}}^{\text{sym}}|_{\text{NNLO}} = -\frac{1}{6\pi} y^{\frac{3}{2}}, \quad (3.11)$$

using the temporal vector enhancement factors

$$\mathcal{E}_1 \equiv \frac{1}{6\pi} \left(1 + \frac{1}{2}\tilde{h}_3^{3/2} \right), \quad \mathcal{E}_2 \equiv 1 + \frac{1}{2}\tilde{h}_3^2 (1 - \ln \tilde{h}_3) + 3\tilde{\kappa}_3\tilde{h}_3, \quad \mathcal{E}_3 \equiv 1 + \frac{1}{2}\tilde{h}_3^2. \quad (3.12)$$

The dimensionless versions of the effective gauge coupling, the coupling between temporal and Lorentz scalars, and the self-coupling of the temporal vectors are defined as

$$\tilde{g}_{d,3}^2 = \frac{g_{d,3}^2}{\eta^{2/3}}, \quad \tilde{h}_3 = \frac{h_3}{\eta^{2/3}}, \quad \tilde{\kappa}_3 = \frac{\kappa_3}{\eta^{2/3}}. \quad (3.13)$$

Setting $\mathcal{E}_1 = 1/(6\pi)$ and $\mathcal{E}_2 = \mathcal{E}_3 = \tilde{g}_{d,3}^4 = 1$ recovers the results of [72,137]. The dimensionless resummed field-dependent scalar masses appearing in eq. (3.10) are

$$\begin{aligned}\partial_\varphi^2 \tilde{V}_{\text{eff}}^{\text{bro}} &= \tilde{m}_{s,3}^2 \equiv \frac{m_{s,3}^2}{\eta^{4/3}} = y + 3x\varphi^2 - 6\mathcal{E}_1\varphi, \\ \varphi^{-1} \partial_\varphi \tilde{V}_{\text{eff}}^{\text{bro}} &= \tilde{m}_{\chi,3}^2 \equiv \frac{m_{\chi,3}^2}{\eta^{4/3}} = y + x\varphi^2 - 3\mathcal{E}_1\varphi.\end{aligned}\quad (3.14)$$

For the effective action, rescaling the spatial coordinates and scalar background as $\mathbf{x} \rightarrow \tilde{\mathbf{x}} y^{-\frac{1}{2}} \eta^{-\frac{2}{3}}$ and $\varphi \rightarrow y/\mathcal{E}_1\varphi$, the LO action takes the form

$$\begin{aligned}S_{\text{LO}} &= \int_{\mathbf{x}} \left\{ \frac{1}{2} (\partial_i \phi_{\text{B}})^2 + V_{\text{eff}}^{\text{LO}}(\phi_{\text{B}}) \right\} \\ &= \kappa \int_{\tilde{\mathbf{x}}} \left\{ \frac{1}{2} (\tilde{\partial}_i \varphi_{\text{B}})^2 + \frac{1}{2} \varphi_{\text{B}}^2 + \frac{\gamma}{4} \varphi_{\text{B}}^4 - \varphi_{\text{B}}^3 \right\} \equiv \kappa \tilde{S}_{\text{LO}}(\gamma),\end{aligned}\quad (3.15)$$

where $\kappa = y^{3/2}/\mathcal{E}_1^2$ and $\gamma = xy/\mathcal{E}_1^2$. The bounce solution $\phi_{\text{B}} = \phi_{\text{B}}(\mathbf{x})$ is obtained by solving the bounce equation of motion and φ_{B} is the dimensionless bounce solution. By further shifting $\mathcal{E}_1 \rightarrow 2\mathcal{E}_1$ and $x \rightarrow 2x$ or $\kappa \rightarrow \tilde{\kappa} = \kappa/4$ and $\gamma \rightarrow \tilde{\gamma} = \gamma/2$, we can ensure that $\tilde{\gamma}(y_c) = 1$ at the critical temperature T_c ; see eq. (3.34) for the definition of y_c . This way one can expand the dimensionless action $\tilde{S}_{\text{LO}}(\tilde{\gamma})$ around $\tilde{\gamma} = 1$, which admits the fit [140,143–146]

$$f(\tilde{\gamma}) = c_1 + c_2\tilde{\gamma} + c_3\tilde{\gamma}^2 + c_4(1 - \tilde{\gamma})^{-1} + c_5(1 - \tilde{\gamma})^{-2} + c_6(1 - \tilde{\gamma})^{-3}, \quad (3.16)$$

provided that $\tilde{\gamma} < 1$. Naturally, $\tilde{S}_{\text{LO}}(\tilde{\gamma})$ diverges as $\tilde{\gamma} \rightarrow 1$, which corresponds to the limit of a vanishing barrier and tunneling rate. The bounce solution $\phi_{\text{B}}(\mathbf{x})$ is then obtained numerically using `BubbleDet` [147] and `CosmoTransitions` [148], with the fitting coefficients listed in tab. 1; we also verified the results using `FindBounce` [149]. For a more general fitting approach of bounce actions see [150].

At NLO and in derivative expansion, the effective action receives contributions from the wave-function renormalization of the scalar field and from the vector-induced two-loop effective potential (3.9),

$$\begin{aligned}S_{\text{NLO}} &= \int_{\mathbf{x}} \left\{ \frac{Z(\phi_{\text{B}})}{2} (\partial_i \phi_{\text{B}})^2 + V_{\text{eff}}^{\text{bro}}|_{\text{NLO}}(\phi_{\text{B}}) \right\} \\ &= \frac{y^{\frac{1}{2}}}{\mathcal{E}_1} \int_{\tilde{\mathbf{x}}} \left\{ \frac{\tilde{g}_{d,3}}{48\pi} \frac{\mathcal{E}_Z}{2} \frac{(\tilde{\partial}_i \varphi_{\text{B}})^2}{\varphi_{\text{B}}} - \frac{\tilde{g}_{d,3}^4 \varphi_{\text{B}}^2}{(4\pi)^2} \left(\frac{\mathcal{E}_2}{\mathcal{E}_1} + 2 \frac{\mathcal{E}_3}{\mathcal{E}_1} \ln \frac{\tilde{\mu}_{3\text{d}} \mathcal{E}_1}{2y\tilde{g}_{d,3}\varphi_{\text{B}}} \right) \right\}.\end{aligned}\quad (3.17)$$

The NLO action is evaluated on the LO bounce solution $\phi_{\text{B}} = \phi_{\text{B}}^{\text{LO}}$, and scales as $\mathcal{O}(y^{1/2})$ compared to S_{LO} (3.15). The kinetic enhancement factor is defined in eq. (3.19) and is $\mathcal{E}_Z = -22$ in the absence of temporal vector contributions. Here, $\tilde{\mu}_{3\text{d}} = \eta^{-2/3} \bar{\mu}_{3\text{d}}$ is the dimensionless 3d renormalization scale.

| Action | c_1 | c_2 | c_3 | c_4 | c_5 | c_6 |
|--|----------|---------|----------|-----------|------------|--------------|
| $\tilde{S}_{\text{LO}}(\tilde{\gamma})$ | 7.674(7) | 4.26(3) | 1.11(5) | 10.413(2) | 1.24396(6) | 0 |
| $\tilde{S}_{\text{NLO}}^{(a)}(\tilde{\gamma})$ | 55.72(3) | 15.9(1) | -16.7(2) | 53.040(9) | 5.5867(3) | 0 |
| $\tilde{S}_{\text{NLO}}^{(b)}(\tilde{\gamma})$ | 30.5(2) | 17(1) | 36(2) | 3.17(7) | 20.182(2) | 4.95936(2) |
| $\tilde{S}_{\text{NLO}}^{(c)}(\tilde{\gamma})$ | 20.1(3) | 7(2) | 75(2) | -34.9(1) | 19.019(3) | 6.87518(2) |
| $\tilde{S}_{\text{NNLO}}^s(\tilde{\gamma})$ | 1.5(2) | 2.0(7) | -5(1) | 3.40(5) | 0.548(1) | 0 |
| $\tilde{S}_{\text{NNLO}}^\chi(\tilde{\gamma})$ | 1.046(3) | 0.50(1) | -1.38(2) | 1.5133(9) | 0.46924(3) | 0.0328801(2) |

Table 1: Fitting coefficients for the LO dimensionless action $\tilde{S}_{\text{LO}}(\gamma)$ (3.15), the individual building blocks $\tilde{S}_{\text{NLO}}^{(a)-(c)}(\tilde{\gamma})$ of the NLO action (3.17), and the NNLO scalar and Goldstone fluctuation-determinant contributions $\tilde{S}_{\text{NNLO}}^{s,\chi}(\tilde{\gamma})$. Fits are obtained using `BubbleDet` [147] and `CosmoTransitions` [148]; uncertainties stem from the fitting procedure. See [143] for a similar construction.

The wave-function renormalization term $\propto Z(\phi_{\text{B}})$ is obtained from the NLO term in the derivative expansion in $\partial_i \sim m_{V,3}, m_{V_0}$ of the spatial and temporal vector fluctuation determinant [37, 66, 67],

$$Z(\phi_3) = \frac{1}{48\pi} \left[-\frac{22g_{d,3}}{\phi_3} + \frac{h_3^2 \phi_3^2}{m_{V_0}^3} \right] \stackrel{h_3 \phi_3^2 \gg m_{\text{D}}^2}{=} \frac{1}{48\pi} \frac{g_{d,3}}{\phi_3} \mathcal{E}_Z. \quad (3.18)$$

The second equality is obtained in the limit of a strong transition, where the field-dependent mass contribution dominates over the Debye mass, $h_3 \phi_3^2 \gg m_{\text{D}}^2$, (cf. (3.6)), and yields the following enhancement

$$\mathcal{E}_Z \equiv -22 + \tilde{h}_3^{\frac{1}{2}}, \quad (3.19)$$

with $\tilde{h}_3 = 1 + \mathcal{O}(g_d^2)$. In comparison to the temporal vector-induced enhancement of the cubic barrier (3.12), the enhancement of the wave-function renormalization term is small and of $\mathcal{O}(1\%)$ compared to the pure spatial vector contribution.

While the wave-function renormalization term (3.18) is often neglected in the PTA literature, e.g. [42, 151], including the full NLO action is required for the nucleation rate to be gauge invariant at NLO [66, 67]. In classically conformal models, where the scalar mass arises entirely from radiative corrections, the contribution of $Z(\phi_{\text{B}})$ has been found to significantly affect the nucleation rate [36] and can even signal the breakdown of the derivative expansion itself [37, 38] when $\partial_i \sim m_{V,3}$ vanishes at the bounce tail.

After identifying the building blocks of the NLO action in eq. (3.17),

$$\tilde{S}_{\text{NLO}}^{(a)} = \int_{\tilde{\mathbf{x}}} \frac{(\tilde{\partial}_i \varphi_{\text{B}}(\tilde{\mathbf{x}}))^2}{\varphi_{\text{B}}(\tilde{\mathbf{x}})}, \quad \tilde{S}_{\text{NLO}}^{(b)} = \int_{\tilde{\mathbf{x}}} \varphi_{\text{B}}^2(\tilde{\mathbf{x}}), \quad \tilde{S}_{\text{NLO}}^{(c)} = \int_{\tilde{\mathbf{x}}} \varphi_{\text{B}}^2(\tilde{\mathbf{x}}) \ln \varphi_{\text{B}}^2(\tilde{\mathbf{x}}), \quad (3.20)$$

their dimensionless forms are fitted to the same functional form (3.16), with coefficients listed in tab. 1.

The NNLO contribution to the bounce action arises from the scalar and Goldstone fluctuation determinants, $\tilde{S}_{\text{NNLO}}^s(\tilde{\gamma})$ and $\tilde{S}_{\text{NNLO}}^X(\tilde{\gamma})$, again evaluated around the LO bounce solution $\phi_{\text{B}}^{\text{LO}}$. In principle, these contributions can be approximated via $A_{\text{dyn}} \times \det_S \approx T^4$ in the nucleation rate, which has been shown to be a robust approximation [37]. Here we instead compute them via their full determinant [143] using `BubbleDet` [147], and fit the results to the functional form (3.16); the coefficients are listed in tab. 1.

3.2. Phase transition thermodynamics

The current state-of-the-art assumption in computing GW signals from first-order phase transitions is that the spectrum depends on a few microphysical thermodynamic parameters [152]. One central quantity is the free energy, or equivalently the pressure $p(T)$, that encodes the thermodynamic equilibrium behavior.

This section details the computation of the thermodynamic quantities relevant for computing the GW spectrum, including the critical temperature T_c , the percolation temperature T_p , the transition strength α ,¹² the inverse duration β/H , the symmetric-phase sound speed c_s , and the bubble wall velocity v_w . Below, all phase-transition quantities are referenced to the percolation temperature [153] such that

$$T_\star = T_p. \quad (3.21)$$

In turn, we will encounter the following thermodynamic quantities consisting of the pseudo-trace anomaly $\bar{\theta}$ [154, 155], the energy density e , enthalpy density w , entropy density s , and sound speed c_s ,

$$\bar{\theta} \equiv e - \frac{p}{c_{s,\text{bro}}^2}, \quad e = T \frac{\partial p}{\partial T} - p, \quad w = T \frac{\partial p}{\partial T}, \quad s = \frac{w}{T}, \quad c_s = \frac{\partial p}{\partial T} \bigg/ \frac{\partial e}{\partial T}, \quad (3.22)$$

which are valid both in the symmetric (sym) and broken (bro) phase. For generic thermodynamic quantities $X = \{\bar{\theta}, e, p, w, V_{\text{eff}}, \dots\}$, we define the symmetric- and broken-phase difference

$$\Delta X(T) = X_{\text{sym}}(T) - X_{\text{bro}}(T), \quad (3.23)$$

and the thermal derivatives $X' = \partial_T X$.

In the high-temperature expansion, the pressure for the symmetric and broken phases takes the form

$$p_i = p_0 - T F_i, \quad F_i = V_{\text{eff}}^i(\phi_{\text{min}}), \quad i \in \{\text{bro}, \text{sym}\}, \quad (3.24)$$

¹²Not to be confused with the gauge coupling combination $\alpha_d = g_d^2/4\pi$.

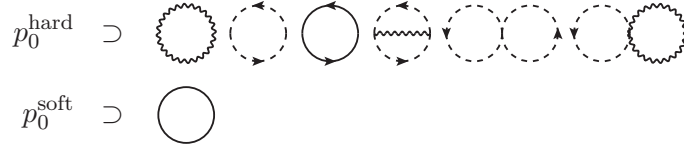


Figure 2: One-loop and two-loop vacuum diagrams contributing to the dark-sector hard p_0^{hard} (3.25) and soft p_0^{soft} (3.26) unit operator in the high-temperature expansion computed in the symmetric phase. Wiggly lines indicate the vector bosons V_μ , dashed directed lines the scalars S , solid directed lines the fermions X , and solid undirected lines the temporal vectors V_0 .

where F_i is the free energy, namely the effective potential of the 3dEFT evaluated at its minimum for each phase. The unit operator p_0 is the symmetric, field-independent pressure [63, 156, 157]. The latter consists of a hard and a soft contribution $p_0 = p_0^{\text{hard}} + p_0^{\text{soft}}$ as displayed in fig. 2. These contributions originate from thermal corrections to the vacuum. For the dark sector, up to NNLO, they take the form

$$\begin{aligned}
p_0^{\text{hard}} &= T^4 \left[g_{\text{eff,DS}}^{\text{B}} \frac{\zeta_4}{\pi^2} - \frac{5g_d^2(1+n_G) + 4\lambda_s}{288} + \frac{1}{12} \frac{\mu_s^2}{T^2} \right] \\
&\quad - \frac{\mu_X^4}{4(4\pi)^2} \left[\ln \frac{\bar{\mu}^2}{\mu_X^2} + \frac{3}{2} \right] + \tilde{J}_X^T + \mathcal{O}(g^3 T^4) \\
&\stackrel{m_i \ll T}{=} T^4 \left[g_{\text{eff,DS}} \frac{\zeta_4}{\pi^2} - \frac{5g_d^2(1+n_G) + 4\lambda_s}{288} + \frac{1}{12} \frac{\mu_s^2 - \mu_X^2}{T^2} + \mathcal{O}\left(g^3 T^4, \frac{\mu_s^4}{T^4}, \frac{\mu_X^4}{T^4}\right) \right], \quad (3.25)
\end{aligned}$$

$$p_0^{\text{soft}} = -\frac{T}{12\pi} m_{\text{D}}^3 + \mathcal{O}(g^5 T^4), \quad (3.26)$$

where $g_{\text{eff,DS}}^{\text{B}}$ denotes the bosonic relativistic degrees of freedom, and in the third line we applied the high-temperature expansion. Here, $\zeta_4 = \pi^4/90$, and $\zeta_s = \zeta(s)$ for $\text{Re}(s) > 1$ is the Riemann zeta function. The divergence at m_X^4/ϵ in the hard \tilde{J}_X^T in eq. (A.17) is cancelled by the potential 4d counterterm [157, 158] and the thermal master integral is defined in eq. (A.23). The NNLO contribution to the unit operator, originating from hard three-loop vacuum diagrams, can readily be included by using DRalgo [129].

In thermal equilibrium, the relativistic degrees of freedom of the dark sector, $g_{\text{eff,DS}}$, and of the SM, $g_{\text{eff,SM}}$ [113], add up to the total number

$$g_{\text{eff,tot}} = g_{\text{eff,SM}} + g_{\text{eff,DS}}, \quad (3.27)$$

$$g_{\text{eff,DS}} = \underbrace{2}_S (\text{scalars}) + \underbrace{2}_{V_\mu} (\text{vectors}) + \frac{7}{8} \left[\underbrace{4n_G}_{\bar{X}, X} \right] (\text{fermions}) = \frac{8 + 7n_G}{2}, \quad (3.28)$$

where each (anti)fermion contributes a factor of 2 from spin degrees of freedom. At the transition temperatures considered in this work, $T_\star \sim \mathcal{O}(\text{MeV})$, the dark fermion is non-

relativistic for the dark matter masses of interest, and therefore $g_{\text{eff,DS}} = g_{\text{eff,DS}}^{\text{B}}$.¹³ If the visible and dark sectors are also hydrodynamically coupled, $g_{\text{eff,hyd}} = g_{\text{eff,tot}}$ (cf. sec. 3.2.1).

The critical temperature T_c , or critical mass y_c , is determined from the degeneracy condition of the free energy between the symmetric and broken phase,

$$\begin{aligned} \Delta F(y_c(x), x) &= [F_{\text{sym}} - F_{\text{bro}}](y_c(x), x) \\ &= \left[\Delta F_{\text{LO}} + x \Delta F_{\text{NLO}} + x^{\frac{3}{2}} \Delta F_{\text{NNLO}} + \mathcal{O}(x^2) \right]_{y=y_c(x)} = 0, \end{aligned} \quad (3.29)$$

where x and y are the dimensionless variables defined in eq. (3.8). From the second line, this condition can be solved up to N⁴LO in a strict perturbative series [72, 136] after expanding

$$y_c = y_c^{\text{LO}} + x y_c^{\text{NLO}} + x^{\frac{3}{2}} y_c^{\text{NNLO}} + x^2 y_c^{\text{N}^3\text{LO}} + x^{\frac{5}{2}} y_c^{\text{N}^4\text{LO}}, \quad (3.30)$$

$$\phi_{\text{min}} = \phi_0 + x \phi_1 + x^{\frac{3}{2}} \phi_2 + \mathcal{O}(x^2). \quad (3.31)$$

The power-counting parameter x indicates the suppression of higher-order terms since the expansion is organized in powers of x and not by loops. Focusing on the NNLO result, all terms of the effective potential are evaluated at the minimum, $\phi_{\text{min}} = \eta^{1/3} \varphi_{\text{min}}$, at LO [46]

$$\varphi_{\text{min}} = \frac{3\mathcal{E}_1 + \sqrt{9\mathcal{E}_1^2 - 4xy}}{2x}, \quad \varphi_{\text{min,c}} = \frac{2\mathcal{E}_1}{x}, \quad (3.32)$$

where we also displayed the critical value of the minimum $\varphi_{\text{min,c}}$.

After solving eq. (3.29) order by order in x , the individual orders of the critical mass y_c are given by

$$\Delta F_{\text{LO}} \Big|_{y=y_c^{\text{LO}}} = 0, \quad y_c^{\text{NLO}} = - \frac{\Delta F_{\text{NLO}}}{\partial_y \Delta F_{\text{LO}}} \Big|_{y=y_c^{\text{LO}}}, \quad y_c^{\text{NNLO}} = - \frac{\Delta F_{\text{NNLO}}}{\partial_y \Delta F_{\text{LO}}} \Big|_{y=y_c^{\text{LO}}}. \quad (3.33)$$

The resulting NNLO critical mass y_c with $\tilde{\mu}_3 = (x \tilde{\mu}_{3d} / \mathcal{E}_1) \exp\{\frac{\mathcal{E}_2}{2\mathcal{E}_3} - 2 \ln 2\}$ is [72, 136, 159]

$$y_c \Big|_{\text{NNLO}} = \frac{2}{x} \mathcal{E}_1^2 + \frac{\mathcal{E}_2}{(2\pi)^2} \ln \tilde{\mu}_3 - \frac{\mathcal{E}_1}{6\pi} \left(\frac{x}{2}\right)^{\frac{1}{2}}, \quad (3.34)$$

and gauge independent order by order in x [137]. The temporal vector enhancement factors $\mathcal{E}_{1,2}$ are defined in eq. (3.12). The critical mass y_c is depicted in fig. 3 (left) as a function of x together with lattice data points from [46, 94, 126] and the final orders N³LO and N⁴LO from [72]. The critical temperature can then be obtained by inverting the relation $y(T_c) = y_c$. By using the LO matching relations of appendix C, and the leading term of eq. (3.34), one can recover the LO expression

$$T_c^{\text{LO}} = \mu_s \left(\frac{4\lambda_s + 3g_d^2}{12} - \frac{2g_d^6 \mathcal{E}_1^2}{\lambda_s} \right)^{-1/2}, \quad (3.35)$$

¹³The precise choice of the dark-sector $g_{\text{eff,DS}}$ is less important, since it can always be absorbed by slightly redefining the temperature T_{reh} at reheating of eq. (3.40).

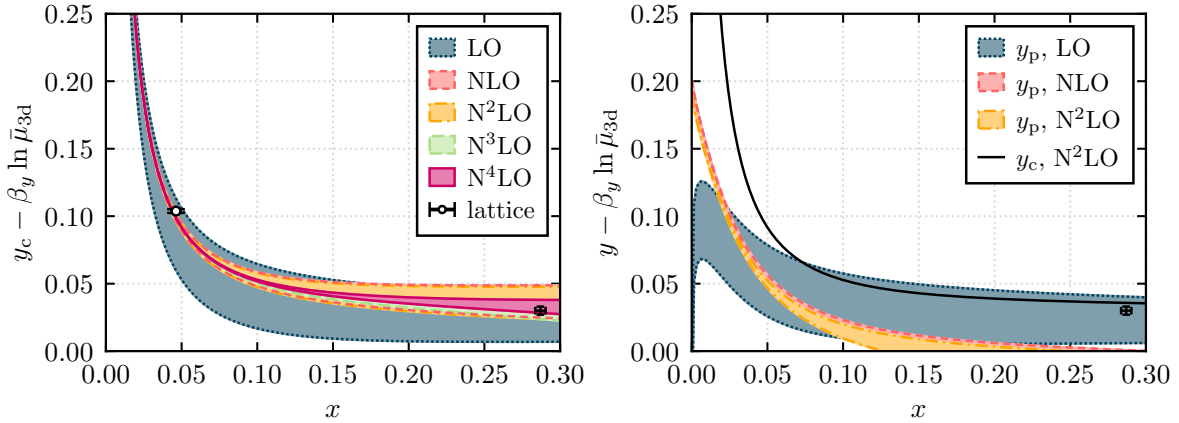


Figure 3: The renormalization-scale invariant quantity $\tilde{y}_{c,p} = y_{c,p} - \beta_y \ln \bar{\mu}_{3d}$, where y_c is the critical mass (left), y_p the percolation mass (right), $\bar{\mu}_{3d}$ the renormalization scale, and β_y the β -function for y from [72]. Uncertainties for the perturbative calculations are shown as error bands by varying $\bar{\mu}_{3d}/(2m_V) = [10^{-\frac{1}{2}}, 10^{\frac{1}{2}}]$. Left: The theoretical uncertainty for the lattice data points from [46, 94, 126] are shown as error bars. The line of first-order phase transitions ends in a second-order transition at $x \sim 0.3$ [94]. The orders NLO and NNLO are almost identical. Right: Comparison between y_p fulfilling the condition (3.39) and y_c at NNLO.

which restricts the parameter range (g_d, λ_s) for which a first-order transition is realized to a positive argument of the square root. Larger temporal vector contributions increase \mathcal{E}_1 and thus T_c^{LO} .

To compute the percolation temperature T_p , or the percolation mass y_p as a function of x , one can follow a similar strategy [143, 144]. After taking the LO action from eq. (3.15), the defining equation, is the percolation criterion [160, 161]

$$S_{\text{eff}} = \left[S_{\text{LO}} + x S_{\text{NLO}} + x^{\frac{3}{2}} S_{\text{NNLO}} + \mathcal{O}(x^2) \right]_{y=y_p(x)} = \mathcal{F}[H(T_p)], \quad (3.36)$$

$$y_p = y_p^{\text{LO}} + x y_p^{\text{NLO}} + x^{\frac{3}{2}} y_p^{\text{NNLO}}, \quad (3.37)$$

which is also solved order by order in the expansion parameter x . Up to NNLO, the individual gauge-independent orders of y_p are by

$$S_{\text{LO}} \Big|_{y=y_p^{\text{LO}}} = \mathcal{F}[H(T_p)], \quad y_p^{\text{NLO}} = - \frac{S_{\text{NLO}}}{\partial_y S_{\text{LO}}} \Big|_{y=y_p^{\text{LO}}}, \quad y_p^{\text{NNLO}} = - \frac{S_{\text{NNLO}}}{\partial_y S_{\text{LO}}} \Big|_{y=y_p^{\text{LO}}}, \quad (3.38)$$

and depicted in fig. 3 (right) as a function of x . The percolation criterion in eq. (3.36) depends on \mathcal{F} which is a function of the Hubble parameter $H(T)$; see eq. (2.11) for its definition during radiation domination. Here, we set $\mathcal{F}[H(T_p)]$ to be a constant [162], and impose the standard percolation condition, for which the probability that a given spatial point remains in the false

vacuum, $P(T_p) = e^{-I(T_p)} \simeq 71\%$, corresponds to $I(T_p) = 0.34$ [160, 161]. This yields

$$\begin{aligned} \mathcal{F}[H(T_p)] &\approx \ln I(T_p) + \ln(8\pi) + 3 \ln v_w + \ln \frac{A}{H^4} - 4 \ln \frac{\beta}{H} \\ &= 181.6 + \ln I(T_p) + 3 \ln v_w + \ln \frac{A}{T_p^4} - 4 \ln \frac{\beta/H_\star}{100} - 2 \ln \frac{g_{\text{eff,tot}}}{10} - 4 \ln \frac{T_p}{1 \text{ MeV}}, \end{aligned} \quad (3.39)$$

where in our numerical studies, we use $\ln(A/T_p^4) \simeq -14$ [163], and the ansatz $\beta/H_\star \simeq 100$, $v_w \simeq 1$, $g_{\text{eff,tot}} \simeq 10$, and $T_p \simeq 1 \text{ MeV}$. In practice, the percolation criterion is not very sensitive to the precise choice of these parameters but a fully general computation would require a self-consistent solution of the percolation criterion together with the thermodynamic parameters.

For strong supercooling where $T_p \ll T_c$ and α is large, or very strong transitions where a lot of energy is stored in the form of vacuum energy that later reheats the universe when the transition ends, the reheating temperature can differ significantly from the percolation temperature $T_\star = T_p$ [164],

$$T_{\text{reh}} \approx T_\star (1 + \alpha_\star)^{1/4}. \quad (3.40)$$

The phase-transition strength is most suitably computed from the pseudotrace anomaly [154, 155] defined in eq. (3.22),

$$\alpha = \frac{\Delta \bar{\theta}}{3 \omega_{\text{sym}}} = \frac{1}{3 p'_{\text{sym}}} \left(\frac{\Delta F}{c_{s,\text{bro}}^2} - \Delta \frac{dF}{d \ln T} \right). \quad (3.41)$$

The inverse duration depends on the action $S_3 = S_{\text{LO}} + x S_{\text{NLO}} + x^{3/2} S_{\text{NNLO}} + \dots$ fitted in tab. 1, and, after applying the chain rule, it factorizes into

$$\beta/H \simeq \frac{d \ln \Gamma}{d \ln T} = (\eta_y \partial_y + \eta_x \partial_x) S_3, \quad (3.42)$$

with $\tau = \ln T$ and $\eta_\kappa = \partial_\tau \kappa$ encoding the thermal running of the EFT parameters [165].

The subsequent bubble-wall hydrodynamics is controlled by the sound speeds in the broken phase $c_{s,\text{bro}}$ and in the symmetric phase $c_{s,\text{sym}}$, as well as the enthalpy ratio across the wall,

$$\Psi = \frac{\omega_{\text{bro}}}{\omega_{\text{sym}}} \approx 1 - \frac{1}{p'_0} \left(F_{\text{bro}} + \frac{dF_{\text{bro}}}{d \ln T} \right). \quad (3.43)$$

The kinetic energy fraction [154, 155, 166] is determined by the kinetic energy density in the fluid ρ_{fl} and the total energy density of the plasma e_{sym} [167],

$$K = \frac{\rho_{\text{fl}}}{e_{\text{sym}}} = \kappa_{\text{sw}}(\alpha_{\star,\text{hyd}}) \alpha_{\star,\text{tot}} \frac{3}{4} \Gamma_{\text{ad}}, \quad (3.44)$$

and is related to the efficiency factor $\kappa_{\text{sw}}(\alpha_{\star,\text{hyd}})$. The latter quantifies the fraction of the latent heat deposited into bulk fluid motion, rather than reheating the plasma, and depends on $\alpha_{\star,\text{hyd}}$, the transition strength normalized to the energy density of the hydrodynamically active sector. Here, $\Gamma_{\text{ad}} = \omega_{\text{sym}}/e_{\text{sym}}$ is the adiabatic index of the symmetric phase, and $\alpha_{\star,\text{tot}}$ is the total transition strength, both evaluated using the total relativistic degrees of freedom $g_{\text{eff,tot}}$ of eq. (3.27). The condition for hydrodynamic equilibrium is discussed in sec. 3.2.1.

Imposing local thermal equilibrium (LTE) across the wall, an upper limit on the terminal wall velocity v_w [162] follows from the hydrodynamic matching conditions together with entropy conservation. The wall velocity v_w and the sound-wave efficiency factor κ_{sw} are then fully determined by [168]¹⁴

$$v_w = v_w(\alpha_{\star,\text{hyd}}, \Psi, c_{s,\text{sym}}, c_{s,\text{bro}}), \quad \kappa_{\text{sw}} = \kappa_{\text{sw}}(\alpha_{\star,\text{hyd}}, \Psi, c_{s,\text{sym}}, c_{s,\text{bro}}). \quad (3.45)$$

Alternatively, the efficiency factor $\kappa_{\text{sw}} = \kappa_{\text{sw}}(\alpha, v_w)$ can be taken from [171, 172], in which case v_w is treated as an input.

For the strongest transitions encountered in this work, detonations with $v_w \simeq 1$ can occur. Throughout, we adopt the LTE upper bound on v_w^{LTE} using the implementation of [168]. A general perturbative determination of v_w requires including out-of-equilibrium effects [173–175], as recently automated in [176–178]. In the detonation regime, where $v_w \simeq 1$, one has $\kappa_{\text{sw}}(\alpha, 1) = \kappa_{\text{sw}}(\alpha)$ and both the efficiency factor and the kinetic energy fraction are well approximated by [171, 179]

$$K = 0.6 \kappa_{\text{sw}}(\alpha_{\star,\text{hyd}}) \frac{\alpha_{\star,\text{tot}}}{1 + \alpha_{\star,\text{tot}}}, \quad \kappa_{\text{sw}}(\alpha) \approx \frac{\alpha}{0.73 + 0.083 \sqrt{\alpha} + \alpha}. \quad (3.46)$$

Besides κ_{sw} , the wall velocity also sets the sound-shell thickness Δ_w of eq. (3.54).

3.2.1. Hydrodynamic equilibrium and decoupling

Besides the thermal equilibration condition (2.10), we also examine the hydrodynamic contact between the SM and dark sectors. The relevant criterion is whether the mean free path for SM–DS momentum exchange is shorter than the mean bubble separation $R \sim v_w/\beta$, the characteristic length scale of the bubble hydrodynamics. This translates to the condition

$$C_{\text{hyd}}^{\text{eq}} : \quad \Gamma_{\text{int}} \cdot R \gtrsim 1, \quad (3.47)$$

where Γ_{int} is the total SM–DS interaction rate of eq. (2.10). Depending on whether this condition is satisfied, all thermodynamic quantities entering the hydrodynamics are evaluated either in the dark sector alone or in the full plasma of eq. (3.27), motivating two distinct transition strengths:

¹⁴A lower bound on v_w can in principle be obtained from the ballistic approximation [169]. It has also been shown that the LTE upper bound cannot always be saturated, as entropy production across the wall persists even in the zero-friction limit [170].

$\alpha_{\star,\text{hyd}}$: normalized to the energy density of the hydrodynamically active sector, this governs the bubble-wall dynamics and efficiency factor κ_{sw} in eq. (3.44).

$\alpha_{\star,\text{tot}}$: normalized to the full relativistic energy density of eq. (3.27), this sets the overall amplitude of the GW signal through eq. (3.44).

The two strengths can differ significantly when the condition (3.47) is not met.

3.3. Gravitational wave spectrum

A first-order phase transition proceeds through the nucleation and expansion of bubbles of the broken phase, whose dynamics sources GWs in the early universe [10,180]. Three mechanisms have been identified that may linearly combine into the total stochastic gravitational-wave background (SGWB),

$$\Omega_{\text{GW}}h^2 \simeq \Omega_{\text{coll}}h^2 + \Omega_{\text{sw}}h^2 + \Omega_{\text{turb}}h^2, \quad (3.48)$$

namely bubble-wall collisions and shocks [167], sound waves expanding into the plasma [181,182], and magnetohydrodynamic (MHD) turbulence in the post-collision plasma [183]. An additional source of feebly interacting particles has been identified recently [184]. In the parameter range relevant for our analysis (cf. tab. 2), the bubbles do not run away and the signal is dominated by the sound-wave contribution.

We write the sound-wave spectrum as a peak amplitude times a dimensionless spectral shape function,

$$\Omega_{\text{sw}}h^2 = \mathcal{R}h^2 A_{\text{sw}} K^2 \mathcal{Y}_{\text{sw}}(RH_{\star}) S(f), \quad (3.49)$$

and take $H_0 = 100h \text{ km s}^{-1} \text{ Mpc}^{-1}$ with the observed Hubble parameter today given by $h = 0.6737 \pm 0.0054$ [6].

The overall amplitude structure of eq. (3.49) is common to multiple spectral models, while the spectral shape $S(f)$ and its characteristic frequencies differ. Here, A_{sw} is the simulation-extracted amplitude, K the kinetic energy fraction (3.44), R the mean bubble separation, and the redshift to today reads [53,166]¹⁵

$$\mathcal{R}h^2 = \Omega_{\gamma}h^2 \left(\frac{h_0}{h_{\text{eff,tot}}(T_{\text{reh}})} \right)^{4/3} \frac{g_{\text{eff,tot}}(T_{\text{reh}})}{g_{\gamma}}, \quad (3.50)$$

with $\Omega_{\gamma}h^2 = 2.473 \times 10^{-5}$ is the radiation redshift today [6], $g_{\gamma} = 2$, and $h_0 = 3.930$ [185]. Here, $g_{\text{eff,tot}}(T_{\text{reh}})$ and $h_{\text{eff,tot}}(T_{\text{reh}})$ denote the total number of relativistic energy and entropy degrees of freedom in the thermalised SM and dark sector bath after reheating at the end

¹⁵The factors \mathcal{R} and $F_{\text{gw},0}$ of [152] are equivalent.

of the phase transition as defined in eq. (3.28). For $T_\star > 0.1$ MeV, it is appropriate to take $g_{\text{eff,tot}}(T_{\text{reh}}) = h_{\text{eff,tot}}(T_{\text{reh}})$ [186].

The finite source lifetime is included through the shock-formation factor [40, 152, 187, 188]

$$\mathcal{Y}_{\text{sw}} = \min\{1, \tau_{\text{sh}} H_\star\}, \quad \tau_{\text{sh}} H_\star \simeq \sqrt{\frac{\Gamma_{\text{ad}}}{K}} RH_\star, \quad (3.51)$$

where τ_{sh} is the shock-formation timescale and $\Gamma_{\text{ad}} = \omega_{\text{sym}}/e_{\text{sym}} \approx 4/3$ is the adiabatic index. The mean bubble separation is set by the inverse duration [152]

$$RH_\star \approx \left(\frac{8\pi}{f_{\text{p}}}\right)^{1/3} \frac{H_\star}{\beta} \max\{v_w, c_{s,\text{bro}}\}, \quad (3.52)$$

with the true-vacuum fraction $P_{\text{t}}(T_{\text{p}}) \equiv f_{\text{p}} \simeq 0.28957$ at percolation [189–191]. The Hubble rate at percolation redshifted to today is common to a generic GW spectrum [166]

$$H_{\star,0} = a_\star H_\star = 11.2 \times 10^{-9} \text{ Hz} \left(\frac{T_{\text{reh}}}{100 \text{ MeV}}\right) \left(\frac{g_{\text{eff,tot}}(T_{\text{reh}})}{10}\right)^{1/2} \left(\frac{10}{h_{\text{eff,tot}}(T_{\text{reh}})}\right)^{1/3}. \quad (3.53)$$

We now focus on two specific templates that differ in the spectral shape function and its characteristic breaks.

3.3.1. Single broken power law

The single broken power law extracted from the sound-shell model [152, 167, 182, 192, 193] peaks at a single frequency $f_{\text{sw}}^{\text{peak}}$,

$$S_1(f) = \mathcal{N}_1 \left(\frac{f}{f_{\text{sw}}^{\text{peak}}}\right)^3 \left[\frac{7}{4 + 3(f/f_{\text{sw}}^{\text{peak}})^2}\right]^{7/2}, \quad f_{\text{sw}}^{\text{peak}} = 1.56 \left(\frac{z_p}{10}\right) \left(\frac{a_\star H_\star}{RH_\star}\right), \quad (\text{SBPL})$$

with $\mathcal{N}_1 = \frac{1080}{343} \sqrt{\frac{3}{7}}$ normalizing the respective peak amplitude such that $\int d \ln f S_1(f) \stackrel{!}{=} 3$ [182]. The constant factors $A_{\text{sw}} = 1.2 \times 10^{-2}$ in eq. (3.49), and $z_p \approx 10$ which accounts for the observed peak value $z_p = (kH_\star)_{\text{max}}$, are determined from simulations [182].

3.3.2. Double broken power law

The template for the double broken power law can be determined from the more recent Higgsless simulations [166, 172, 194]. The spectrum develops a plateau between two breaks $f_1 < f_2$ [166, 195],

$$S_2(f) = \mathcal{N}_2 \left(\frac{f}{f_2}\right)^3 \left[1 + \left(\frac{f}{f_1}\right)^2\right]^{-1} \left[1 + \left(\frac{f}{f_2}\right)^4\right]^{-1}, \quad f_1 \simeq 0.2 \left(\frac{a_\star H_\star}{RH_\star}\right), \\ f_2 \simeq \frac{0.5}{\Delta_w} \left(\frac{a_\star H_\star}{RH_\star}\right), \quad (\text{DBPL})$$

where the exact position of the peaks f_1 and f_2 are determined from simulations [194] and are sensitive to the strength of the transition. The normalization factor $\mathcal{N}_2 = \frac{2\sqrt{2}}{\pi} [(1 + f_2^2/f_1^2) + \sqrt{2}f_2/f_1]$, $A_{\text{sw}} \approx 0.11$, and the relative sound-shell thickness [192]

$$\Delta_w = \frac{|v_w - c_{s,\text{bro}}|}{\max\{v_w, c_{s,\text{bro}}\}}. \quad (3.54)$$

Both spectra (SBPL) and (DBPL) share the rising f^3 causality tail in the IR [196], while in the UV the single (double) broken power law falls off as f^{-4} (f^{-3}). In the strong phase-transition limit, $\alpha \gg 1$, the wall velocity saturates to $v_w \simeq 1$, so that the sound-shell thickness $\Delta_w \rightarrow 1 - c_{s,\text{bro}}$ and the two breaks approach each other, $f_2 \sim f_1$. The double broken power law then collapses to an effectively single break and the two templates coincide [166]. The strongest transitions preferred by the PTA data approach this regime and the single broken power law (SBPL) already provides a reasonable leading description of the signal. For the finite values of α and v_w realized in sec. 5, the two breaks remain partially resolved, and we default to the double broken power law (DBPL).

In the sound-wave template (3.49), also the kinetic energy fraction K and the wall velocity v_w are required as additional inputs. In our analysis, we keep both generic albeit choosing v_w at its LTE value introduced below eq. (3.45), fixed by the enthalpy ratio Ψ and the sound speeds [168].

4. Dark matter freeze-out

In this section, we discuss the complementarity between the phase transition dynamics of sec. 3 and dark matter phenomenology. Although dark matter is not the primary focus, the model naturally contains a viable dark matter candidate.

The dark matter candidate is the Dirac fermion X in eq. (2.1) with a vector-like mass term, which therefore constitutes an independent parameter of the model. We adopt this setup to facilitate comparison with previous studies [54], while leaving the more involved scenario in which the dark fermion mass is dynamically generated during the phase transition for future work (see e.g. [46, 56]).

The dark matter fermion undergoes the standard thermal freeze-out mechanism. For the couplings of $g_d \sim \mathcal{O}(1)$ that are considered throughout this work, the dark fermions remain in thermal equilibrium with the plasma at high temperatures. The parameter region relevant for our analysis, is dominated by channels into dark scalars and vector bosons. Annihilations into SM particles are strongly suppressed by the small portal couplings (2.6) and become relevant only after the dark-sector phase transition.

In the parameter region considered here, the dark-matter fermion is significantly heavier than both the physical dark scalar and vector boson masses. Since the freeze-out temperature

is typically given by $T_{\text{fo}} \simeq m_X/25$, one generically finds

$$T_{\text{fo}} \gg T_{\text{c,DS}}, T_{\text{p,DS}}, \quad (4.1)$$

and the processes driving annihilation in the symmetric phase are

$$X\bar{X} \rightarrow VV, \quad X\bar{X} \rightarrow SS^*. \quad (4.2)$$

We have explicitly verified the condition (4.1) by solving the Boltzmann equation (4.6).¹⁶ As discussed in sec. 2.2, the visible and dark sectors remain in thermal equilibrium down to temperatures of $\mathcal{O}(\text{MeV})$ for the range of scalar mixing angles allowed by current constraints; cf. (2.7). It is therefore consistent to describe both sectors with a common temperature $T = T_{\text{DS}} = T_{\text{SM}}$ during the epoch relevant for dark matter freeze-out.

Dark matter annihilation, even when proceeding dominantly into dark-sector states rather than directly into SM particles, can still be constrained by indirect detection probes. This is particularly relevant for dark matter masses below $\mathcal{O}(10^2)$ GeV, where late-time annihilations may lead to observable signatures. In particular, annihilations occurring around the time of recombination inject energy into the primordial plasma and can therefore distort the CMB anisotropy spectrum. More precisely, exotic energy injection modifies the recombination history and alters the optical depth of the CMB. In this regime, the relevant annihilation processes occur in the broken phase of the dark sector, and the dominant channels are

$$X\bar{X} \rightarrow VV, \quad X\bar{X} \rightarrow Vs, \quad X\bar{X} \rightarrow V\chi. \quad (4.3)$$

The strongest constraints on exotic energy injection during recombination are provided by measurements of the CMB anisotropies by the Planck collaboration [6]. Following the model-independent treatment of energy deposition developed in [197], one obtains the approximate bound

$$\langle \sigma_{\text{ann}} v_{\text{rel}} \rangle \lesssim 2.6 \times 10^{-27} \left(\frac{m_X}{\text{GeV}} \right) \frac{\text{cm}^3}{\text{s}}, \quad (4.4)$$

where the efficiency factor f_{eff} parametrizes the absorption efficiency of injected energy in the intergalactic medium.¹⁷ The thermal average in the CMB bound should be evaluated using the dark matter velocity distribution at recombination.

More generally, indirect detection constraints are particularly stringent in scenarios featuring sizable late-time annihilation cross-sections [198–200], especially in the presence of Sommerfeld enhancement [201–203] and bound-state formation effects [204, 205], which can substantially enhance the annihilation rate at low velocities. We therefore focus on indirect detection constraints, while leaving aside direct detection searches. The latter are strongly

¹⁶A simple estimate can also be obtained from the usual freeze-out condition $n_X^{\text{eq}} \langle \sigma_{\text{ann}} v_{\text{rel}} \rangle \simeq H$, where the Hubble rate in the radiation dominated era is given by eq. (2.11).

¹⁷We adopt the conservative estimate $f_{\text{eff}} = 0.137$ for all annihilation channels, following [197].

suppressed by the tiny portal couplings allowed in the mediator mass range relevant for our analysis. Collider constraints are effectively encoded in the allowed range of scalar mixing angles (2.7).

The bound on the annihilation cross-section (4.4) is especially severe for the symmetric dark matter scenario, which is the standard assumption for thermal dark sectors. In this case, particles and antiparticles remain equally abundant after freeze-out, and their late-time annihilations in dense astrophysical environments provide the basis for indirect detection searches. Alternatively, asymmetric dark matter scenarios have attracted considerable interest due to their possible connection with the matter-antimatter asymmetry of the visible sector [206–208]. In such scenarios, the dark sector may also contain a particle-antiparticle asymmetry, resulting in different relic abundances for dark matter particles and antiparticles. Consequently, the late-time annihilation rate is suppressed by the factor [208]

$$\langle \sigma_{\text{ann}} v_{\text{rel}} \rangle \rightarrow \langle \sigma_{\text{ann}} v_{\text{rel}} \rangle \frac{4r_\infty}{(1+r_\infty)^2}. \quad (4.5)$$

Here, r_∞ denotes the ratio between the antiparticle and particle abundances at times well after chemical freeze-out. See sec. 4.2 for more details.

In the following, we discuss the symmetric dark matter scenario in sec. 4.1 and the asymmetric scenario in sec. 4.2, thereby extending the analysis of [54] in the context of dark-sector phase transitions in a PTA-favored GW parameter space.

4.1. Symmetric dark matter scenario

In the standard symmetric freeze-out scenario, the dark matter abundance is determined by solving the Boltzmann equation [209]

$$(\partial_t + 3H)n = -\frac{1}{2} \langle \sigma_{\text{eff}} v_{\text{rel}} \rangle (n^2 - n_{\text{eq}}^2), \quad (4.6)$$

where n denotes the total number density of particles and antiparticles. The quantity $\langle \sigma_{\text{eff}} v_{\text{rel}} \rangle$ is the thermally averaged effective annihilation cross-section, which incorporates non-perturbative effects relevant in the non-relativistic regime.

One such non-perturbative effect arises from the repeated exchange of soft vector mediators between the annihilating particle-antiparticle pair. Such interactions distort the two-body wave function and, for an attractive potential, enhance the annihilation cross-section. This phenomenon is known as Sommerfeld enhancement [88, 210]. In the Coulombic regime, corresponding to the symmetric phase where $m_V = 0$, the Sommerfeld factor admits an analytic expression (see e.g. [211, 212])

$$S_{\text{ann}}(\zeta) = \frac{2\pi\zeta}{1 - e^{-2\pi\zeta}}, \quad \zeta \equiv \frac{\alpha_d}{v_{\text{rel}}}, \quad (4.7)$$

and multiplies the perturbative annihilation cross-section. Here, $\alpha_d = g_d^2/(4\pi)$ is the dark fine-structure constant and v_{rel} is the relative velocity of the annihilating pair.

After the phase transition, the vector mediator acquires a finite mass and the interaction becomes Yukawa-like. In this case, no exact analytic expression for the Sommerfeld factor is available, although approximate analytic results can be obtained using the Hulthén potential [212]. The Sommerfeld factor must therefore be computed numerically and depends on two parameters, $S_{\text{ann}}(\zeta, \xi)$, where

$$\xi = \frac{m_X \alpha_d}{2m_V}. \quad (4.8)$$

This parameter corresponds to the ratio between the would-be Coulombic Bohr radius and the mediator Compton wavelength, and therefore quantifies the screening effects induced by the finite mediator mass. The Coulomb limit is recovered for $\xi \gg 1$.

A second non-perturbative effect originates from the formation of metastable particle-antiparticle bound states. Whenever bound states are efficiently formed and not immediately dissociated by the thermal bath, they provide an additional channel for dark matter depletion into light degrees of freedom, as originally pointed out in [86, 213]. In this case, the relevant quantities are the bound-state formation cross-section, $\sigma_{\text{bsf}} v_{\text{rel}}$, the bound-state dissociation rate, Γ_{bsd} , and the bound-state annihilation width, Γ_{ann} .

For the model (2.1), the LO bound-state formation process proceeds through radiative emission of a dark vector boson [213, 214]. This process can occur both before and after the phase transition. In the broken phase, however, kinematics requires that the energy difference between the incoming scattering state and the bound state exceeds the dark photon mass. As in the case of Sommerfeld enhancement, analytical expressions for bound-state formation, dissociation, and bound-to-bound transitions are available only in the Coulombic limit (cf. e.g. [213, 215]), while numerical computations are required once the mediator mass becomes non-zero (cf. e.g. [214]).

At NLO, several additional processes contribute to bound-state formation and dissociation [216–219]. However, these corrections significantly affect the dark matter relic abundance only for comparatively large values of the coupling. Since the observed relic density in the mass range $m_X \in [10, 100]$ GeV is reproduced for relatively small couplings in our setup, we neglect these higher-order contributions.¹⁸

Neglecting transitions among different bound states, the Boltzmann equation can be expressed solely in terms of the density of scattering states through the effective cross-section [220]

$$\langle \sigma_{\text{eff}} v_{\text{rel}} \rangle = \langle \sigma_{\text{ann}} v_{\text{rel}} \rangle + \sum_n \langle \sigma_{\text{bsf}}^n v_{\text{rel}} \rangle \frac{\Gamma_{\text{ann}}^n}{\Gamma_{\text{ann}}^n + \Gamma_{\text{bsd}}^n}. \quad (4.9)$$

¹⁸Explicit NLO computations available in the literature are typically derived for additional light fermionic species coupled to the dark vector, rather than for light scalars as in the present model.

The first contribution corresponds to direct annihilation from scattering states, while the second accounts for the formation of unstable bound states that subsequently decay. The annihilation cross-section $\sigma_{\text{ann}}v_{\text{rel}}$ is obtained by multiplying the perturbative cross-section by the Sommerfeld factor.

Since annihilation in the present model is dominated by the s -wave contribution, we keep only the corresponding Sommerfeld enhancement factor. In the symmetric phase, the non-relativistic annihilation cross-section, corresponding to the processes (4.2), reads¹⁹

$$\sigma_{\text{ann}}^{\text{sym}}v_{\text{rel}} = \frac{5\pi\alpha_d^2}{4m_X^2} + \mathcal{O}(v_{\text{rel}}^2). \quad (4.10)$$

We refer to the appendix D for details on the cross-section calculations.

Including near-threshold effects, we determine the pairs (m_X, α_d) , or equivalently the coupling g_d , for which the observed dark matter relic abundance, $\Omega_{\text{DM}}h^2|_{\text{obs.}} = 0.1200 \pm 0.0012$, is reproduced [6]. The Boltzmann equation is solved numerically for the yield $Y_X = n_X/s$, where s denotes the total entropy density of the visible and dark sectors.²⁰

After including Sommerfeld enhancement and bound-state formation effects, we find that the corrections to the perturbative freeze-out prediction remain modest, at the level of approximately 4%. This can be traced back to the relatively small couplings required to reproduce the observed relic density in the mass range $m_X \in [10, 10^2]$ GeV, corresponding to $g_d \in [0.06, 0.2]$.

Notably, the gauge couplings required to realize a strong first-order phase transition in the scanned parameter space of tab. 2 are significantly larger than those compatible with the observed relic abundance via thermal freeze-out. As a consequence, for couplings relevant to the phase-transition dynamics, the dark matter relic density is generically several orders of magnitude below the observed value.

We now turn to late-time annihilations and consider the leading velocity-independent contribution to the annihilation cross-section in the broken phase of the dark sector, denoted by $\sigma_{\text{ann}}^{\text{bro}}v_{\text{rel}}$. The explicit expression is reported in appendix D. The main qualitative difference with respect to the symmetric phase is that the Sommerfeld factor now depends on the finite mediator mass through eq. (4.8). In addition, bound-state formation proceeds via the

¹⁹The non-relativistic annihilation cross-section receives two leading contributions, namely $X\bar{X} \rightarrow VV$ and $X\bar{X} \rightarrow SS^*$. The former yields the well-known result at LO in the relative velocity, $\sigma_{\text{ann}}^{\text{sym}}v_{\text{rel}}(X\bar{X} \rightarrow VV) = \pi\alpha_d^2/m_X^2$ (cf. e.g. [221]), while the latter gives $\sigma_{\text{ann}}^{\text{sym}}v_{\text{rel}}(X\bar{X} \rightarrow SS^*) = \pi\alpha_d^2/(4m_X^2)$. Our result differs from the expression reported in [54].

²⁰Strictly speaking, the Boltzmann equation should be integrated down to temperatures well below the chemical freeze-out temperature. For the standard variable $z = m_X/T$, matching the precision of the experimental uncertainty on the relic abundance typically requires $z \gtrsim 10^4$. We explicitly checked that switching to the broken-phase annihilation cross-section at low temperatures has negligible impact on the predicted relic abundance. Consequently, $\Omega_{\text{DM}}h^2$ is effectively independent of the scalar and vector masses, or equivalently of the quartic coupling λ_s .

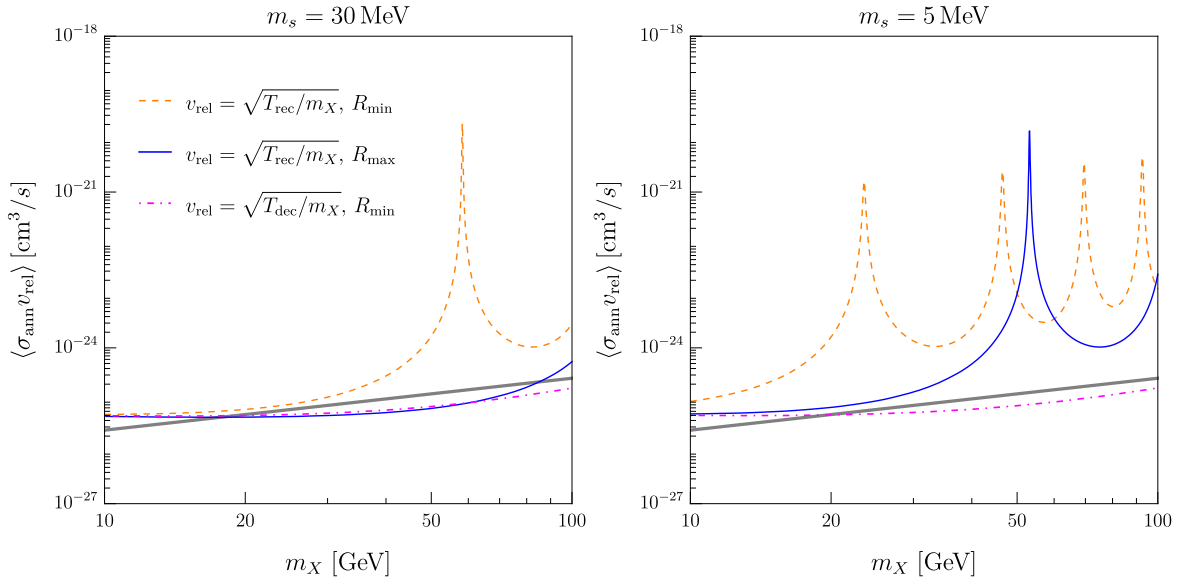


Figure 4: Thermally averaged annihilation cross-section for two benchmark choices of the dark scalar mass, $m_s = 30 \text{ MeV}$ (left) and $m_s = 5 \text{ MeV}$ (right), same legend holds for both panels. The solid gray line denotes exclusion limit as given in eq. (4.4). Dashed orange and blue curves show the annihilation cross-section at relative velocities characteristic of the recombination epoch. The magenta dot-dashed curve corresponds to larger relative velocities expected for an earlier kinetic decoupling at $T \sim \mathcal{O}(1) \text{ MeV}$.

emission of a massive dark vector boson.

The comparison between the predicted annihilation cross-section and the *Planck* exclusion bound is shown in fig. 4 for two benchmark values of the dark scalar mass, namely $m_s = 30 \text{ MeV}$ and $m_s = 5 \text{ MeV}$. One clearly observes the resonant structure characteristic of Sommerfeld enhancement in a Yukawa potential. We further verified that the contribution from bound-state formation remains subleading throughout the parameter space of interest. This is due both to the smallness of the relevant couplings and to the phase-space suppression associated with the emission of a massive mediator in the final state.

Overall, a substantial portion of the dark matter mass range considered in this work is strongly constrained. We analyze two benchmark configurations for the ratio between the vector mediator and dark matter masses, $R \equiv \frac{m_V}{m_X}$, namely R_{min} corresponding to $m_V = 2m_s$, and R_{max} corresponding to $m_V = 10m_s$. If one assumes that dark matter particles remain in kinetic equilibrium with the thermal bath until recombination, their typical relative velocity can be estimated as $v_{\text{rel}} \approx \sqrt{T_{\text{rec}}/m_X}$. For the mass range $m_X \in [10, 10^2] \text{ GeV}$ and using $T_{\text{rec}} \simeq 1 \text{ eV}$, one obtains relative velocities in the range $v_{\text{rel}} \sim 10^{-6} - 10^{-5}$.

In practice, kinetic decoupling is expected to occur well before recombination. Since the

massive dark vector and scalar particles must decay before BBN, the scattering processes responsible for maintaining kinetic equilibrium between dark matter and the thermal bath are expected to become inefficient already at temperatures of $\mathcal{O}(1)$ MeV (see sec. 2.2). This occurs well before recombination and therefore implies larger relative velocities, $v_{\text{rel}} \approx 10^{-3}$. The resulting enhancement is substantially reduced, and the magenta dot-dashed curves shown in fig. 4 consequently lie much closer to, and in some regions slightly below, the current experimental exclusion limits.

4.2. Asymmetric dark matter scenario

A primordial asymmetry may be generated in the dark sector, in analogy with the baryon asymmetry of the visible sector. In the latter case, observations indicate $\eta_{\text{B}} = (0.88 \pm 0.021) \times 10^{-10}$, as inferred from CMB measurements [6]. We do not attempt to address the microscopic origin of the dark-sector asymmetry (see e.g. reviews of the subject [222, 223]). Instead, we assume that such an asymmetry is generated before chemical decoupling and is therefore already present during the freeze-out epoch. In the following, we adopt the notation and formalism of [208, 224].

We define the asymmetry parameter through the difference between the particle and antiparticle yields,

$$Y_X - Y_{\bar{X}} = \eta_{\text{DS}}, \quad Y_X = \frac{n_X}{s}, \quad Y_{\bar{X}} = \frac{n_{\bar{X}}}{s}, \quad r_\infty = \frac{Y_{\bar{X}}(z_{\text{fin}})}{Y_X(z_{\text{fin}})}, \quad (4.11)$$

where $\eta_{\text{DS}} = \epsilon \eta_{\text{B}}$ denotes the conserved dark-sector asymmetry, normalized to the observed baryon asymmetry. Without loss of generality, we assume $\eta_{\text{DS}} > 0$, corresponding to an excess of dark matter particles over antiparticles. The present-day dark matter abundance is then determined by the combined contribution of both components. The ratio r_∞ parametrizes the residual antiparticle fraction at late times.²¹

In contrast to the symmetric freeze-out scenario, the equilibrium number densities involve a non-vanishing chemical potential. In the non-relativistic regime, the equilibrium density of particles is approximately given by

$$n_X^{\text{eq}}(\mu_X) \simeq n_X^{\text{eq}} e^{\mu_X/T}, \quad n_X^{\text{eq}} = g_X \left(\frac{m_X T}{2\pi} \right)^{3/2} e^{-m_X/T}, \quad (4.12)$$

where n_X^{eq} corresponds to the equilibrium density in the symmetric limit and μ_X is the chemical potential of the dark fermion. The corresponding expression for antiparticles is obtained by reversing the sign of the chemical potential.²²

²¹The Boltzmann equations (4.15) and (4.16), are solved up to $z_{\text{fin}} = 10^5$.

²²In the limit of vanishing asymmetry, particle and antiparticle equilibrium densities coincide *viz.* $n_X^{\text{eq}} = n_{\bar{X}}^{\text{eq}}$.

By introducing the equilibrium yield in the symmetric case,

$$Y^{\text{eq}} \equiv n_X^{\text{eq}}/s, \quad (4.13)$$

one obtains the following relation for the chemical potential

$$e^{\mu_X/T} = \frac{1}{2} \left(\frac{\eta_{\text{DS}}}{Y_{\text{eq}}} + \sqrt{4 + \frac{\eta_{\text{DS}}^2}{Y_{\text{eq}}^2}} \right). \quad (4.14)$$

The Boltzmann equations for the particle and antiparticle yields can then be written as

$$\frac{dY_X}{dz} = -\frac{s\xi(T)}{zH} \langle \sigma_{\text{eff}} v_{\text{rel}} \rangle (Y_X^2 - \eta_{\text{DS}} Y_X - Y_{\text{eq}}^2), \quad (4.15)$$

$$\frac{dY_{\bar{X}}}{dz} = -\frac{s\xi(T)}{zH} \langle \sigma_{\text{eff}} v_{\text{rel}} \rangle (Y_{\bar{X}}^2 - \eta_{\text{DS}} Y_{\bar{X}} - Y_{\text{eq}}^2), \quad (4.16)$$

where

$$\xi(T) \equiv \left(1 + \frac{d \ln h_{\text{eff}}(T)}{3d \ln T} \right), \quad (4.17)$$

accounts for the temperature dependence of the entropic degrees of freedom. The effective annihilation cross-section $\langle \sigma_{\text{eff}} v_{\text{rel}} \rangle$ is the same quantity as in eq. (4.9) and includes Sommerfeld enhancement and bound-state formation effects.

The present-day dark matter abundance is finally expressed as

$$\Omega_{\text{DM}} h^2 = 0.2743 \times 10^9 Y_X(z_{\text{fin}}) (1 + r_\infty) \frac{m_X}{\text{GeV}}, \quad (4.18)$$

using the last relation in (4.11), together with the present-day entropy density and critical density.

Our results are consistent with the general picture established in previous studies of asymmetric dark matter [208, 224]. The relic abundance of particles is predominantly determined by the primordial asymmetry η_{DS} and is therefore largely insensitive to the annihilation cross-section. In contrast, the antiparticle abundance is strongly controlled by the annihilation efficiency and can be substantially depleted depending on the values of the coupling g_d and the asymmetry parameter η_{DS} . As expected, larger couplings lead to a stronger suppression of the antiparticle component and therefore to smaller values of r_∞ .

In fig. 5 (left), we show the particle-antiparticle ratio r_∞ in the (ϵ, α_d) plane, together with contours of the gauge coupling g_d for ease of comparison with the phase transition analysis. One observes that sizable antiparticle fractions are realized only for sufficiently small couplings, while r_∞ rapidly decreases to the per-mille level as α_d increases. Consequently, Sommerfeld enhancement and bound-state effects become relevant only in the regime where the antiparticle abundance is already strongly suppressed, implying that their impact on the relic density remains moderate.

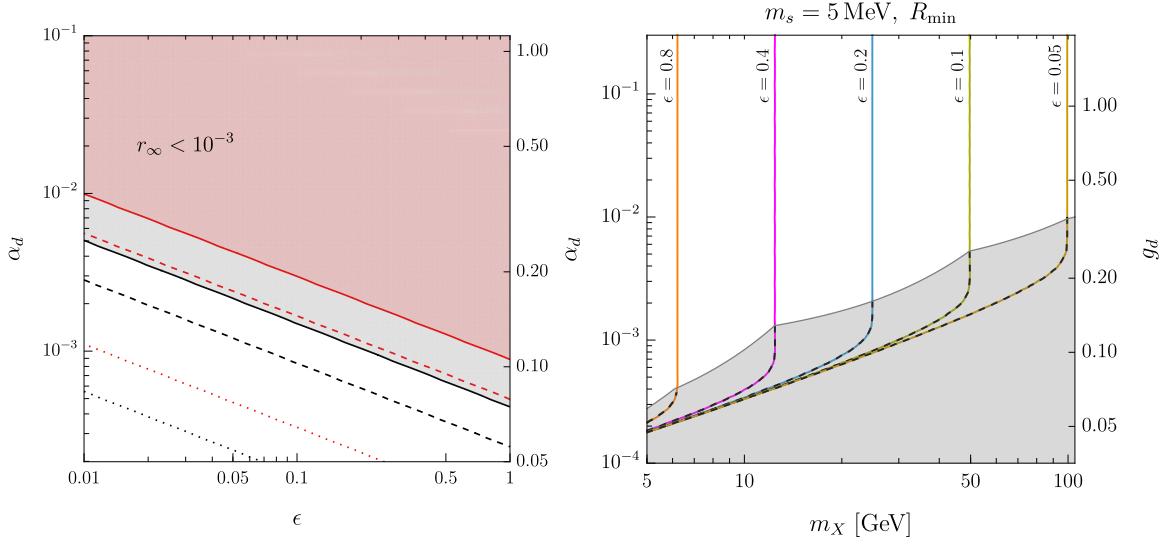


Figure 5: Left: Contour lines of the residual antiparticle fraction r_∞ in the (ϵ, α_d) plane for $m_X = 10$ GeV (black) and $m_X = 50$ GeV (red). Dotted, dashed, and solid lines denote $r_\infty = 0.9, 0.1$, and 10^{-3} , respectively. Right: Contour lines reproducing the observed dark matter relic abundance for different values of the dark-sector asymmetry $\eta_{\text{DS}} = \epsilon \eta_{\text{B}}$. Black dotted segments and the gray shaded region indicate the parameter space excluded by *Planck* limits on late-time dark matter annihilations.

We present results for two benchmark dark matter masses, namely $m_X = 10$ GeV and $m_X = 50$ GeV, shown respectively by the black and red curves. Their behavior can be understood from the scaling of the annihilation cross-section, $\sigma_{\text{eff}} v_{\text{rel}} \propto \alpha_d^2 / m_X^2$. Larger dark matter masses therefore require larger values of the coupling to achieve the same level of antiparticle depletion.

Finally, we turn to the region of parameter space consistent with the observed dark matter relic abundance. In fig. 5 (right), we show representative curves in the (m_X, α_d) plane for different values of the asymmetry parameter ϵ . These curves indicate the combinations of the dark matter mass and coupling for which the observed relic abundance, $\Omega_{\text{DM}} h^2|_{\text{obs.}}$, is reproduced. At small values of α_d , the coupling exhibits a non-trivial dependence on the dark matter mass. As discussed above, this regime corresponds to sizable residual antiparticle fractions, such that the relic abundance becomes sensitive to the annihilation cross-section. This effect becomes increasingly pronounced for smaller asymmetries. Indeed, decreasing ϵ reduces the particle contribution to the relic density, since $Y_X \propto \epsilon \eta_{\text{B}}$, and therefore requires a larger antiparticle component.

In the same fig. 5 (right), we also superimpose the regions excluded by late-time annihilations at recombination, cf. eq. (4.4). The excluded regions correspond predominantly to large values of r_∞ , which are realized for sufficiently small couplings. In this regime, the

| | g_d | m_s [MeV] | λ_s | $\sin \theta_s$ |
|-------|-------------|------------------|---------------------------------|--|
| Range | [0.25, 1.5] | [$10^0, 10^2$] | [$10^{-4}, 3 \times 10^{-1}$] | [$2 \times 10^{-5}, 2 \times 10^{-4}$] |
| Prior | linear | logarithmic | logarithmic | logarithmic |

Table 2: Parameter space scan ranges in the Abelian Higgs model (2.1), focused on a first-order phase transition at the MeV scale based on the constraints (2.7). Priors are chosen to be either linear or logarithmic in the indicated range. The parameters are input at the scale of the corresponding dark photon mass $\bar{\mu}_0 = m_\nu$ and run to the thermal scale $\bar{\mu}_{\text{ref}} = \pi T$ (5.1).

antiparticle abundance remains sizable and enhances the annihilation signal probed by CMB observations. For the comparison with late-time annihilation constraints, we also include Sommerfeld enhancement and bound-state formation effects. We find that these corrections remain relatively mild and become appreciable only for couplings $\alpha_d \gtrsim 10^{-3}$.

The accumulation of viable solutions around $m_\chi \sim 5$ GeV can be readily understood from the observed relation between the dark matter and baryonic energy densities. Since the dark matter abundance is approximately five times larger than the baryonic one, and the visible matter density is dominated by baryons with masses of $\mathcal{O}(1)$ GeV, asymmetric dark matter scenarios naturally favour dark matter masses in the few-GeV range.

Overall, and in contrast to the symmetric scenario discussed in sec. 4.1, we find sizable regions of parameter space that remain phenomenologically viable, especially for larger g_d . This feature is particularly appealing in light of the phase transition analysis, where stronger couplings are generally associated with a more sizable GW signal.

5. Reconciling first-order phase transitions with PTA data

We focus on the dark-sector Abelian Higgs model (2.1), as a representative for the model class of radiatively generated cubic potentials (3.8). Using its thermal EFT introduced in sec. 3, we assess whether the region of parameter space that gives rise to a theoretically controlled first-order phase transition is compatible with the SGWB favored by the recent PTA data [17, 19, 20, 22, 23]. After establishing the range over which the employed EFTs provide a controlled description of the phase transition, we compare the resulting GW predictions with the PTA-preferred parameter space. To this end, we employ the soft EFT1 and the softer EFT2 at the accuracy level outlined in sec. 3 which we will refer to as NLO.

The parameter space scan is performed over the model parameters of the fundamental Lagrangian (2.1), spanned by the dark gauge coupling g_d , the dark scalar quartic coupling λ_s , and the dark scalar mass m_s , whose ranges and corresponding prior distributions are informed by the constraints (2.7) and summarized in tab. 2. The dark fermion mass is fixed to $m_\chi \sim \mathcal{O}(10\text{--}10^2)$ GeV, and therefore is Boltzmann suppressed at the MeV scale of the

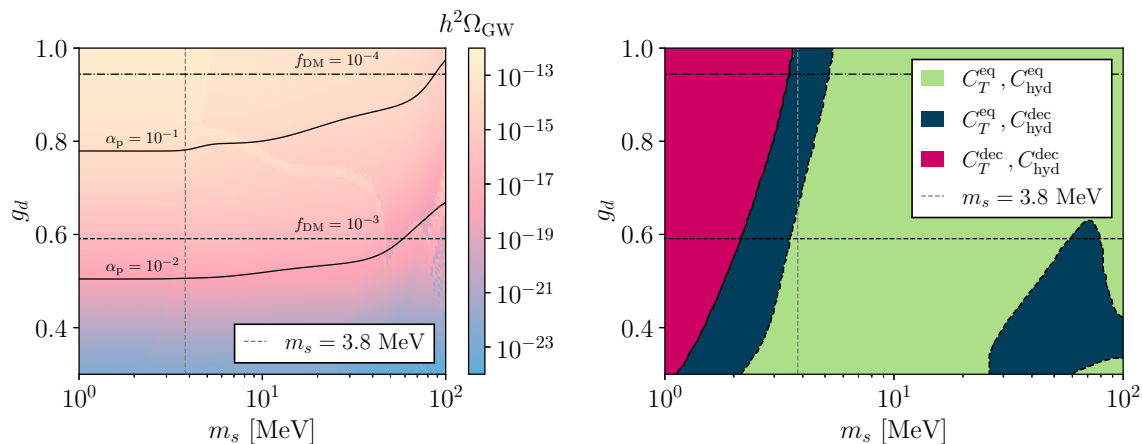


Figure 6: Left: Gravitational-wave amplitude for a first-order phase transition in the Abelian Higgs model (2.1), computed in the soft (EFT1) in the (g_d, m_s) plane. The dark scalar quartic coupling is fixed to $\lambda_s = 10^{-2}$ and $\sin\theta_s = 2 \times 10^{-4}$. The vertical dashed line at $m_s = 3.8$ MeV is the lower bound from [103]. Black dashed and dot-dashed lines indicate (g_d, m_s) values for which symmetric freeze-out yields a fraction $f_{\text{DM}} \equiv \Omega_X/\Omega_{\text{DM}}^{\text{obs}}$ of the observed dark matter abundance, $\Omega_{\text{DM}}^{\text{obs}} h^2 = 0.1200(12)$ [6]. The strongest transitions occur at the largest g_d and smallest m_s . Towards the upper right corner, $v_w^{\text{LTE}} = 1$, as indicated by a faint discontinuous jump in Ω_{GW} . Right: Thermal equilibrium condition C_T^{eq} (2.10) and hydrodynamic equilibrium condition $C_{\text{hyd}}^{\text{eq}}$ (3.47) in the same (g_d, m_s) plane. Magenta regions satisfy neither C_T^{eq} nor $C_{\text{hyd}}^{\text{eq}}$, blue regions satisfy only $C_{\text{hyd}}^{\text{eq}}$, and green regions satisfy both C_T^{eq} and $C_{\text{hyd}}^{\text{eq}}$.

phase transition. The parameters are input at the scale of the corresponding dark photon mass $\bar{\mu}_0 = m_V$ and run to the reference scale

$$\bar{\mu}_{\text{ref}} = A\pi T, \quad \text{with } A \in [2^{-1}, 2^1], \quad (5.1)$$

which aligns with the lowest Matsubara mode. Later, we explore the impact of varying the reference scale by a factor of two in either direction. In most of the scans we take the central value $A = 1$. We also relate physical parameters to Lagrangian parameters at one-loop level in vacuum renormalization, as detailed in appendix B.2 and e.g. [62, 225].

We first focus on a sub-set of the parameter space scan for fixed $\lambda_s = 10^{-2}$, $\sin\theta_s = 2 \times 10^{-4}$, up to $g_d = 1.0$ and compute corresponding the GW amplitude $\Omega_{\text{GW}} h^2$ in the single broken power-law template of eq. (SBPL) in both the soft EFT1 in fig. 6 and the softer EFT2 in fig. 7. Both EFTs possess only a finite range of validity in their respective EFT expansion parameter x [73] defined in eq. (3.8). For EFT2 this range is very narrow, and the breakdown of its validity is indicated by the gray shaded region in fig. 7. The breakdown also manifests

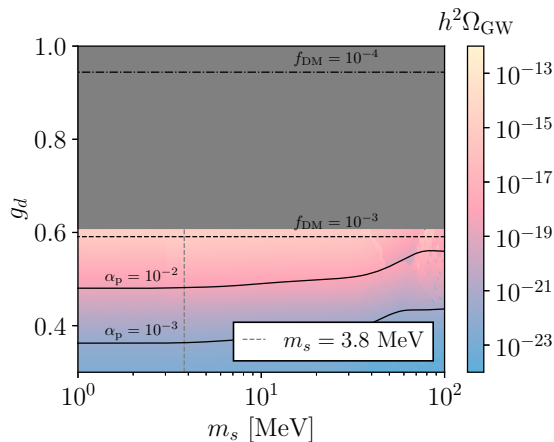


Figure 7: Gravitational-wave amplitude for a first-order phase transition in the Abelian Higgs model (2.1), computed in the softer (EFT2) in the (g_d, m_s) plane. Scan ranges and constraint lines the same as in fig. 6. Grey shaded regions mark where $x < x_{\min}$ and higher-dimensional operators in the EFT become relevant with $x_{\min} = 0.051g_d^2$ taken for the soft EFT1 [73] which coincides with the onset of unphysical values $c_{s,\text{bro}}^2 < 0$ for the softer EFT2.

itself in the unphysical values $c_{s,\text{bro}}^2 < 0$ as reported in fig. 8 (right). The latter can also be interpreted as a loss of perturbativity, since $p_0 \sim TF_{\text{bro}}$ in this regime. This effect is especially pronounced in our model because the number of relativistic degrees of freedom is small, $g_{\text{eff}} \sim \mathcal{O}(1)$.²³ By contrast, the less restrictive approximation in eq. (EFT1) remains valid over a wider range, so the corresponding gray-shaded region in fig. 6 (left) affects only the large-coupling part beyond the scan. The strongest and slowest transitions are realized for the largest values of g_d and the smallest values of m_s .

We assess whether the dark and visible sectors remain both thermally and hydrodynamically coupled throughout the phase transition, as established through the criteria of eqs. (2.10) and (3.47). Thermal equilibrium determines whether the two sectors share a common temperature $T_{\text{DS}} = T_{\text{SM}}$. Hydrodynamic equilibrium determines whether both sectors are hydrodynamically coupled and hence which relativistic degrees of freedom enter in the hydrodynamic quantities of sec. 3. In fig. 6 (right), neither criterion holds in the magenta region, only hydrodynamic equilibrium in the blue region, and both in the green region. Notably, the strongest PTA-relevant signals arise at large coupling and $m_s \gtrsim 3.8$ MeV [103], precisely the blue region. There the two sectors still share a common temperature, yet the SM plasma becomes hydrodynamically decoupled from the dark sector, so that only the dark-sector degrees

²³For phase transitions occurring at the electroweak scale, the effective number of relativistic degrees of freedom is $g_{\text{eff}} \approx \mathcal{O}(100)$. Consequently, the symmetric pressure p_0 is significantly larger than in the MeV-scale Abelian Higgs model considered here, which enhances the pathological behavior of $c_{s,\text{bro}}^2$.

of freedom g_{DS} enter the hydrodynamic quantities relevant for the GW signal.

The scans shown in figs. 6 and 7 also illustrate the interplay between the phase-transition dynamics and the dark matter phenomenology of the model defined in eq. (2.1). As discussed in the previous sections, we consider dark matter masses in the range $\mathcal{O}(10\text{--}100)$ GeV, well above the MeV scale associated with the phase transition. The black dashed and dot-dashed lines indicate the values of the gauge coupling for which the symmetric freeze-out mechanism reproduces only a small fraction $f_{\text{DM}} \equiv \Omega_X/\Omega_{\text{DM}}^{\text{obs}}$ of the observed dark matter abundance, $\Omega_{\text{DM}}^{\text{obs}}h^2 = 0.1200(12)$ [6]. This is a direct consequence of the relatively large gauge couplings required to generate a strong first-order phase transition, which in turn produce annihilation cross-sections significantly larger than the canonical thermal value, $\langle\sigma v_{\text{rel}}\rangle_{\text{th}} \simeq 3 \times 10^{-26} \text{ cm}^3 \text{ s}^{-1}$ [226], for dark matter masses in the range $\mathcal{O}(10)$ GeV.²⁴ The curves for f_{DM} are essentially independent of the dark scalar mass, because freeze-out occurs at temperatures well above the phase-transition temperature; see (4.10) for the corresponding annihilation cross section. For both lines, the DM mass is set to $m_X = 30$ GeV.

Comparing figs. 6 and 7 with fig. 5 (right) shows that the asymmetric dark matter scenario naturally accommodates the observed relic abundance in the region favored by the phase transition. In particular, for $g_d \gtrsim 0.3$, the model reproduces the observed dark matter density while remaining consistent with current experimental constraints over the range of dark matter masses and asymmetry parameters η_{DS} considered in this work. This illustrates the complementarity between the GW and dark matter phenomenology. The relatively large gauge couplings required to generate a strong first-order phase transition are naturally compatible with asymmetric freeze-out, whereas they severely over-deplete the relic abundance in the conventional symmetric scenario of sec. 4.1.

5.1. Breakdown of high-temperature expansion

In this section, we scrutinize the limitations of the EFT framework of sec. 3 and identify the parameter regimes in which the super-renormalizable EFT1 and EFT2 are invalidated. A fully consistent extension beyond the high-temperature expansion as in e.g. [227] is beyond the scope of this work. However, based on extending the EFT operator basis to dimension-six [73, 135], we delimit the range of validity of the EFTs on top of the parameter space scan of tab. 2 using the criteria of eqs. (EFT1) and (EFT2). These limits were already indicated in fig. 7 by the gray shaded regions and mark the breakdown of the EFT expansion which coincides, to a good extent, with the unphysical values of the broken-phase speed of sound $c_{\text{s, bro}}^2 < 0$ which we display in fig. 8 (right).

²⁴This tension is progressively alleviated for heavier dark matter particles, since larger gauge couplings are then required to reproduce the observed relic abundance. The DM mass range is also motivated by the comparison with earlier studies [54].

For sufficiently strong transitions, the standard EFT of eqs. (3.1) and (3.2) becomes insufficient and higher-dimensional operators have to be included in the

- (i) *Effective potential.* Marginal 3dEFT operators such as ϕ^6 induced by hard modes modify the effective potential and become quantitatively important when the EFT expansion parameter $x = \lambda_{s,3}/\eta^{2/3}$ becomes too small [73, 131].
- (ii) *Nucleation action.* Both hard and soft fluctuations of $\mathcal{O}(\pi T), \mathcal{O}(gT)$ [131], as well as fluctuations around the critical bubble of $\mathcal{O}(\mu_{\text{nucl}})$ contribute to the nucleation action. Here, μ_{nucl} denotes the inverse length scale of the critical bubble. A derivative expansion in these scales, however, is only justified for hard and soft fluctuations [37, 143]. A consistent treatment requires retaining all dimension-six operators, including derivative operators. In the present model, this corresponds to $\mathcal{O}(10)$ independent operators [73, 130] which also modify the fluctuation determinant.

The absence of these operators can compromise the characterization of the phase-transition dynamics directly in certain parameter space regions. Since for (ii) only the computation of the bounce in the presence of higher-dimensional operators is addressed in [131], extending it to fluctuation determinants is beyond the scope of this work. We therefore restrict to the standard super-renormalizable EFT (3.1) and, utilizing the criteria of (EFT1) and (EFT2), indicate the regions of parameter space in which omitting higher-dimensional operators is expected to be most severe.

Since PTA-favored transitions tend to be among the strongest transitions accessible in the model, they also lie close to the validity limits of the high-temperature effective theory. We therefore delineate the theoretical boundaries of our EFT description. When working in the softer EFT2, after integrating out the Debye scale in the symmetric phase, the validity of the EFT can be assessed by two conditions:

- (A) The validity of the *high-temperature expansion*, of having integrated out the Debye scale, can be monitored by the ratio $h_3\phi_3^2/m_D^2 \ll 1$. This ratio controls the hierarchy between the soft and Debye scales. When this ratio becomes of order unity, the integration over Matsubara zero modes can no longer be performed within a strict expansion in temperature scales, and the softer-scale EFT2 ceases to provide a controlled approximation.
- (B) The validity of the *perturbative expansion* can be monitored by the ratio $h_3/(4\pi m_D) \sim g_d \ll 1$ [72, 73, 137, 228], which controls the corrections to the effective expansion parameter within $\bar{\lambda}_{s,3}$ as discussed in eq. (C.12) and below.

Breaking condition (A) signals the onset of higher-dimensional operators in the softer EFT2, as already observed in fig. 7. The regime where the high-temperature expansion breaks down

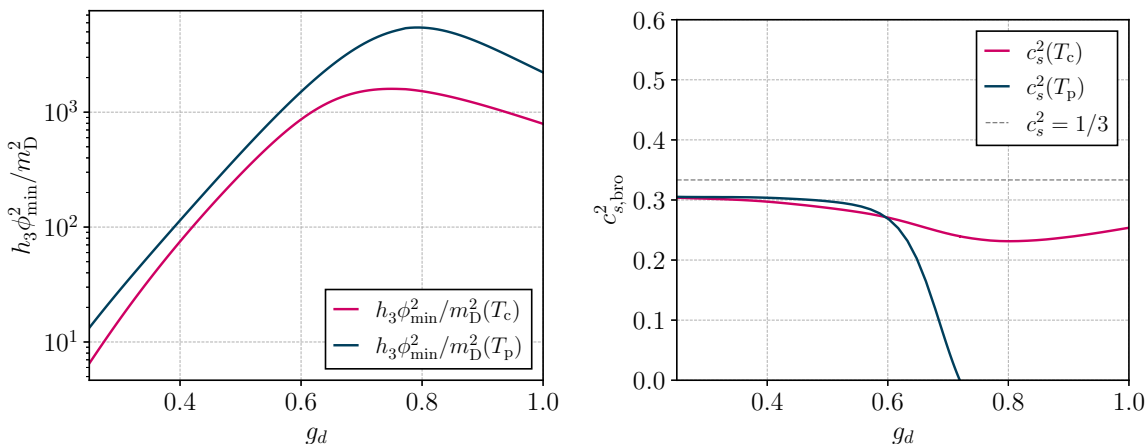


Figure 8: Tests of the validity of the high-temperature and perturbative expansions at benchmark point BM7 of tab. 3 and varying $g_d \in [0.25, 1.0]$. Left: Ratio $h_3 \phi_{\min}^2 / m_D^2$ across the parameter scan, indicating the breakdown of the high-temperature expansion when $h_3 \phi_{\min}^2 / m_D^2 \gg \mathcal{O}(1)$. Right: Broken-phase speed of sound $c_{s,\text{bro}}^2$ across the same scan using the softer EFT2, indicating the onset of non-perturbative behavior when $c_{s,\text{bro}}^2 \ll 1/3$.

coincides with small x (gray region), which is precisely where higher-dimensional operators become quantitatively important. In fig. 8 (left), we show the ratio $h_3 \phi_{\min}^2 / m_D^2$,²⁵ across a parameter scan in g_d for fixed $\lambda_s = 10^{-2}$ and $\sin \theta_s = 2 \times 10^{-4}$. For larger values of g_d , the ratio approaches $\mathcal{O}(10^3)$, strongly invalidating the assumption that one can integrate out the Debye scale m_D .

This motivates utilizing the soft-scale EFT1, whose validity range extends to somewhat smaller x than the softer broken-phase setup. However, statements such as “in the limit of strongest transition” refer to parameter points where even this soft EFT saturates its validity range. The validity bracket $0.051 g_d^2 \ll x \ll 0.18$ is in practice saturated near its lower end for the parameter points relevant to PTA phenomenology. A more quantitative inclusion of dimension-six operators in the nucleation action and fluctuation determinant remains the natural next step for this class of analyses, and we leave it to future work. Frameworks that simultaneously incorporate thermal resummation and remain valid over a broad temperature range are currently being developed. See e.g. [134, 227] for promising approaches to go beyond the high-temperature expansion.

Breaking condition (B) signals a violation of perturbativity in the fundamental theory. It

²⁵For nucleation, the relevant field value is the escape point ϕ_{esc} , which is slightly larger than ϕ_{\min} . However, the difference is negligible for the present discussion since supercooling is small in the parameter space of interest. For stronger supercooling, however, the escape point can become hierarchically separated, $\phi_{\text{esc}} \ll \phi_{\min}$, which can render the high-temperature expansion valid again [36].

can manifest as a breakdown of the perturbative series of x itself or of derived quantities, such as $c_{s,\text{bro}}^2$ becoming unphysical, as we show in fig. 8 (right). This breakdown is present regardless of whether the high-temperature expansion is valid, as can be seen from the large deviation of $c_{s,\text{bro}}^2$ from $1/3$ at both T_p and T_c , with the largest deviation at T_p . Therefore, a violation of perturbativity can become relevant for the PTA-favored region already for values of $g_d \gtrsim \mathcal{O}(0.5)$. As mentioned earlier, this unphysical behavior of the speed of sound is most pronounced in phase transitions with a small number of relativistic degrees of freedom, like the ones addressed in this work and relevant for PTA. For a larger number of relativistic degrees of freedom, the breakdown of perturbativity is delayed to larger values of g_d .

5.2. Implications for the PTA-favored region

While the softer **EFT2** setup has the largest range of validity across the relevant range of couplings, we employ both the soft and softer EFTs to assess the compatibility of the Abelian Higgs model with the PTA-favored region. To this end, we employ the **PTArcade** [229] implementation of the **ceffy1** likelihood [230] for the NANOGrav 15 yr data set [17], considering the first 14 Fourier frequencies in the range $f \in [2, 28]$ nHz as recommended by the NANOGrav collaboration [30].

Going beyond the parameter-space scan in figs. 6 and 7, we report a set of benchmark (BM) points in tab. 3 at fixed $\sin \theta_s = 2 \times 10^{-4}$. These points allow for a direct comparison with the PTA signal at nHz frequencies and illustrate, directly in frequency space in fig. 9, the predicted GW signal and its *incompatibility* with the PTA-favored region. Here, we employ the double broken power law template of eq. (DBPL) and display the corresponding spectra for BM1–BM7 in fig. 9 (left) and BM8–BM16 in fig. 9 (right). The latter are taken from earlier studies, BM8–BM11 from [54], BM12 from [56], and BM13–BM16 from [58]. Additionally, in fig. 9 (right), we show the dependence of the predicted GW signal on the 4d renormalization scale $\bar{\mu}$ for BM13 of tab. 3. The band indicates the residual scale dependence obtained by varying the reference scale as in eq. (5.1). This scale dependence estimates the theoretical uncertainty from missing higher-order perturbative corrections [158], corresponding to a variation $\Delta\Omega_{\text{GW}}/\Omega_{\text{GW}} \sim \mathcal{O}(10)$. This is typical at NLO and remains much smaller than the theoretical uncertainty of LO predictions [68, 137, 158, 231]. Benchmarks BM9–BM12 are not in thermal equilibrium with the SM plasma, failing the condition (2.10). The number of effective hydrodynamically relevant degrees of freedom is adapted according to condition (3.47). In all cases, the predicted signal is incompatible with the PTA-favored region.

Finally, we perform a randomized scan [232] over the model parameter ranges and priors in tab. 2 to determine the full distribution of the thermodynamic quantities $(\alpha_\star, \beta/H_\star)$ and compare the generic GW template of eq. (DBPL) with the PTA data. The resulting values of α_\star and β/H_\star are shown in fig. 10, together with the 1σ (solid) and 2σ (dashed) density contours of the scan for the soft **EFT1** (left, magenta) and the softer **EFT2** (right, dark blue).

| BM | m_s [MeV] | g_d | λ_s | T_c [MeV] | T_p [MeV] | $c_{s,\text{bro}}^2$ | v_w^{LTE} | $\alpha_{\star,\text{hyd}}$ | β/H_\star | C_T^{eq} | $C_{\text{hyd}}^{\text{eq}}$ |
|------|-------------|-------|-------------|-------------|-------------|----------------------|--------------------|-----------------------------|-----------------|-------------------|------------------------------|
| BM1 | 5.00 | 0.5 | 0.05 | 12.64 | 12.39 | 0.320 | 0.578 | 0.0014 | 1759 | ✓ | ✓ |
| BM2 | 5.00 | 0.5 | 0.005 | 15.58 | 14.19 | 0.307 | 0.613 | 0.0256 | 4221 | ✓ | ✓ |
| BM3 | 5.00 | 0.7 | 0.05 | 9.91 | 9.50 | 0.317 | 0.586 | 0.0093 | 4769 | ✓ | ✓ |
| BM4 | 5.00 | 0.7 | 0.01 | 11.97 | 10.31 | 0.315 | 0.668 | 0.0556 | 2706 | ✓ | ✓ |
| BM5 | 5.00 | 0.7 | 0.0075 | 12.44 | 10.08 | 0.315 | 0.721 | 0.0841 | 1816 | ✓ | ✓ |
| BM6 | 5.00 | 0.8 | 0.05 | 9.11 | 8.56 | 0.316 | 0.600 | 0.0187 | 5063 | ✓ | ✓ |
| BM7 | 5.00 | 0.8 | 0.01 | 11.37 | 8.97 | 0.317 | 0.751 | 0.1029 | 1625 | ✓ | ✓ |
| BM8 | 4.40 | 0.960 | 0.0190 | 8.62 | 6.88 | 0.289 | 0.698 | 0.3894 | 2184 | ✓ | ✗ |
| BM9 | 4.01 | 0.986 | 0.0199 | 7.75 | 6.13 | 0.294 | 0.712 | 0.4061 | 2148 | ✗ | ✗ |
| BM10 | 4.10 | 0.921 | 0.0146 | 8.45 | 6.60 | 0.279 | 0.713 | 0.4437 | 1777 | ✗ | ✗ |
| BM11 | 4.51 | 0.990 | 0.0200 | 8.71 | 6.87 | 0.294 | 0.714 | 0.4093 | 2138 | ✗ | ✗ |
| BM12 | 3.39 | 1.2 | 0.03 | 5.94 | 4.38 | 0.349 | 0.817 | 0.5010 | 1801 | ✗ | ✗ |
| BM13 | 55.0 | 0.75 | 0.006 | 136.91 | 98.99 | 0.219 | 0.840 | 0.7551 | 1102 | ✓ | ✗ |
| BM14 | 110 | 0.75 | 0.006 | 273.83 | 197.99 | 0.170 | 1.000 | 0.8932 | 1102 | ✓ | ✗ |
| BM15 | 329 | 0.75 | 0.006 | 818.99 | 592.16 | 0.254 | 1.000 | 0.0359 | 1102 | ✓ | ✓ |
| BM16 | 141 | 0.85 | 0.01 | 313.78 | 238.21 | 0.251 | 0.750 | 0.5463 | 1362 | ✓ | ✗ |

Table 3: Benchmark (BM) points in the parameter space of the Abelian Higgs model (2.1) that yield a first-order phase transition at the MeV scale in the soft EFT1. BM8–BM11 are taken from [54], BM12 is from [56], and BM13–BM16 are from [58]. The input parameters are the dark scalar mass m_s , the dark gauge coupling g_d , and the dark scalar quartic coupling λ_s , specified at the input scale $\bar{\mu}_0 = m_\nu$. The portal coupling $\sin\theta_s = 10^{-4}$ and $\epsilon_s < 1$. The remaining columns list the critical temperature T_c , the percolation temperature T_p , the broken-phase sound speed $c_{s,\text{bro}}^2(T_\star)$, the wall velocity $v_w^{\text{LTE}}(T_\star)$ in the LTE approximation of [168], the transition strength of the hydrodynamic sector $\alpha_{\text{hyd}}(T_\star)$, and the inverse transition timescale β/H_\star . The last two columns indicate whether the dark sector is in thermal equilibrium with the SM plasma (C_T^{eq} of eq. (2.10)) and whether it is in hydrodynamic equilibrium with the SM ($C_{\text{hyd}}^{\text{eq}}$ of eq. (3.47)). All thermodynamic quantities are evaluated at $T_\star = T_p$.

While the softer EFT is applicable only over a relatively narrow region of parameter space, the resulting distributions in the $(\alpha_\star, \beta/H_\star)$ plane are robust and agree well with the soft EFT, cf. eq. (EFT1), for small values of the gauge coupling g_d . For larger couplings, however, the soft EFT naturally predicts denser regions extending towards smaller values of β/H_\star and larger values of α_\star , thereby moving closer to the PTA-favored region. The soft EFT therefore provides a less restrictive framework for assessing the compatibility of the model with the PTA observations.

In both scans of fig. 10, we impose the condition set by experimentally allowed portal couplings (2.9). Gray points correspond to $\epsilon_s > 0.1$. This is a liberal choice, as smaller values of ϵ_s significantly shrink the available parameter space and shift the density contours in fig. 10

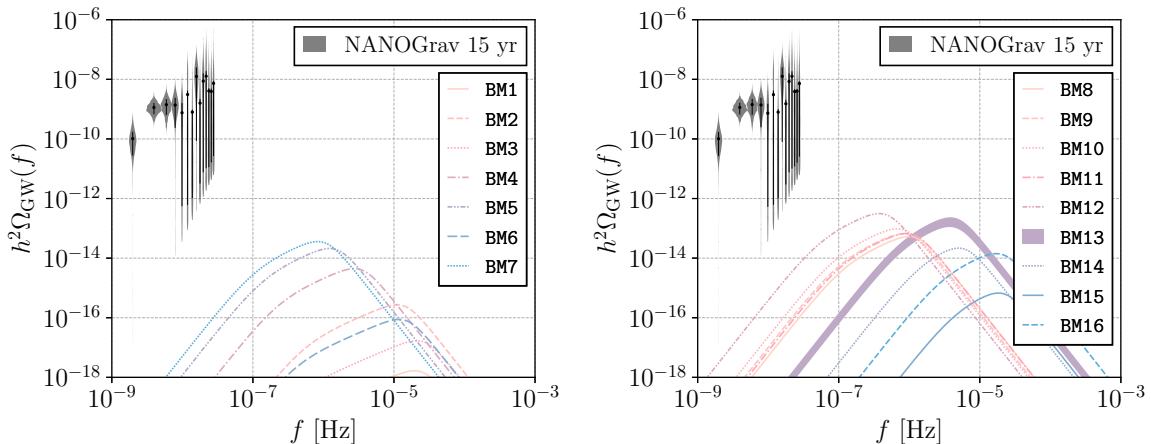


Figure 9: Left: Gravitational-wave spectra for the benchmark points BM1–BM7 listed in tab. 3, computed using the double broken power law template of eq. (DBPL). The NANOGrav $\mathcal{T} = 15$ yr data set [17] is shown for comparison. For BM13 of tab. 3, the 4d renormalization scale $\bar{\mu} = A\pi T$ is varied around $A = \{2^{-1}, 2^1\}$ as indicated by the band of the predicted GW signal. Right: BM8–BM16 of tab. 3.

towards larger β/H_\star , until all points are excluded once $\epsilon_s < \lambda_s$. These conclusions extend earlier assessments of the dark Abelian model in the PTA context, e.g. [49, 53]. Black circled points are out of thermal equilibrium (cf. eq. (2.10)), so that $T_{\text{DS}} \neq T_{\text{SM}}$. Treating them consistently requires tracking the dark-sector temperature T_{DS} after decoupling, whose ratio $\xi_{\text{DS}} = T_{\text{DS}}/T_{\text{SM}}$ explicitly enters the hydrodynamic computations of sec. 3. This procedure is beyond the scope of this work, but has been discussed in [49, 233].

The results of the scan shown in fig. 10 are broadly consistent with the findings of [49, 53, 191], which likewise concluded that the Abelian Higgs model does not reproduce the PTA-preferred region. In agreement with these studies, we find that compatibility with the PTA signal is achieved only after significant tuning at confidence levels above 2σ level.

For comparison, we also include in fig. 10 (right, orange) the corresponding density contours obtained using a Daisy-resummed treatment which is the softer EFT2 at full LO accuracy. In comparison, for our NLO computations the populated region extends towards lower values of β/H_\star and larger values of α_\star by approximately one order of magnitude. This shift is a genuine consequence of the EFT construction rather than a mere *thermal detail*.

At NLO, the soft and softer descriptions yield compatible results in the regime of mutual validity for small gauge couplings g_d . For larger couplings, however, the two approaches lead to quantitatively different phase-transition parameters and $(\alpha_\star, \beta/H_\star)$ populated parameter spaces. Nevertheless, the overall phenomenological conclusion remains unchanged. While the analysis of [53] is based on a LO thermal description, our NLO thermodynamics of sec. 3

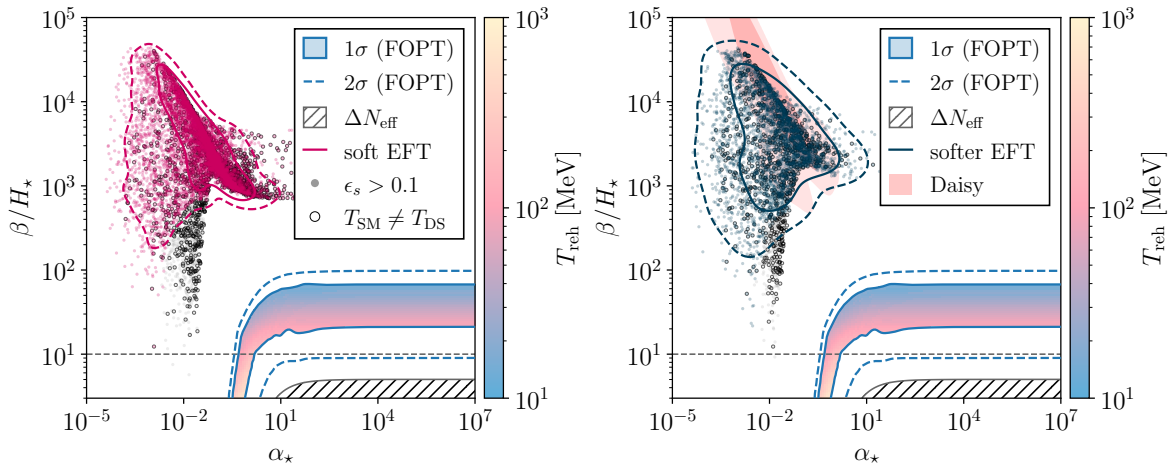


Figure 10: The 1σ and 2σ regions favored by current PTA data, described by the transition strength α_* and the inverse duration β/H_* of a generic dark sector first-order phase transition (light blue), assuming sound-wave induced GWs modelled with the doubly broken power-law template (DBPL) and the NANOGrav $\mathcal{T} = 15$ yr data set [17]. The colorbar on the right-hand side shows the best-fit reheating temperature T_{reh} , while the gray hatched region indicates the parameter space excluded by ΔN_{eff} constraints from BBN and CMB observations [47]. The dashed gray line marks values of β/H_* that are not supported by simulations [172]. For the soft **EFT1** (left, magenta) and the softer **EFT2** (right, dark blue) setups, the individual points show the values of α_* and β/H_* obtained in the parameter-space scan of tab. 2, and the contours give the corresponding 1σ (solid) and 2σ (dashed) density regions. Gray shaded points correspond to $\epsilon_s > 0.1$. Black circled points are out of thermal equilibrium with the SM plasma, failing the condition (2.10). In the right panel, we show the corresponding parameter space computed à la Daisy resummation (orange), as in [53].

demonstrates that the predicted phase-transition region remains well separated from the PTA-favored region. We therefore conclude that the incompatibility of the Abelian Higgs model with the current PTA data is robust against higher-order thermal corrections as well as the choice of thermal resummation scheme.

Having established the predictions of our EFT framework, it is instructive to compare them with previous analyses of the same model also at the level of the predicted spectra. Since these studies employ different treatments of the finite-temperature effective potential and thermal resummation, such a comparison helps isolate the origin of the differing phenomenological conclusions. Our analysis arrives at different conclusions than [54, 56], where the PTA-favored region was claimed to be compatible with the Abelian Higgs model as can also be seen in fig. 9 (right), which collects the benchmark points BM8–BM11 of [54], BM12 of [56], and BM13–BM16 of [58].

6. Conclusions

The possibility that the stochastic GW background reported by PTA collaborations originates from a cosmological first-order phase transition at MeV temperatures has attracted considerable interest in recent years. We revisited this scenario for a model class with a radiatively induced cubic barrier. As a representative fundamental model, we focused on a dark Abelian Higgs model, performing a precision study of the phase-transition thermodynamics using dimensionally reduced EFTs while also addressing the thermal and hydrodynamic contact between the dark and Standard Model sectors and the phenomenology of a fermionic dark matter candidate. Beyond identifying the parameter regions that yield an observable GW signal, we assessed the theoretical robustness of these predictions by systematically tracking the impact of thermal resummation, higher-order matching, renormalization-scale dependence, and higher-dimensional operators, using the Abelian Higgs model as a benchmark for which both perturbative and lattice results are available. Currently this is the highest level of precision in thermodynamics for PTA-era phase transitions.

We compared the resulting GW spectra with the current NANOGrav data using large parameter-space scans in tab. 2 and individual benchmark points in tab. 3. Because the region favored by current PTA data lies close to the boundary of validity of the finite-temperature description of the model, we first delineated where the predictions remain under theoretical control. To this end, we have identified three limiting sources of theoretical uncertainty:

- The high-temperature expansion breaks down, as expected for the strong transitions favored by the PTA data. The hierarchy between the soft and Debye scales, quantified by the ratio $h_3\phi_{\min}^2/m_D^2$, exceeds $\mathcal{O}(1)$, so that integrating out the temporal Debye scale is no longer parametrically justified.
- In the same regime, the dark gauge coupling g_d grows large enough to challenge a strict perturbative expansion.
- Where the effective theory remains under control, higher-order corrections only shift the predicted parameter space at large gauge coupling, while the predictions remain robust at small coupling. For the strongest transitions, higher-dimensional operators are expected to dominate over loop corrections [73, 130].

The strongest phase transitions accessible within the model push against this boundary, precisely where compatibility with the PTA signal would be maximal. Within the range where the effective theory remains theoretically controlled, the predicted phase-transition parameters remain well separated from the PTA-preferred region, despite a substantial shift of the predicted parameter space induced by higher-order thermal corrections at large gauge couplings. Reproducing the PTA-favored signal therefore requires significant tuning. Quantitative differences with previous studies arise from the state-of-the-art treatment of thermal

resummation in sec. 3, higher-order matching corrections in appendix C, and a systematic assessment of the validity of the effective field theory.

Phenomenological constraints (2.7) further shrink the viable parameter space. Assuming the dark scalar decays exclusively into Standard Model particles through Higgs mixing, the allowed window for the Higgs-dark scalar mixing angle, combined with the requirement that it decay before the onset of BBN, strongly disfavors dark scalar masses below $m_s \approx 3$ MeV. This further restricts the region that can be reconciled with the PTA observations.

We have also carefully examined the thermal history of the dark sector and the conditions required to maintain thermal contact with the Standard Model plasma. Owing to the small portal couplings implied by cosmological and experimental constraints, thermal equilibrium between the two sectors is not guaranteed *a priori*. By computing the relevant interaction rates and comparing them with the Hubble expansion rate, we showed that thermalization is predominantly maintained through the scalar portal, while the vector portal is typically ineffective in the parameter region of interest. We also identified a class of scattering processes mediated by dark-scalar self-interactions that, to the best of our knowledge, had not been included in previous analyses. Overall, we find that the dark and visible sectors remain in thermal equilibrium throughout the epoch of GW production across most of the parameter space. This justifies the use of a common temperature and the inclusion of both sectors in the relativistic degrees of freedom entering the GW redshift. Also decoupled regions are identified and must be treated accordingly; see [49, 233].

The interaction rates computed in this work also determine whether the dark and visible sectors remain hydrodynamically coupled during the phase transition. Comparing the mean free path associated with momentum transfer between the two sectors with the mean bubble separation allows us to assess whether this exchange is efficient and determine the relativistic degrees of freedom that enter the hydrodynamic description of the transition.

We further investigated the dark matter phenomenology of the model. For thermal freeze-out in the symmetric scenario, the gauge couplings required to obtain a strong first-order phase transition are generally incompatible with reproducing the observed relic abundance, while late-time annihilation constraints further restrict the viable parameter space. In contrast, asymmetric dark matter scenarios naturally accommodate the observed relic density over sizable regions of parameter space while remaining compatible with the phase-transition dynamics, illustrating the complementarity between GW observations and dark matter phenomenology. Moreover, we showed that the experimentally allowed range of the Higgs-dark scalar mixing angle significantly constrains the parameter space explored in our scan (cf. fig. 10), thereby affecting the compatibility of the model with the PTA-favored region.

Interpreting PTA observations with a particle-physics phase transition requires both viable phenomenology and quantitatively controlled finite-temperature calculations. Our analysis provides a precision blueprint for such studies. The framework in sec. 3 applies to a broad

class of gauge-Higgs models, such as non-Abelian gauge theories (3.8). There, gauge self-interactions may enhance the thermal barrier and yield stronger transitions in a more controlled perturbative regime. The framework can also be extended to the full NLO thermodynamics of classically scale-invariant models, where significant supercooling can arise. Natural next steps include incorporating higher-dimensional operators consistently in the nucleation dynamics and adopting frameworks that remain valid beyond the high-temperature regime.

Acknowledgements

The authors thank Carlo Tasillo and Tuomas V.I. Tenkanen for valuable discussions. We are grateful to Jorinde van de Vis for advice on the hydrodynamic equilibration condition and for many helpful comments during the preparation of this manuscript. We also thank Mikko Laine for comments on the manuscript. PS is supported by the Swiss National Science Foundation (SNSF) under grant PZ00P2-215997.

Data availability statement. The effective potential expressions used to produce figs. 3, and figs. 6–10 are publicly available via the software `DRalgo` [72]. Feynman diagrams were generated with `Axodraw` [234].

A. Master integrals

This appendix collects the master integrals used in the effective potential and the dimensional-reduction matching of sec. C. The d -dimensional integral measure is

$$\int_{\mathbf{p}} \equiv \int \frac{d^d \mathbf{p}}{(2\pi)^d} = \frac{2}{(4\pi)^2 \Gamma(\frac{d}{2})} \int_0^\infty dp p^{d-1}. \quad (\text{A.1})$$

A.1. Zero-temperature master integrals

At one-loop level and in dimensional regularization, the relevant class of master integrals in vacuum is

$$I_s^d(m_i) = I_{s;i}^d \equiv \left(\frac{\bar{\mu}^2 e^{\gamma_E}}{4\pi} \right)^\epsilon \int_{\mathbf{p}} \frac{1}{(P^2 + m_i^2)^s} = \left(\frac{\bar{\mu}^2 e^{\gamma_E}}{4\pi} \right)^\epsilon \frac{[m_i^2]^{\frac{d}{2}-s} \Gamma(s - \frac{d}{2})}{(4\pi)^{\frac{d}{2}} \Gamma(s)}. \quad (\text{A.2})$$

The Euclidean Passarino-Veltman integrals [235] are defined as:

$$\begin{aligned} A(m) &= \int_P \frac{1}{P^2 + m^2}, \\ B_{\{1;\mu;\mu\nu\}}(K; m_1, m_2) &= \int_P \frac{\{1; P_\mu; P_\mu P_\nu\}}{[P^2 + m_1^2][(K - P)^2 + m_2^2]}, \end{aligned} \quad (\text{A.3})$$

where $\int_P = \int \frac{d^D P}{(2\pi)^D}$ denotes the D -dimensional integral measure, and we define $B(K; m, m) \equiv B(K; m)$, and similarly for the rank-1 and 2 tensor integrals B_μ and $B_{\mu\nu}$. For vector self-energies, the following structures appear,

$$B_\mu(K; m_1, m_2) = \frac{1}{2} \frac{K_\mu}{K^2} \left\{ A(m_1) - A(m_2) - [K^2 + m_1^2 - m_2^2] B(K; m_1, m_2) \right\}, \quad (\text{A.4})$$

$$\begin{aligned} B_{\mu\nu}(K; m_1, m_2) &= \frac{1}{4(D-1)K^2} \left(\delta_{\mu\nu} - \frac{DK_\mu K_\nu}{K^2} \right) \\ &\quad \times \left\{ [K^2 - m_1^2 + m_2^2] A(m_1^2) + [K^2 - m_2^2 + m_1^2] A(m_2^2) \right. \\ &\quad \left. - [K^2 + (m_1 + m_2)^2] [K^2 + (m_1 - m_2)^2] B(K; m_1^2, m_2^2) \right\} \\ &\quad + \frac{K_\mu K_\nu}{K^2} \left\{ A(m_1^2) - m_2^2 B(K; m_1^2, m_2^2) \right\}. \end{aligned} \quad (\text{A.5})$$

The rank-1 tensor integral is proportional to the external momentum $B_\mu(K; m_1, m_2) = K_\mu C(K; m_1, m_2)$, and for the rank-2 tensor integral, we only need its transverse part $B_{\mu\nu}^{(T)}$ which is defined through $B_{\mu\nu} = B_{\mu\nu}^{(T)} (\delta_{\mu\nu} - \frac{K_\mu K_\nu}{K^2}) + \mathcal{O}(K_\mu K_\nu)$.

In $D = 4 - 2\epsilon$ dimensions, the master integrals evaluate to

$$\begin{aligned} A(m) &= I_1^D(m) \\ &\stackrel{D=4-2\epsilon}{=} -\frac{m^2}{(4\pi)^2} \left(\frac{\bar{\mu}^{-2\epsilon}}{\epsilon} + \left(\ln \frac{\bar{\mu}^2}{m^2} + 1 \right) + \mathcal{O}(\epsilon) \right), \end{aligned} \quad (\text{A.6})$$

$$\begin{aligned} B(K, m_1, m_2) &\stackrel{D=4-2\epsilon}{=} \frac{1}{(4\pi)^2} \left(\frac{\bar{\mu}^{-2\epsilon}}{\epsilon} \right. \\ &\quad \left. + \left[\ln \frac{\bar{\mu}^2}{m_1 m_2} + 1 - \frac{m_1^2 + m_2^2}{m_1^2 - m_2^2} \ln \frac{m_1}{m_2} + F\left(\frac{m_1}{K}, \frac{m_2}{K}\right) \right] + \mathcal{O}(\epsilon) \right). \end{aligned} \quad (\text{A.7})$$

Here, we defined

$$\begin{aligned} \text{Re } F(r_1, r_2) &= 1 + \left(\frac{r_1^2 + r_2^2}{r_1^2 - r_2^2} + r_1^2 - r_2^2 \right) \ln \frac{r_1}{r_2} \\ &\quad - 2 \text{Re} \sqrt{(r_1 - r_2)^2 + 1} \sqrt{(r_1 + r_2)^2 + 1} \operatorname{arctanh} \frac{\sqrt{(r_1 - r_2)^2 + 1}}{\sqrt{(r_1 + r_2)^2 + 1}}, \end{aligned} \quad (\text{A.8})$$

where $F(r_1, r_1) = F(r_1)$. Anticipating the analytic continuation to Minkowskian space-time, via $K \rightarrow -iK$, we also identify $F(r_1, r_2) = F(ir_1, ir_2)$. The function $\mathcal{F}(r_1, r_2)$ has the following special cases

$$\mathcal{F}(1) = 2 - \frac{\pi}{\sqrt{3}}, \quad \mathcal{F}(r) = 2 - 2\sqrt{4r^2 - 1} \arctan \frac{1}{\sqrt{4r^2 - 1}}. \quad (\text{A.9})$$

A.2. Thermal master integrals

The one-loop master integrals for the effective potential are given by

$$J_d(x) \equiv \frac{1}{2} \left(\frac{\bar{\mu}^2 e^{\gamma_E}}{4\pi} \right)^\epsilon \int_{\mathbf{p}} \ln(p^2 + x) = -\frac{1}{2} \left(\frac{\bar{\mu}^2 e^{\gamma_E}}{4\pi} \right)^\epsilon \frac{x^{\frac{d}{2}}}{(4\pi)^{\frac{d}{2}}} \frac{\Gamma(-\frac{d}{2})}{\Gamma(1)}, \quad (\text{A.10})$$

$$J_4(x) = -\frac{x^2}{4(4\pi)^2} \left(\frac{1}{\epsilon} + \ln \frac{\bar{\mu}^2}{x} + \frac{3}{2} + \mathcal{O}(\epsilon) \right), \quad (\text{A.11})$$

$$J_3(x) = -\frac{x^{\frac{3}{2}}}{12\pi} + \mathcal{O}(\epsilon). \quad (\text{A.12})$$

At one-loop level, the bosonic and fermionic master integrals decompose into a vacuum part and a thermal part. The hard thermal contributions Z^T and \tilde{Z}^T , for bosons and fermions respectively, can be evaluated numerically,

$$Z_{s;i}^\alpha = \not\int'_P \frac{p_n^\alpha}{[P^2 + m_i^2]^s}, \quad Z_{s;i}^0 = Z_{s;i} = \not\int'_P \frac{1}{[P^2 + m_i^2]^s} = I_{s;i}^4 + Z_{s;i}^T, \quad (\text{A.13})$$

$$\tilde{Z}_{s;i}^\alpha = \not\int_{\{P\}} \frac{p_n^\alpha}{[P^2 + m_i^2]^s}, \quad \tilde{Z}_{s;i}^0 = \tilde{Z}_{s;i} = \not\int_{\{P\}} \frac{1}{[P^2 + m_i^2]^s} = I_{s;i}^4 + \tilde{Z}_{s;i}^T, \quad (\text{A.14})$$

where $P \equiv (p_n, \mathbf{p})$ is the Euclidean four-momentum with Matsubara frequencies $p_n = 2n\pi T$ for bosons and $p_n = (2n+1)\pi T$ for fermions ($n \in \mathbb{Z}$). Curly braces on the sum-integral denote fermionic statistics, while a prime indicates that the bosonic zero mode is excluded. Similarly, the bosonic and fermionic logarithmic master integrals can be written as a Coleman-Weinberg vacuum part plus a thermal part,

$$J_i = \frac{1}{2} \not\int'_P \ln(P^2 + m_i^2) = J_i^4 + J_i^T, \quad \tilde{J}_i = \frac{1}{2} \not\int_{\{P\}} \ln(P^2 + m_i^2) = J_i^4 + \tilde{J}_i^T, \quad (\text{A.15})$$

with the corresponding 4d vacuum integral $J_i^d = J_d(m_i^2)$ from eq. (A.10).

The high-temperature expansion ($m_i \ll T$) of the master integrals in $d = 3 - 2\epsilon$ relevant for the hard scalar and fermionic pressure in eq. (3.25) is²⁶

$$\begin{aligned} J_i &= J_i^4 + J_i^T \\ &= -\frac{m_i^4}{4(4\pi)^2} \left(\frac{1}{\epsilon} + \ln \frac{\bar{\mu}^2}{m_i^2} + \frac{3}{2} \right) + J_i^T + \mathcal{O}(\epsilon) \\ m_i \ll T & \quad T^4 \left[-\frac{\zeta_4}{\pi^2} + \frac{1}{24} \frac{m_i^2}{T^2} - \frac{1}{4(4\pi)^2} \frac{m_i^4}{T^4} \left(\frac{1}{\epsilon} + L_b \right) + \mathcal{O}\left(\frac{m_i^6}{T^6}, \epsilon\right) \right], \quad (\text{A.16}) \\ \tilde{J}_i &= J_i^4 + \tilde{J}_i^T \end{aligned}$$

²⁶Vector bosons carry a dimension-dependent multiplicity, $J_i \rightarrow (D-1)J_i$, which modifies, e.g., the $\mathcal{O}(\epsilon^0)$ term in eq. (A.11).

$$\begin{aligned}
&= -\frac{m_i^4}{4(4\pi)^2} \left(\frac{1}{\epsilon} + \ln \frac{\bar{\mu}^2}{m_i^2} + \frac{3}{2} \right) + \tilde{J}_i^T + \mathcal{O}(\epsilon) \\
m_i \ll T & \quad T^4 \left[\frac{7}{8} \frac{\zeta_4}{\pi^2} - \frac{1}{48} \frac{m_i^2}{T^2} - \frac{1}{4(4\pi)^2} \frac{m_i^4}{T^4} \left(\frac{1}{\epsilon} + L_f \right) + \mathcal{O}\left(\frac{m_i^6}{T^6}, \epsilon\right) \right], \tag{A.17}
\end{aligned}$$

with $\zeta_4 = \frac{\pi^4}{90}$. Here, $\zeta_s = \zeta(s)$ for $\text{Re}(s) > 1$ is the Riemann zeta function, and $(\ln \zeta_s)' = \zeta'(s)/\zeta(s)$. To aid compactness, we defined a shorthand notation for the thermal logarithms

$$L_b \equiv 2 \ln \frac{\mu}{T} - 2(\ln(4\pi) - \gamma_E), \quad L_f \equiv L_b + 4 \ln 2, \tag{A.18}$$

where γ_E is the Euler-Mascheroni constant. Using the vacuum integrals of eq. (A.2) in $d = 4 - 2\epsilon$ dimensions, the corresponding contributions to the one-loop matching relations are

$$\begin{aligned}
\tilde{Z}_{1;i} &= I_{1;i}^4 + \tilde{Z}_{1;i}^T \\
&= -\frac{m_i^2}{(4\pi)^2} \left(\frac{1}{\epsilon} + \ln \frac{\bar{\mu}^2}{m_i^2} + 1 \right) + \tilde{Z}_{1;i}^T + \mathcal{O}(\epsilon) \\
m_i \ll T & \quad T^2 \left[-\frac{1}{24} - \frac{1}{(4\pi)^2} \frac{m_i^2}{T^2} \left(\frac{1}{\epsilon} + L_f \right) + \mathcal{O}\left(\frac{m_i^4}{T^4}, \epsilon\right) \right], \tag{A.19}
\end{aligned}$$

$$\begin{aligned}
\tilde{Z}_{2;i} &= I_{2;i}^4 + \tilde{Z}_{2;i}^T \\
&= \frac{1}{(4\pi)^2} \left(\frac{1}{\epsilon} + \ln \frac{\bar{\mu}^2}{m_i^2} \right) + \tilde{Z}_{2;i}^T + \mathcal{O}(\epsilon) \\
m_i \ll T & \quad \frac{1}{(4\pi)^2} \left(\frac{1}{\epsilon} + L_f \right) - 2 \frac{14\zeta_3}{(4\pi)^4} \frac{m_i^2}{T^2} + \mathcal{O}\left(\frac{m_i^4}{T^4}, \epsilon\right), \tag{A.20}
\end{aligned}$$

$$\begin{aligned}
\tilde{Z}_{3;i} &= I_{3;i}^4 + \tilde{Z}_{3;i}^T \\
&= \frac{1}{(4\pi)^2} \frac{1}{2m_i^2} + \tilde{Z}_{3;i}^T + \mathcal{O}(\epsilon) \\
m_i \ll T & \quad \frac{1}{T^2} \left[\frac{14\zeta_3}{(4\pi)^4} - 3 \frac{124\zeta_5}{(4\pi)^6} \frac{m_i^2}{T^2} + \mathcal{O}\left(\frac{m_i^4}{T^4}, \epsilon\right) \right], \tag{A.21}
\end{aligned}$$

$$\begin{aligned}
\tilde{Z}_{4;i} &= I_{4;i}^4 + \tilde{Z}_{4;i}^T \\
&= \frac{1}{(4\pi)^2} \frac{1}{6m_i^4} + \tilde{Z}_{4;i}^T + \mathcal{O}(\epsilon) \\
m_i \ll T & \quad \frac{1}{T^4} \left[\frac{124\zeta_5}{(4\pi)^6} - 4 \frac{1270\zeta_7}{(4\pi)^8} \frac{m_i^2}{T^2} + \mathcal{O}\left(\frac{m_i^4}{T^4}, \epsilon\right) \right], \tag{A.22}
\end{aligned}$$

where the explicit fermionic thermal integrals up to $\mathcal{O}(\epsilon^0)$ are

$$\tilde{J}_i^T = -T \int_{\mathbf{p}} \ln(1 - n_F(\omega_{p,i})), \tag{A.23}$$

$$\tilde{Z}_{1;i}^T = - \int_{\mathbf{p}} \frac{n_{\text{F}}(\omega_{p,i})}{\omega_{p,i}}, \quad (\text{A.24})$$

$$\tilde{Z}_{2;i}^T = - \frac{1}{2} \int_{\mathbf{p}} \frac{n_{\text{F}}(\omega_{p,i})}{p^2 \omega_{p,i}}, \quad (\text{A.25})$$

$$\tilde{Z}_{3;i}^T = - \frac{1}{8} \int_{\mathbf{p}} \frac{n_{\text{F}}(\omega_{p,i})}{p^2 \omega_{p,i}^2} \left[\frac{1}{\omega_{p,i}} + \frac{1 - n_{\text{F}}(\omega_{p,i})}{T} \right], \quad (\text{A.26})$$

$$\tilde{Z}_{4;i}^T = - \frac{1}{16} \int_{\mathbf{p}} \frac{n_{\text{F}}(\omega_{p,i})}{p^2 \omega_{p,i}^3} \left[\frac{1}{\omega_{p,i}^2} + \frac{1 - n_{\text{F}}(\omega_{p,i})}{\omega_{p,i} T} + \frac{(1 - n_{\text{F}}(\omega_{p,i}))(1 - 2n_{\text{F}}(\omega_{p,i}))}{3T^2} \right], \quad (\text{A.27})$$

with $\omega_{p,i} \equiv \sqrt{p^2 + m_i^2}$, m_i a general mass, and the Fermi distribution function $n_{\text{F}}(\omega) \equiv 1/(\exp(\omega/T) + 1)$.

B. Zero-temperature vacuum structure

B.1. Renormalization and one-loop β -functions

The renormalization group (RG) equations (β -functions) for the parameters of the model in eq. (2.1) encode their running with respect to the $\overline{\text{MS}}$ renormalization scale $\bar{\mu}$. Defining

$$t \equiv \ln \bar{\mu}^2, \quad (\text{B.1})$$

at one-loop level, we obtain

$$\partial_t g_d^2 = \frac{1}{(4\pi)^2} \frac{g_d^4}{3} (Y_s^2 + 4n_{\text{G}} Y_X^2), \quad (\text{B.2})$$

$$\partial_t \mu_s^2 = \frac{1}{(4\pi)^2} \mu_s^2 (4\lambda_s - 3g_d^2 Y_s^2), \quad (\text{B.3})$$

$$\partial_t \mu_X^2 = - \frac{3}{(4\pi)^2} \mu_X^2 g_d^2 Y_X^2, \quad (\text{B.4})$$

$$\partial_t \lambda_s = \frac{1}{(4\pi)^2} (10\lambda_s^2 - 6g_d^2 Y_s^2 \lambda_s + 3g_d^4 Y_s^4), \quad (\text{B.5})$$

given in terms of the hypercharge of the scalar and fermion fields, $Y_s = Y_X = 1$. For numerical evaluations, the input scale is chosen as the dark photon mass, $\bar{\mu}_0 = m_V$. The model parameters are evolved using eqs. (B.2)–(B.5), with the number of fermion generations n_{G} changing at the fermion threshold $\bar{\mu} \simeq m_X$.

In the 3dEFT, we employ a different RG scale, denoted by $\bar{\mu}_{3\text{d}}$,

$$t_3 \equiv \ln \bar{\mu}_{3\text{d}}. \quad (\text{B.6})$$

In the soft 3dEFT both the scalar and Debye masses obtain a non-zero β -function [61,67,236],

$$\partial_{t_3} \bar{\mu}_{s,3}^2 = \frac{4}{(4\pi)^2} \left(g_{d,3}^4 + \frac{1}{2} h_3^2 - 2g_{d,3}^2 \lambda_{s,3} + 2\lambda_{s,3}^2 \right), \quad (\text{B.7})$$

$$\partial_{t_3} m_D^2 = -\frac{4}{(4\pi)^2} \left(g_{d,3}^2 h_3 - h_3^2 - 24\kappa_3^2 \right), \quad (\text{B.8})$$

where the soft-EFT matching parameters $g_{d,3}$, $\lambda_{s,3}$ are defined in eqs. (C.2)–(C.7). In the softer 3dEFT only the scalar mass has a non-zero β -function,

$$\partial_{\bar{t}_3} \bar{\mu}_{s,3}^2 = \frac{4}{(4\pi)^2} \left(\bar{g}_{d,3}^4 - 2\bar{g}_{d,3}^2 \bar{\lambda}_{s,3} + 2\bar{\lambda}_{s,3}^2 \right), \quad (\text{B.9})$$

where $\bar{t}_3 \equiv \ln \bar{\mu}_{3d}$ and the barred softer-EFT matching parameters $\bar{g}_{d,3}$, $\bar{\lambda}_{s,3}$ are defined in eqs. (C.10)–(C.12).

B.2. Relations between $\overline{\text{MS}}$ -parameters and physical observables

The physical input parameters are related to the $\overline{\text{MS}}$ Lagrangian parameters of the model in eq. (2.1),

$$\{m_s, \alpha_d, m_V, m_X\} \mapsto \{\mu_s, g_d, \lambda_s, \mu_X\}, \quad (\text{B.10})$$

at the input scale $\bar{\mu} = \bar{\mu}_0$ taken as the physical dark photon mass,

$$\bar{\mu}_0 = m_V. \quad (\text{B.11})$$

After inverting the scalar mass eigenvalues (2.4), the $\overline{\text{MS}}$ mass parameter μ_s , scalar self-coupling, and fermion mass μ_X are related to the physical masses m_s , m_V , m_X in the broken phase using one-loop vacuum renormalization [46] with the relations

$$\mu_s^2(\bar{\mu}) = \frac{m_s^2}{2} \left[1 + \frac{\Pi_s(-m_s^2; \bar{\mu})}{m_s^2} \right], \quad \lambda_s(\bar{\mu}) = \frac{g_d^2 m_s^2}{2 m_V^2} \left[1 - \frac{\Pi_V(-m_V^2; \bar{\mu})}{m_V^2} + \frac{\Pi_s(-m_s^2; \bar{\mu})}{m_s^2} \right], \quad (\text{B.12})$$

and $\mu_X(\bar{\mu}) = m_X$ at the input scale $\bar{\mu} = \bar{\mu}_0$. Here, Π_s is the scalar and Π_V the vector one-loop self-energy evaluated at their respective pole mass, with the explicit expressions given in eqs. (B.21) and (B.22) below and in [46,97]. Thus, both higher-order corrections in the renormalization conditions and the momentum dependence of the pole masses are consistently included [62,225,237]. The expressions in eq. (B.12) hold at one-loop level and, in general, receive radiative corrections that can induce a further scale dependence.²⁷ Although m_X is an input parameter, the dark fermion is decoupled in the scans of sec. 5 and therefore does not enter the self-energies below.

²⁷In the Coleman-Weinberg limit $\lambda_s \ll g_d^2$, the scalar mass is loop-generated and satisfies $m_s \ll m_V$. The one-loop relations of eq. (B.12) then receive large higher-order corrections, and a consistent treatment requires resumming the scalar self-energy [159,238].

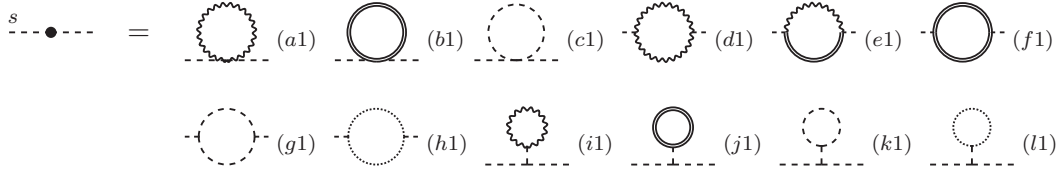


Figure 11: One-loop contributions to the vacuum Abelian Higgs model 2-point functions for the dark scalar s with implicit counterterms. Dashed lines denote the scalar s , double lines the Goldstone boson χ , wiggly lines dark vector V_μ , and dotted lines ghosts c, \bar{c} . Note that in $U(1)_d$ there is no $(V_\mu c \bar{c})$ vertex.

The masses m_s, m_V are analogs of the Higgs and Z -boson masses of the SM and, together with the fermion mass m_X , could in principle be determined experimentally. The dark gauge coupling $\alpha_d = g_d^2/(4\pi)$, in contrast, must be fixed by relating $g_d^2(\bar{\mu})$ to a physical observable, such as the analogue of the Fermi constant. The latter could be extracted from a four-fermion scattering amplitude. Since the dark model parameters are unknown in any case, we instead take the $\overline{\text{MS}}$ parameter $g_d^2(\bar{\mu})$ and the pole masses $\{m_s, m_V, m_X\}$ as direct inputs at μ_0 (B.11).

In our parameter scans of sec. 5, we trade the dark photon mass m_V for the scalar quartic λ_s via the tree-level relation $\lambda_s = \frac{g_d^2 m_s^2}{2 m_V^2}$ at $\bar{\mu}_0$, and scan over $\{m_s, \lambda_s, g_d\}$. The transition is insensitive to the dark fermion, since it remains Boltzmann suppressed for $m_X \gg m_V$ in the dark sector. All parameters are then evolved to the thermal matching scale $\bar{\mu}_{\text{ref}} = A\pi T$ of eq. (5.1) using the one-loop β -functions (B.2)–(B.5), where A is varied around unity to quantify the residual scale dependence.

Here, we detail the computation of the self-energies $\Pi(K^2; \bar{\mu})$ that enter the one-loop-corrected propagators *viz.*

$$\begin{aligned} \langle s(K)s(-K) \rangle &= \frac{1}{K^2 + m_s^2 - \Pi_s(K^2; \bar{\mu})}, \\ \langle V_\mu(K)V_\nu(-K) \rangle &= \frac{\delta_{\mu\nu} - \frac{K_\mu K_\nu}{K^2}}{K^2 + m_V^2 - \Pi_V^{(T)}(K^2; \bar{\mu})} + \mathcal{O}\left(\frac{K_\mu K_\nu}{K^2}\right). \end{aligned} \quad (\text{B.13})$$

The self-energies are computed at one-loop level in vacuum based on the diagrams in fig. 11 for the dark scalar and fig. 12 for the dark vector. The result for the dark scalar self-energy can readily be found in [46] and the dark vector self-energy in [97]. Our strategy is to compute both one-loop self-energies in dimensional regularization in $D = 4 - 2\epsilon$ Euclidean space-time dimensions and then perform the analytic continuation to Minkowskian space-time. We compute the results in general R_ξ gauge, where the gauge-fixing parameter is denoted by ξ as given in the ghost Lagrangian (cf. footnote 6) using the particle masses of eq. (2.4).

In Minkowskian space-time (subscript M), $\int_{\mathcal{P}} = \int \frac{dp^0}{2\pi} \int_{\mathbf{p}}$ denotes the $D = (d+1)$ -dimensional integral measure with $\int_{\mathbf{p}} = \int \frac{d^d \mathbf{p}}{(2\pi)^d}$ being its d -dimensional spatial part. The

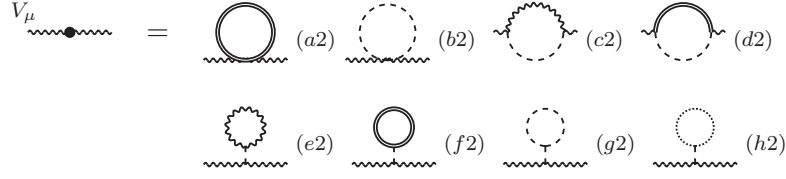


Figure 12: One-loop contributions to the vacuum Abelian Higgs model 2-point functions for the dark vector V_μ with implicit counterterms. Line prescription is as denoted in fig. 11.

analytic continuation from Euclidean to Minkowskian space-time is performed through $K \rightarrow -iK$, where the propagator in Minkowskian space-time is regulated by $\Delta \rightarrow \Delta + i\epsilon$.

Below, we list the individual diagrammatic contributions from fig. 11 to the scalar self-energy $\Pi_s(K^2; \bar{\mu})$ for $\xi = 1$ (Feynman gauge),

$$\begin{aligned}
\mathcal{D}_{(a1)} &= D g_d^2 A(m_V), & \mathcal{D}_{(b1)} &= \lambda_s A(m_V), \\
\mathcal{D}_{(c1)} &= 3\lambda_s A(m_s), & \mathcal{D}_{(d1)} &= -2D g_d^2 m_V^2 B(K, m_V), \\
\mathcal{D}_{(e1)} &= -g_d^2 (A(m_V) + (2K^2 - m_V^2)B(K, m_V)), & \mathcal{D}_{(f1)} &= -m_s^2 \lambda_s B(K, m_V), \\
\mathcal{D}_{(g1)} &= -9\lambda_s m_s^2 B(K, m_s), & \mathcal{D}_{(h1)} &= g_d^2 m_V^2 B(K, m_V), \\
\mathcal{D}_{(i1)} &= -3g_d^2 D A(m_V), & \mathcal{D}_{(j1)} &= -\frac{3}{2} g_d^2 \frac{m_s^2}{m_V^2} A(m_V), \\
\mathcal{D}_{(k1)} &= -\frac{9}{2} g_d^2 \frac{m_s^2}{m_V^2} A(m_s), & \mathcal{D}_{(l1)} &= 3g_d^2 A(m_V). \tag{B.14}
\end{aligned}$$

The transverse part of the vector self-energy $\Pi_V^{(T)}(K^2; \bar{\mu})$ from fig. 12 reads:

$$\begin{aligned}
\mathcal{D}_{(a2)}^{(T)} &= g_d^2 A(m_V), & \mathcal{D}_{(b2)}^{(T)} &= g_d^2 A(m_s), \\
\mathcal{D}_{(c2)}^{(T)} &= -4 g_d^2 m_V^2 B(K, m_s, m_V), & \mathcal{D}_{(d2)}^{(T)} &= -4g_d^2 D_{\mu\nu}^{(T)}(K; m_s, m_V), \\
\mathcal{D}_{(e2)}^{(T)} &= -2D g_d^2 \frac{m_V^2}{m_s^2} A(m_V), & \mathcal{D}_{(f2)}^{(T)} &= -g_d^2 A(m_V), \\
\mathcal{D}_{(g2)}^{(T)} &= -3g_d^2 A(m_s), & \mathcal{D}_{(h2)}^{(T)} &= 2g_d^2 \frac{m_V^2}{m_s^2} A(m_V). \tag{B.15}
\end{aligned}$$

Here, we used that eq. (2.4) in Feynman gauge implies $m_V = m_\chi = m_c$ in the minimum. To simplify, we use the on-shell relation

$$\lambda_s = \frac{g_d^2 m_s^2}{2 m_V^2} = \frac{g_d^2}{2} R_s^2, \quad R_s = \frac{m_s}{m_V}. \tag{B.16}$$

Two integral structures arising in the computation reduce to the basic integrals of eq. (A.3):

$$\mathcal{D}_{(e1)} \simeq \int_P \frac{(2K - P)^2}{[P^2 + m^2]} \frac{1}{[(K - P)^2 + m^2]} = A(m^2) + (2K^2 - m^2)B(K^2; m^2), \quad (\text{B.17})$$

$$\begin{aligned} \mathcal{D}_{(c2)} &\simeq \int_P \frac{(2P_\mu - K_\mu)(2P_\nu - K_\nu)}{[P^2 + m_s^2][(K - P)^2 + m_V^2]} \\ &= 4B_{\mu\nu}(K; m_s, m_V) - K_\mu K_\nu (4C(K; m_s, m_V) - B(K; m_s, m_V)), \end{aligned} \quad (\text{B.18})$$

where only the first term contributes to the transverse result. The self-energies are then obtained as

$$\begin{aligned} \Pi_s(K^2; m_s, m_V) &= \mathcal{D}_{(a1)} + \dots + \mathcal{D}_{(l1)} \\ &= -g_d^2 \left\{ \frac{9}{2} R_s^2 m_s^2 B(K; m_s) + \frac{(R_s^4 + 4(D - 1))m_s^2 + 4R_s^2 K^2}{2R_s^2} B(K; m_V) \right. \\ &\quad \left. + (R_s^2 + 2(D - 1))A(m_V) + 3R_s^2 A(m_s) \right\}, \end{aligned} \quad (\text{B.19})$$

$$\begin{aligned} \Pi_V^{(T)}(K^2; m_s, m_V) &= \mathcal{D}_{(a2)}^{(T)} + \dots + \mathcal{D}_{(h2)}^{(T)} \\ &= -2g_d^2 \left\{ 2B_{\mu\nu}^{(T)}(K; m_s, m_V) + 2m_V^2 B(K; m_s, m_V) \right. \\ &\quad \left. + A(m_s) + \frac{D - 1}{R_s^2} A(m_V) \right\}, \end{aligned} \quad (\text{B.20})$$

where $\Pi_V = \Pi_{\mu\nu}^{(T)}$. The vector self-energy agrees with [97] and the scalar self-energy with [46].

Finally, after analytically continuing the self-energies to Minkowskian space-time via $K \rightarrow -iK$ and employing the master integrals of eq. (A.9), we find the explicit expressions for the one-loop self-energies at the pole,

$$\begin{aligned} \Pi_s(-m_s^2; \bar{\mu}) &= \frac{g_d^2}{(4\pi)^2} m_s^2 \left[(2R_s^2 - 3) \ln \frac{\bar{\mu}^2}{m_V^2} - 3R_s^2 \ln R_s - \left(3 - \frac{9}{2} \mathcal{F}(1) \right) R_s^2 \right. \\ &\quad \left. - 1 - \frac{6}{R_s^2} + \frac{R_s^4 - 4R_s^2 + 12}{2R_s^2} \mathcal{F}(1/R_s) \right], \end{aligned} \quad (\text{B.21})$$

$$\begin{aligned} \Pi_V(-m_V^2; \bar{\mu}) &= \frac{g_d^2}{(4\pi)^2} \frac{m_V^2}{3} \left[- \left(9R_s^2 - 10 + \frac{18}{R_s^2} \right) \ln \frac{\bar{\mu}^2}{m_V^2} + 18R_s^2 \frac{R_s^2 - 2}{R_s^2 - 1} \ln R_s \right. \\ &\quad \left. - 11R_s^2 + \frac{26}{3} - \frac{6}{R_s^2} + (R_s^4 - 4R_s^2 + 12) \mathcal{F}(1, R_s) \right]. \end{aligned} \quad (\text{B.22})$$

C. Dimensional reduction details

The effective parameters of the dimensionally reduced theory setups (EFT1) and (EFT2) are collected below. Our independent computation here also agrees with the output of

DRalgo [129, 130] and the pure Abelian Higgs part of [46, 67, 73]. Both references employ the high-temperature expansion.

When constructing the soft EFT1, we follow the reasoning of [227] and apply the high-temperature expansion to the transitioning scalar field, $\mu_s \sim gT$, while keeping the inducing field, the Dirac fermion X , over a broader temperature range, $m_x > gT$, down to $m_x \gg T$, where it becomes Boltzmann suppressed. While in the broken phase, vector bosons also act as inducing fields, we keep them in the high-temperature limit during the matching. To accommodate fermion masses over a broad temperature range, including e.g. $m_x \sim T$, the thermal integrals are kept in general form during matching, as was done for a Majorana fermion in [239] and for EQCD in [240] and were recently automated using the hot Loop-Tree Duality technique [227, 241].

The one-loop bosonic and fermionic master integrals decompose into a vacuum part and a thermal part, Z^T for bosons and \tilde{Z}^T for fermions, that can be evaluated numerically; see eqs. (A.13)–(A.14) for the corresponding definitions. Since only the dark photon couples to the fermion, the sole fermionic one-loop contribution to the field normalizations appears in the $\mathcal{O}(p^2)$ term of the temporal and spatial dark photon correlators

$$\begin{aligned}
\Pi'_{V_0 V_0} &= \frac{g_d^2}{(4\pi)^2} \frac{1}{3} \left[L_b + 2 + 4n_G Y_X^2 \left(\ln \frac{\bar{\mu}^2}{\mu_X^2} - 1 + (4\pi)^2 (\tilde{Z}_{2;x}^T + 2\mu_X^2 \tilde{Z}_{3;x}^T) \right) \right] \\
&\stackrel{m_i \ll T}{=} \frac{g_d^2}{(4\pi)^2} \frac{1}{3} \left[L_b + 2 + 4n_G Y_X^2 (L_f - 1) \right], \\
\Pi'_{V_i V_i} &= \frac{g_d^2}{(4\pi)^2} \frac{1}{3} \left[L_b + 4n_G Y_X^2 \left(\ln \frac{\bar{\mu}^2}{\mu_X^2} + (4\pi)^2 \tilde{Z}_{2;x}^T \right) \right] \\
&\stackrel{m_i \ll T}{=} \frac{g_d^2}{(4\pi)^2} \frac{1}{3} \left[L_b + 4n_G Y_X^2 L_f \right]. \tag{C.1}
\end{aligned}$$

Here, we also displayed the respective high-temperature limits, $m_i \ll T$.

For n_G fermion generations, the gauge coupling and Debye mass one-loop matching relations are

$$g_{d,3}^2 = g_d^2 T \left[1 - \frac{g_d^2}{(4\pi)^2} \frac{1}{3} \left(L_b Y_s^2 + 4n_G Y_X^2 \left(\ln \frac{\bar{\mu}^2}{\mu_X^2} + (4\pi)^2 \tilde{Z}_{2;x}^T \right) \right) \right], \tag{C.2}$$

$$\begin{aligned}
m_D^2 &= g_d^2 T^2 \left(\frac{1}{3} - 4 \frac{Y_s^2}{(4\pi)^2} \frac{\mu_s^2}{T^2} \right) - 8n_G Y_X^2 g_d^2 \left(\tilde{Z}_{1;x}^T + \mu_X^2 \tilde{Z}_{2;x}^T \right) \\
&\quad - \frac{T^2}{(4\pi)^2} g_d^2 \left(\frac{L_b - 7}{9} g_d^2 Y_s^4 - \frac{4}{3} \lambda_s Y_s^2 \right), \tag{C.3}
\end{aligned}$$

where the scalar mass effect in the Debye mass is rooted in the high-temperature expansion.

The remaining matching relations for the thermal mass of the complex $U(1)_d$ singlet and its quartic couplings take the form

$$\begin{aligned} \mu_{s,3}^2 &= -\mu_s^2 + \frac{T^2}{12} (4\lambda_s + 3g_d^2 Y_s^2) + \frac{L_b}{(4\pi)^2} \mu_s^2 (4\lambda_s - 3g_d^2 Y_s^2) \\ &\quad - \frac{T^2}{(4\pi)^2} \frac{g_d^2 Y_s^2}{9} (2g_d^2 Y_s^2 - 6\lambda_s) - \frac{T^2}{(4\pi)^2} L_b \left(\frac{13}{12} g_d^4 Y_s^4 - 2g_d^2 Y_s^2 \lambda_s + \frac{10}{3} \lambda_s^2 \right) \\ &\quad - \left(c + \ln \frac{3T}{\bar{\mu}_{3d}} \right) \frac{1}{(4\pi)^2} \left(4g_{d,3}^4 Y_s^4 - 8g_{d,3}^2 \lambda_{s,3} Y_s^2 + 8\lambda_{s,3}^2 + \frac{h_3^2}{2} \right), \end{aligned} \quad (\text{C.4})$$

$$\lambda_{s,3} = T \left[\lambda_s + \frac{1}{(4\pi)^2} \left((2 - 3L_b) g_d^4 Y_s^4 + L_b (6g_d^2 Y_s^2 \lambda_s - 10\lambda_s^2) \right) \right], \quad (\text{C.5})$$

$$\begin{aligned} h_3 &= g_d^2 Y_s^2 T \left[1 - \frac{1}{(4\pi)^2} \left(\frac{L_b - 4}{3} Y_s^2 g_d^2 - 8\lambda_s \right. \right. \\ &\quad \left. \left. + \frac{4}{3} n_G Y_X^2 g_d^2 \left(\ln \frac{\bar{\mu}^2}{\mu_X^2} - 1 + (4\pi)^2 (\tilde{Z}_{2;x}^T + 2\mu_X^2 \tilde{Z}_{3;x}^T) \right) \right) \right], \end{aligned} \quad (\text{C.6})$$

$$\kappa_3 = T g_d^4 \left[\frac{16Y_s^4}{(4\pi)^2} + 192n_G Y_X^4 m_i^4 \tilde{Z}_{4;x}^T \right], \quad (\text{C.7})$$

where $c = \frac{1}{2} (\ln \frac{8\pi}{9} + (\ln \zeta_2)' - 2\gamma_E)$. For completeness, we also display the high-temperature-expanded fermionic contributions at two-loop level

$$m_D^2 \supset -\frac{T^2}{(4\pi)^2} \frac{g_d^4}{9} \left((L_b + 4L_f - 2) Y_s^2 Y_X^2 n_G + 18n_G Y_X^4 + 4(L_f - 1) Y_X^4 n_G^2 \right), \quad (\text{C.8})$$

$$\mu_{s,3}^2 \supset +\frac{T^2}{(4\pi)^2} g_d^4 Y_s^2 Y_X^2 n_G \left(\frac{1}{9} + \frac{L_f}{6} - \frac{L_b}{2} \right), \quad (\text{C.9})$$

where, due to the absence of a tree-level interaction, fermionic contributions to the scalar mass only start at two-loop level. In the matching relations used in practice, we truncate the fermionic effects after one loop order both in the Debye and scalar mass and relegate the computation of the corresponding two-loop thermal integrals, similar to [239, 240], to future work.

Integrating out the temporal vector boson V_0 from the soft theory yields the softer **EFT2**. The corresponding softer-EFT matching parameters read

$$\bar{g}_{d,3}^2 = g_{d,3}^2, \quad (\text{C.10})$$

$$\bar{\mu}_{s,3}^2 = \mu_{s,3}^2 - \frac{h_3 m_D}{(4\pi)} - \frac{h_3}{(4\pi)^2} \left[h_3 \left(1 + \ln \frac{\bar{\mu}_{3d}^2}{4m_D^2} \right) - \frac{\kappa_3}{24} \right], \quad (\text{C.11})$$

$$\bar{\lambda}_{s,3} = \lambda_{s,3} - \frac{1}{(4\pi)} \frac{h_3^2}{2m_D} + \frac{2}{(4\pi)^2} \frac{h_3^3}{m_D^2}. \quad (\text{C.12})$$

$$\mathcal{M}_{X\bar{X}\rightarrow VV} = \begin{array}{c} \text{---} \\ \text{---} \\ \text{---} \end{array} + \begin{array}{c} \text{---} \\ \text{---} \\ \text{---} \end{array}, \quad \mathcal{M}_{X\bar{X}\rightarrow SS^*} = \begin{array}{c} \text{---} \\ \text{---} \\ \text{---} \end{array}.$$

Figure 13: Diagrams for the dark matter pair annihilation and co-annihilation with the singlet scalar in the unbroken phase. The dark fermion X is displayed by an arrowed solid line, the complex scalar S by an arrowed dashed line, and dark photons by wiggly lines.

Here, we explicitly included the two-loop contributions for the softer scalar self-coupling $\bar{\lambda}_{s,3}$, since they are formally of $\mathcal{O}(g_d^4)$, which corresponds to NLO accuracy. The positive sign of this term improves convergence of the softer EFT close to T_c as indicated in [72, 228]. The successive contributions to $\bar{\lambda}_{s,3}$, namely $\lambda_{s,3}$, $h_3^2/(4\pi m_D)$ and $h_3^3/(4\pi m_D)^2$, scale as $g_d^2 T$, $g_d^3 T$ and $g_d^4 T$ under the power counting $h_3, \lambda_{s,3} \sim g_d^2 T$ and $m_D \sim g_d T$. Scaling out the common factor $\lambda_{s,3} \sim g_d^2 T$, the genuine dimensionless expansion parameter is the ratio of consecutive terms, $h_3/(4\pi m_D) \sim g_d$, so that the truncation is justified only for $h_3 \ll 4\pi m_D$; otherwise one should either use the soft theory directly or encode temporal effects to a softer-type EFT as described in sec. 3.1.

D. Annihilation cross-sections across the phase transition

This appendix collects the annihilation cross-sections relevant for the dark matter phenomenology discussed in sec. 4. We distinguish between the symmetric (sym) and broken (bro) phases of the dark gauge symmetry.

D.1. Symmetric phase

In the symmetric phase, the relevant annihilation channels are

$$X\bar{X} \rightarrow VV, \quad X\bar{X} \rightarrow SS^*. \quad (\text{D.1})$$

The corresponding tree-level diagrams are shown in fig. 13. The annihilation cross-sections, expressed in terms of the Mandelstam variable $s = (p_X + p_{\bar{X}})^2$, are

$$\sigma_{\text{ann}}^{\text{sym}} v_{\text{rel}}(X\bar{X} \rightarrow VV) = \frac{4\pi\alpha_d^2}{s} \left[-1 - \frac{4m_X^2}{s} + 2 \left(1 + \frac{4m_X^2}{s} - \frac{8m_X^4}{s^2} \right) \frac{\text{artanh}\left(\sqrt{1 - 4m_X^2/s}\right)}{\sqrt{1 - 4m_X^2/s}} \right], \quad (\text{D.2})$$

$$\sigma_{\text{ann}}^{\text{sym}} v_{\text{rel}}(X\bar{X} \rightarrow SS^*) = \frac{2\pi\alpha_d^2}{3s} \left(1 + \frac{2m_X^2}{s} \right). \quad (\text{D.3})$$

$$\begin{aligned}
\mathcal{M}_{X\bar{X}\rightarrow VV} &= \text{[Diagram 1]} + \text{[Diagram 2]}, \\
\mathcal{M}_{X\bar{X}\rightarrow Vs} &= \text{[Diagram 3]}, \\
\mathcal{M}_{X\bar{X}\rightarrow \chi s} &= \text{[Diagram 4]}.
\end{aligned}$$

Figure 14: Diagrams for the dark matter pair annihilation in the broken phase and in Feynman gauge. The dark fermion X is displayed by an arrowed solid line, the scalar s and the Goldstone χ by a dashed line, and dark photons by wiggly lines.

In the non-relativistic regime, relevant for thermal freeze-out and late-time annihilations, one may expand the cross-sections using $s = 4m_X^2/(1 - v_{\text{rel}}^2/4)$. The leading terms in the velocity expansion are

$$\sigma_{\text{ann}}^{\text{sym}} v_{\text{rel}}(X\bar{X} \rightarrow VV) = \frac{\pi\alpha_d^2}{m_X^2} + \mathcal{O}(v_{\text{rel}}^2), \quad (\text{D.4})$$

$$\sigma_{\text{ann}}^{\text{sym}} v_{\text{rel}}(X\bar{X} \rightarrow SS^*) = \frac{\pi\alpha_d^2}{4m_X^2} + \mathcal{O}(v_{\text{rel}}^2), \quad (\text{D.5})$$

which we have crosschecked also via a non-relativistic matching to dimension-six, velocity independent, operators [215, 242]. We find contribution to $\text{Im}[f(^1S_0)] = \pi\alpha^2$ solely from the annihilation into gauge boson and $\text{Im}[f(^3S_1)] = \pi\alpha^2/12$ for the annihilation into scalar pairs, where $^S L_J$ is the standard spectroscopic notation for orbital angular momentum, spin and total angular momentum. In this regime, non-perturbative effects become important. In particular, multiple exchanges of the vector mediator induce Sommerfeld enhancement and allow for bound-state formation, both of which modify the annihilation dynamics. In the main text, these effects are incorporated through the effective cross-section introduced in eq. (4.9).

D.2. Broken phase

After spontaneous symmetry breaking in the dark sector, additional annihilation channels become kinematically available. The relevant processes are

$$X\bar{X} \rightarrow VV, \quad X\bar{X} \rightarrow Vs, \quad X\bar{X} \rightarrow \chi s, \quad (\text{D.6})$$

where s denotes the physical dark scalar and χ the Goldstone boson. Throughout this appendix, we work in Feynman gauge ($\xi \rightarrow 1$). Accordingly, the Goldstone boson appears as an explicit propagating degree of freedom. Physical observables are recovered after consistently summing all contributions. The corresponding diagrams are shown in fig. 14.

The annihilation cross-sections into dark vectors, mixed vector-scalar states, and pure scalar states are given by

$$\sigma_{\text{ann}}^{\text{bro}} v_{\text{rel}}(X\bar{X} \rightarrow VV) = \frac{4\pi\alpha_d^2}{s} \sqrt{1 - \frac{4m_V^2}{s}} \left[\frac{2\left(1 + \frac{4m_X^2}{s} - \frac{8m_X^4}{s^2} - \frac{4m_X^2 m_V^2}{s^2} \left(2 - \frac{m_V^2}{m_X^2}\right)\right)}{\left(1 - \frac{2m_V^2}{s}\right) \sqrt{\left(1 - \frac{4m_X^2}{s}\right) \left(1 - \frac{4m_V^2}{s}\right)}} \right. \\ \left. \times \operatorname{artanh} \left(\frac{\sqrt{(s - 4m_X^2)(s - 4m_V^2)}}{s - 2m_V^2} \right) - \frac{1 + \frac{4m_X^2}{s} + \frac{2m_V^2}{sm_X^2}}{1 - \frac{4m_V^2}{s} + \frac{m_V^4}{sm_X^2}} \right], \quad (\text{D.7})$$

$$\sigma_{\text{ann}}^{\text{bro}} v_{\text{rel}}(X\bar{X} \rightarrow Vs) = \frac{4\pi\alpha_d^2}{s} \frac{m_V^2 (s + 2m_X^2)}{(s - m_V^2)^2} \left[\left(1 - \frac{(m_V + m_s)^2}{s}\right) \left(1 - \frac{(m_V - m_s)^2}{s}\right) \right]^{\frac{1}{2}}, \quad (\text{D.8})$$

$$\sigma_{\text{ann}}^{\text{bro}} v_{\text{rel}}(X\bar{X} \rightarrow \chi s) = \frac{2\pi\alpha_d^2}{3} \frac{(s + 2m_X^2)}{(s - m_V^2)^2} \left[\left(1 - \frac{(m_V + m_s)^2}{s}\right) \left(1 - \frac{(m_V - m_s)^2}{s}\right) \right]^{\frac{3}{2}}. \quad (\text{D.9})$$

As a consistency check, consider the limit $v_s \rightarrow 0$, which restores the $U(1)_d$ symmetry. In this limit, the scalar, Goldstone, and vector masses vanish, cf. eq. (2.4), and the expressions above reduce to the corresponding symmetric-phase cross-sections in eqs. (D.2) and (D.3). Assuming $m_X \gg m_V$ and $m_X \gg m_s$, as in our analysis, the leading terms of the non-relativistic expansion are

$$\sigma_{\text{ann}}^{\text{bro}} v_{\text{rel}}(X\bar{X} \rightarrow VV) = \frac{\pi\alpha_d^2}{m_X^2} \left(1 - \frac{m_V^2}{2m_X^2}\right), \quad (\text{D.10})$$

$$\sigma_{\text{ann}}^{\text{bro}} v_{\text{rel}}(X\bar{X} \rightarrow Vs) = \frac{3\pi\alpha_d^2}{8m_X^2} \left(\frac{m_V}{m_X}\right)^2, \quad (\text{D.11})$$

$$\sigma_{\text{ann}}^{\text{bro}} v_{\text{rel}}(X\bar{X} \rightarrow \chi s) = \frac{\pi\alpha_d^2}{4m_X^2} \left(1 - \frac{m_V^2}{4m_X^2} - \frac{3m_s^2}{m_X^2}\right), \quad (\text{D.12})$$

shown to $\mathcal{O}(m_V^2/m_X^2)$ and $\mathcal{O}(m_s^2/m_X^2)$.

References

- [1] A. Strumia and F. Vissani, *Neutrino masses and mixings and...* [[hep-ph/0606054](#)].
- [2] Y. Cai, J. Herrero-García, M. A. Schmidt, A. Vicente, and R. R. Volkas, *From the trees to the forest: a review of radiative neutrino mass models*, *Front. in Phys.* **5** (2017) 63 [[1706.08524](#)].
- [3] M. Sajjad Athar *et al.*, *Status and perspectives of neutrino physics*, *Prog. Part. Nucl. Phys.* **124** (2022) 103947 [[2111.07586](#)].

- [4] V. C. Rubin, N. Thonnard, and W. K. Ford, Jr., *Rotational properties of 21 SC galaxies with a large range of luminosities and radii, from NGC 4605 /R = 4kpc/ to UGC 2885 /R = 122 kpc/*, *Astrophys. J.* **238** (1980) 471.
- [5] A. Bosma, *21-cm line studies of spiral galaxies. 2. The distribution and kinematics of neutral hydrogen in spiral galaxies of various morphological types.*, *Astron. J.* **86** (1981) 1825.
- [6] **Planck** Collaboration, N. Aghanim *et al.*, *Planck 2018 results. VI. Cosmological parameters*, *Astron. Astrophys.* **641** (2020) A6 [1807.06209].
- [7] G. Bertone and D. Hooper, *History of dark matter*, *Rev. Mod. Phys.* **90** (2018) 045002 [1605.04909].
- [8] **WMAP** Collaboration, C. L. Bennett *et al.*, *Nine-Year Wilkinson Microwave Anisotropy Probe (WMAP) Observations: Final Maps and Results*, *Astrophys. J. Suppl.* **208** (2013) 20 [1212.5225].
- [9] G. Arcadi, M. Dutra, P. Ghosh, *et al.*, *The waning of the WIMP? A review of models, searches, and constraints*, *Eur. Phys. J. C* **78** (2018) 203 [1703.07364].
- [10] C. Caprini, M. Hindmarsh, S. Huber, *et al.*, *Science with the space-based interferometer eLISA. II: Gravitational waves from cosmological phase transitions*, *JCAP* **04** (2016) 001 [1512.06239].
- [11] **LISA** Collaboration, P. Amaro-Seoane *et al.*, *Laser Interferometer Space Antenna*, [1702.00786].
- [12] W.-H. Ruan, Z.-K. Guo, R.-G. Cai, and Y.-Z. Zhang, *Taiji program: Gravitational-wave sources*, *Int. J. Mod. Phys. A* **35** (2020) 2050075 [1807.09495].
- [13] M. J. Ramsey-Musolf, *The electroweak phase transition: a collider target*, *JHEP* **09** (2020) 179 [1912.07189].
- [14] L. S. Friedrich, M. J. Ramsey-Musolf, T. V. I. Tenkanen, and V. Q. Tran, *Addressing the Gravitational Wave - Collider Inverse Problem*, [2203.05889].
- [15] M. J. Ramsey-Musolf, T. V. I. Tenkanen, and V. Q. Tran, *Refining Gravitational Wave and Collider Physics Dialogue via Singlet Scalar Extension*, [2409.17554].
- [16] **NANOGrav** Collaboration, Z. Arzoumanian *et al.*, *The NANOGrav 12.5 yr Data Set: Search for an Isotropic Stochastic Gravitational-wave Background*, *Astrophys. J. Lett.* **905** (2020) L34 [2009.04496].
- [17] **NANOGrav** Collaboration, G. Agazie *et al.*, *The NANOGrav 15-year Data Set: Evidence for a Gravitational-Wave Background*, [2306.16213].
- [18] **EPTA** Collaboration, S. Chen *et al.*, *Common-red-signal analysis with 24-yr high-precision timing of the European Pulsar Timing Array: inferences in the stochastic gravitational-wave background search*, *Mon. Not. Roy. Astron. Soc.* **508** (2021) 4970 [2110.13184].
- [19] **EPTA, InPTA:** Collaboration, J. Antoniadis *et al.*, *The second data release from the European Pulsar Timing Array - III. Search for gravitational wave signals*, *Astron. Astrophys.* **678** (2023) A50 [2306.16214].

- [20] **EPTA, InPTA** Collaboration, J. Antoniadis *et al.*, *The second data release from the European Pulsar Timing Array - IV. Implications for massive black holes, dark matter, and the early Universe*, *Astron. Astrophys.* **685** (2024) A94 [2306.16227].
- [21] B. Goncharov *et al.*, *On the Evidence for a Common-spectrum Process in the Search for the Nanohertz Gravitational-wave Background with the Parkes Pulsar Timing Array*, *Astrophys. J. Lett.* **917** (2021) L19 [2107.12112].
- [22] D. J. Reardon *et al.*, *Search for an Isotropic Gravitational-wave Background with the Parkes Pulsar Timing Array*, *Astrophys. J. Lett.* **951** (2023) L6 [2306.16215].
- [23] H. Xu *et al.*, *Searching for the Nano-Hertz Stochastic Gravitational Wave Background with the Chinese Pulsar Timing Array Data Release I*, *Res. Astron. Astrophys.* **23** (2023) 075024 [2306.16216].
- [24] M. T. Miles *et al.*, *The MeerKAT Pulsar Timing Array: the first search for gravitational waves with the MeerKAT radio telescope*, *Mon. Not. Roy. Astron. Soc.* **536** (2024) 1489 [2412.01153].
- [25] R. w. Hellings and G. s. Downs, *UPPER LIMITS ON THE ISOTROPIC GRAVITATIONAL RADIATION BACKGROUND FROM PULSAR TIMING ANALYSIS*, *Astrophys. J. Lett.* **265** (1983) L39.
- [26] H. Middleton, A. Sesana, S. Chen, A. Vecchio, W. Del Pozzo, and P. A. Rosado, *Retracted: Correction to: Massive black hole binary systems and the NANOGrav 12.5 yr results*, *Mon. Not. Roy. Astron. Soc.* **502** (2021) L99 [2011.01246].
- [27] D. Izquierdo-Villalba, A. Sesana, S. Bonoli, and M. Colpi, *Massive black hole evolution models confronting the n-Hz amplitude of the stochastic gravitational wave background*, *Mon. Not. Roy. Astron. Soc.* **509** (2021) 3488 [2108.11671].
- [28] M. Curyło and T. Bulik, *Predictions for LISA and PTA based on SHARK galaxy simulations*, *Astron. Astrophys.* **660** (2022) A68 [2108.11232].
- [29] M. Milosavljevic and D. Merritt, *The Final parsec problem*, *AIP Conf. Proc.* **686** (2003) 201 [astro-ph/0212270].
- [30] **NANOGrav** Collaboration, A. Afzal *et al.*, *The NANOGrav 15-year Data Set: Search for Signals from New Physics*, [2306.16219].
- [31] W. Buchmuller, V. Domcke, and K. Schmitz, *From NANOGrav to LIGO with metastable cosmic strings*, *Phys. Lett. B* **811** (2020) 135914 [2009.10649].
- [32] P. Athron, A. Fowlie, C.-T. Lu, *et al.*, *Can Supercooled Phase Transitions Explain the Gravitational Wave Background Observed by Pulsar Timing Arrays?*, *Phys. Rev. Lett.* **132** (2024) 221001 [2306.17239].
- [33] T. Hambye and A. Strumia, *Dynamical generation of the weak and Dark Matter scale*, *Phys. Rev. D* **88** (2013) 055022 [1306.2329].
- [34] C. D. Carone and R. Ramos, *Classical scale-invariance, the electroweak scale and vector dark matter*, *Phys. Rev. D* **88** (2013) 055020 [1307.8428].

- [35] M. Kierkla, A. Karam, and B. Swiezewska, *Conformal model for gravitational waves and dark matter: a status update*, JHEP **03** (2023) 007 [2210.07075].
- [36] M. Kierkla, B. Swiezewska, T. V. I. Tenkanen, and J. van de Vis, *Gravitational waves from supercooled phase transitions: dimensional transmutation meets dimensional reduction*, JHEP **02** (2024) 234 [2312.12413].
- [37] M. Kierkla, P. Schicho, B. Swiezewska, T. V. I. Tenkanen, and J. van de Vis, *Finite-temperature bubble nucleation with shifting scale hierarchies*, JHEP **07** (2025) 153 [2503.13597].
- [38] M. Kierkla, N. Ramberg, P. Schicho, and D. Schmitt, *Thermodynamical uncertainties for primordial black holes from cosmological phase transitions*, Phys. Rev. D **113** (2026) 095024 [2506.15496].
- [39] E. Madge, E. Morgante, C. Puchades-Ibáñez, *et al.*, *Primordial gravitational waves in the nano-Hertz regime and PTA data — towards solving the GW inverse problem*, JHEP **10** (2023) 171 [2306.14856].
- [40] S. Balan, T. Bringmann, F. Kahlhoefer, J. Matuszak, and C. Tasillo, *Sub-GeV dark matter and nano-Hertz gravitational waves from a classically conformal dark sector*, JCAP **08** (2025) 062 [2502.19478].
- [41] J. Gonçalves, D. Marfatia, A. P. Morais, and R. Pasechnik, *Supercooled phase transitions in conformal dark sectors explain NANOGrav data*, Phys. Lett. B **869** (2025) 139829 [2501.11619].
- [42] M. Christiansen, E. Madge, C. Puchades-Ibáñez, M. E. Ramirez-Quezada, and P. Schwaller, *Beyond the daisy chain: running and the 3D EFT view of supercooled phase transitions*, JHEP **05** (2026) 014 [2511.02910].
- [43] G. C. Dorsch, S. J. Huber, and J. M. No, *A strong electroweak phase transition in the 2HDM after LHC8*, JHEP **10** (2013) 029 [1305.6610].
- [44] K. Hashino, M. Kakizaki, S. Kanemura, P. Ko, and T. Matsui, *Gravitational waves and Higgs boson couplings for exploring first order phase transition in the model with a singlet scalar field*, Phys. Lett. B **766** (2017) 49 [1609.00297].
- [45] N. Benincasa, A. Hryczuk, K. Kannike, and M. Laletin, *Phase transitions and gravitational waves in a model of \mathbb{Z}_3 scalar dark matter*, JHEP **02** (2024) 207 [2312.04627].
- [46] K. Kajantie, M. Karjalainen, M. Laine, and J. Peisa, *Three-dimensional $U(1)$ gauge + Higgs theory as an effective theory for finite temperature phase transitions*, Nucl. Phys. B **520** (1998) 345 [hep-lat/9711048].
- [47] T.-H. Yeh, J. Shelton, K. A. Olive, and B. D. Fields, *Probing physics beyond the standard model: limits from BBN and the CMB independently and combined*, JCAP **10** (2022) 046 [2207.13133].
- [48] M. Kawasaki, K. Kohri, T. Moroi, and Y. Takaesu, *Revisiting Big-Bang Nucleosynthesis Constraints on Long-Lived Decaying Particles*, Phys. Rev. D **97** (2018) 023502 [1709.01211].
- [49] T. Bringmann, P. F. Depta, T. Konstandin, K. Schmidt-Hoberg, and C. Tasillo, *Does NANOGrav observe a dark sector phase transition?*, JCAP **11** (2023) 053 [2306.09411].

- [50] A. Addazi, Y.-F. Cai, A. Marciano, and L. Visinelli, *Have pulsar timing array methods detected a cosmological phase transition?*, Phys. Rev. D **109** (2024) 015028 [2306.17205].
- [51] T. Ghosh, A. Ghoshal, H.-K. Guo, *et al.*, *Did we hear the sound of the Universe boiling? Analysis using the full fluid velocity profiles and NANOGrav 15-year data*, JCAP **05** (2024) 100 [2307.02259].
- [52] M. W. Winkler and K. Freese, *Origin of the stochastic gravitational wave background: First-order phase transition versus black hole mergers*, Phys. Rev. D **111** (2025) 083509 [2401.13729].
- [53] T. Bringmann, T. Konstandin, J. Matuszak, K. Schmidt-Hoberg, and C. Tasillo, *Tuning the violins: dark sector phase transition models for the PTA signal*, [2602.09092].
- [54] C. Han, K.-P. Xie, J. M. Yang, and M. Zhang, *Self-interacting dark matter implied by nano-Hertz gravitational waves*, Phys. Rev. D **109** (2024) 115025 [2306.16966].
- [55] P. Di Bari and M. H. Rahat, *Split Majoron model confronts the NANOGrav signal and cosmological tensions*, Phys. Rev. D **110** (2024) 055019 [2307.03184].
- [56] A. Banik, Y. Cui, Y.-D. Tsai, and Y. Tsai, *The Sound of Dark Sectors in Pulsar Timing Arrays*, [2412.16282].
- [57] W.-Z. Feng and Z.-H. Zhang, *Gauge-independent gravitational waves from a minimal dark U(1) sector with viable dark matter candidates*, [2602.14866].
- [58] F. Costa, J. Hoefken Zink, M. Lucente, S. Pascoli, and S. Rosauero-Alcaraz, *Supercooled dark scalar phase transitions explanation of NANOGrav data*, Phys. Lett. B **868** (2025) 139634 [2501.15649].
- [59] P. Ginsparg, *First and second order phase transitions in gauge theories at finite temperature*, Nucl. Phys. B **170** (1980) 388.
- [60] T. Appelquist and R. D. Pisarski, *High-temperature Yang-Mills theories and three-dimensional quantum chromodynamics*, Phys. Rev. D **23** (1981) 2305.
- [61] K. Farakos, K. Kajantie, K. Rummukainen, and M. E. Shaposhnikov, *3-D physics and the electroweak phase transition: Perturbation theory*, Nucl. Phys. B **425** (1994) 67 [hep-ph/9404201].
- [62] K. Kajantie, M. Laine, K. Rummukainen, and M. E. Shaposhnikov, *Generic rules for high temperature dimensional reduction and their application to the standard model*, Nucl. Phys. B **458** (1996) 90 [hep-ph/9508379].
- [63] E. Braaten and A. Nieto, *Effective field theory approach to high temperature thermodynamics*, Phys. Rev. D **51** (1995) 6990 [hep-ph/9501375].
- [64] K. Kajantie, M. Laine, K. Rummukainen, and M. E. Shaposhnikov, *Is there a hot electroweak phase transition at $m_H \gtrsim m_W$?*, Phys. Rev. Lett. **77** (1996) 2887 [hep-ph/9605288].
- [65] O. Gould and J. Hirvonen, *Effective field theory approach to thermal bubble nucleation*, Phys. Rev. D **104** (2021) 096015 [2108.04377].

- [66] J. Löfgren, M. J. Ramsey-Musolf, P. Schicho, and T. V. I. Tenkanen, *Nucleation at Finite Temperature: A Gauge-Invariant Perturbative Framework*, Phys. Rev. Lett. **130** (2023) 251801 [2112.05472].
- [67] J. Hirvonen, J. Löfgren, M. J. Ramsey-Musolf, P. Schicho, and T. V. I. Tenkanen, *Computing the gauge-invariant bubble nucleation rate in finite temperature effective field theory*, JHEP **07** (2022) 135 [2112.08912].
- [68] O. Gould and T. V. I. Tenkanen, *On the perturbative expansion at high temperature and implications for cosmological phase transitions*, JHEP **06** (2021) 069 [2104.04399].
- [69] E. J. Weinberg, *Vacuum decay in theories with symmetry breaking by radiative corrections*, Phys. Rev. D **47** (1993) 4614 [hep-ph/9211314].
- [70] D. Metaxas and E. J. Weinberg, *Gauge independence of the bubble nucleation rate in theories with radiative symmetry breaking*, Phys. Rev. D **53** (1996) 836 [hep-ph/9507381].
- [71] M. Garny and T. Konstandin, *On the gauge dependence of vacuum transitions at finite temperature*, JHEP **07** (2012) 189 [1205.3392].
- [72] A. Ekstedt, P. Schicho, and T. V. I. Tenkanen, *Cosmological phase transitions at three loops: The final verdict on perturbation theory*, Phys. Rev. D **110** (2024) 096006 [2405.18349].
- [73] F. Bernardo, P. Klose, P. Schicho, and T. V. I. Tenkanen, *Higher-dimensional operators at finite temperature affect gravitational-wave predictions*, JHEP **08** (2025) 109 [2503.18904].
- [74] D. Croon, V. Sanz, and G. White, *Model Discrimination in Gravitational Wave spectra from Dark Phase Transitions*, JHEP **08** (2018) 203 [1806.02332].
- [75] B. Patt and F. Wilczek, *Higgs-field portal into hidden sectors*, [hep-ph/0605188].
- [76] M. Pospelov, A. Ritz, and M. B. Voloshin, *Secluded WIMP Dark Matter*, Phys. Lett. B **662** (2008) 53 [0711.4866].
- [77] J. March-Russell, S. M. West, D. Cumberbatch, and D. Hooper, *Heavy Dark Matter Through the Higgs Portal*, JHEP **07** (2008) 058 [0801.3440].
- [78] P. Galison and A. Manohar, *TWO Z's OR NOT TWO Z's?*, Phys. Lett. B **136** (1984) 279.
- [79] B. Holdom, *Two U(1)'s and Epsilon Charge Shifts*, Phys. Lett. B **166** (1986) 196.
- [80] P. F. Depta, M. Hufnagel, and K. Schmidt-Hoberg, *Updated BBN constraints on electromagnetic decays of MeV-scale particles*, JCAP **04** (2021) 011 [2011.06519].
- [81] M. Escudero Abenza, *Precision early universe thermodynamics made simple: N_{eff} and neutrino decoupling in the Standard Model and beyond*, JCAP **05** (2020) 048 [2001.04466].
- [82] D. J. Fixsen, E. S. Cheng, J. M. Gales, J. C. Mather, R. A. Shafer, and E. L. Wright, *The Cosmic Microwave Background spectrum from the full COBE FIRAS data set*, Astrophys. J. **473** (1996) 576 [astro-ph/9605054].
- [83] J. Chluba and R. A. Sunyaev, *The evolution of CMB spectral distortions in the early Universe*, Mon. Not. Roy. Astron. Soc. **419** (2012) 1294 [1109.6552].

- [84] X.-L. Chen and M. Kamionkowski, *Particle decays during the cosmic dark ages*, Phys. Rev. D **70** (2004) 043502 [astro-ph/0310473].
- [85] **Planck** Collaboration, N. Aghanim *et al.*, *Planck 2018 results. I. Overview and the cosmological legacy of Planck*, Astron. Astrophys. **641** (2020) A1 [1807.06205].
- [86] J. L. Feng and J. Kumar, *The WIMPlless Miracle: Dark-Matter Particles without Weak-Scale Masses or Weak Interactions*, Phys. Rev. Lett. **101** (2008) 231301 [0803.4196].
- [87] J. L. Feng, H. Tu, and H.-B. Yu, *Thermal Relics in Hidden Sectors*, JCAP **10** (2008) 043 [0808.2318].
- [88] N. Arkani-Hamed, D. P. Finkbeiner, T. R. Slatyer, and N. Weiner, *A Theory of Dark Matter*, Phys. Rev. D **79** (2009) 015014 [0810.0713].
- [89] N. F. Bell, Y. Cai, and R. K. Leane, *Dark Forces in the Sky: Signals from Z' and the Dark Higgs*, JCAP **08** (2016) 001 [1605.09382].
- [90] M. Duerr, F. Kahlhoefer, K. Schmidt-Hoberg, T. Schwetz, and S. Vogl, *How to save the WIMP: global analysis of a dark matter model with two s -channel mediators*, JHEP **09** (2016) 042 [1606.07609].
- [91] J. A. Evans, S. Gori, and J. Shelton, *Looking for the WIMP Next Door*, JHEP **02** (2018) 100 [1712.03974].
- [92] T. S. Evans and A. C. Pearson, *Real time thermal propagators for massive gauge bosons*, Zeitschrift für Phys. C Part. Fields **65** (1993) 123 [9307229].
- [93] P. B. Arnold and O. Espinosa, *The Effective potential and first order phase transitions: Beyond leading-order*, Phys. Rev. D **47** (1993) 3546 [hep-ph/9212235].
- [94] S. Mo, J. Hove, and A. Sudbo, *The Order of the metal to superconductor transition*, Phys. Rev. B **65** (2002) 104501 [cond-mat/0109260].
- [95] H. Kleinert, *DISORDER VERSION OF THE ABELIAN HIGGS MODEL AND THE ORDER OF THE SUPERCONDUCTIVE PHASE TRANSITION*, Lett. Nuovo Cim. **35** (1982) 405.
- [96] I. F. Herbut and Z. Tesanovic, *Critical fluctuations in superconductors and the magnetic field penetration depth*, Phys. Rev. Lett. **76** (1996) 4588 [cond-mat/9605185].
- [97] S. Kim and M. Laine, *On thermal corrections to near-threshold annihilation*, J. Cosmol. Astropart. Phys. **2017** (2017) 013 [1609.00474].
- [98] S. P. Martin and H. H. Patel, *Two-loop effective potential for generalized gauge fixing*, Phys. Rev. D **98** (2018) 076008 [1808.07615].
- [99] J. Berger, K. Jedamzik, and D. G. E. Walker, *Cosmological Constraints on Decoupled Dark Photons and Dark Higgs*, JCAP **11** (2016) 032 [1605.07195].
- [100] A. Fradette, M. Pospelov, J. Pradler, and A. Ritz, *Cosmological Constraints on Very Dark Photons*, Phys. Rev. D **90** (2014) 035022 [1407.0993].

- [101] A. Fradette, M. Pospelov, J. Pradler, and A. Ritz, *Cosmological beam dump: constraints on dark scalars mixed with the Higgs boson*, Phys. Rev. D **99** (2019) 075004 [1812.07585].
- [102] J.-T. Li, G. M. Fuller, and E. Grohs, *Probing dark photons in the early universe with big bang nucleosynthesis*, JCAP **12** (2020) 049 [2009.14325].
- [103] M. Ibe, S. Kobayashi, Y. Nakayama, and S. Shirai, *Cosmological constraints on dark scalar*, JHEP **03** (2022) 198 [2112.11096].
- [104] **NA62** Collaboration, E. Cortina Gil *et al.*, *Measurement of the very rare $K^+ \rightarrow \pi^+ \nu \bar{\nu}$ decay*, JHEP **06** (2021) 093 [2103.15389].
- [105] **BNL-E949** Collaboration, A. V. Artamonov *et al.*, *Study of the decay $K^+ \rightarrow \pi^+ \nu \bar{\nu}$ in the momentum region $140 < P_\pi < 199$ MeV/c*, Phys. Rev. D **79** (2009) 092004 [0903.0030].
- [106] P. S. B. Dev, R. N. Mohapatra, and Y. Zhang, *Revisiting supernova constraints on a light CP-even scalar*, JCAP **08** (2020) 003 [2005.00490].
- [107] **Particle Data Group** Collaboration, F. Takahashi *et al.*, *Review of Particle Physics*, Int. J. Mod. Phys. A **41** (2026) 2630011.
- [108] M. Fabbrichesi, E. Gabrielli, and G. Lanfranchi, *The Dark Photon*, [2005.01515].
- [109] J. H. Chang, R. Essig, and S. D. McDermott, *Revisiting Supernova 1987A Constraints on Dark Photons*, JHEP **01** (2017) 107 [1611.03864].
- [110] W. DeRocco, P. W. Graham, D. Kasen, G. Marques-Tavares, and S. Rajendran, *Observable signatures of dark photons from supernovae*, JHEP **02** (2019) 171 [1901.08596].
- [111] A. Sung, H. Tu, and M.-R. Wu, *New constraint from supernova explosions on light particles beyond the Standard Model*, Phys. Rev. D **99** (2019) 121305 [1903.07923].
- [112] **PandaX-II** Collaboration, J. Yang *et al.*, *Constraining self-interacting dark matter with the full dataset of PandaX-II*, Sci. China Phys. Mech. Astron. **64** (2021) 111062 [2104.14724].
- [113] M. Laine and M. Meyer, *Standard Model thermodynamics across the electroweak crossover*, J. Cosmol. Astropart. Phys. **2015** (2015) 035 [1503.04935].
- [114] M. D’Onofrio and K. Rummukainen, *The Standard Model cross-over on the lattice*, Phys. Rev. D **93** (2015) 025003 [1508.07161].
- [115] H. Wu and S. Zheng, *Scalar Dark Matter: Real vs Complex*, JHEP **03** (2017) 142 [1610.06292].
- [116] G. Krnjaic, *Probing Light Thermal Dark-Matter With a Higgs Portal Mediator*, Phys. Rev. D **94** (2016) 073009 [1512.04119].
- [117] S. Davidson, E. Nardi, and Y. Nir, *Leptogenesis*, Phys. Rept. **466** (2008) 105 [0802.2962].
- [118] A. Anisimov, D. Besak, and D. Bodeker, *Thermal production of relativistic Majorana neutrinos: Strong enhancement by multiple soft scattering*, JCAP **03** (2011) 042 [1012.3784].
- [119] J. Ghiglieri and M. Laine, *Neutrino dynamics below the electroweak crossover*, JCAP **07** (2016) 015 [1605.07720].

- [120] S. Biondini and J. Ghiglieri, *Freeze-in produced dark matter in the ultra-relativistic regime*, JCAP **03** (2021) 075 [2012.09083].
- [121] **HotQCD** Collaboration, A. Bazavov *et al.*, *Chiral crossover in QCD at zero and non-zero chemical potentials*, Phys. Lett. B **795** (2019) 15 [1812.08235].
- [122] S. Nadkarni, *Dimensional reduction in finite-temperature quantum chromodynamics. II*, Phys. Rev. D **38** (1988) 3287.
- [123] N. Landsman, *Limitations to dimensional reduction at high temperature*, Nucl. Phys. B **322** (1989) 498.
- [124] E. Braaten and A. Nieto, *Free energy of QCD at high temperature*, Phys. Rev. D **53** (1996) 3421 [hep-ph/9510408].
- [125] H. A. Weldon, *Covariant Calculations at Finite Temperature: The Relativistic Plasma*, Phys. Rev. D **26** (1982) 1394.
- [126] M. Karjalainen and J. Peisa, *Dimensionally reduced $U(1)$ + Higgs theory in the broken phase*, Z. Phys. C **76** (1997) 319 [hep-lat/9607023].
- [127] K. Kajantie, M. Karjalainen, M. Laine, and J. Peisa, *Masses and phase structure in the Ginzburg-Landau model*, Phys. Rev. B **57** (1998) 3011 [cond-mat/9704056].
- [128] J. O. Andersen, *3-D effective field theory for finite temperature scalar electrodynamics*, Phys. Rev. D **59** (1999) 065015 [hep-ph/9709418].
- [129] A. Ekstedt, P. Schicho, and T. V. I. Tenkanen, *DRalgo: A package for effective field theory approach for thermal phase transitions*, Comput. Phys. Commun. **288** (2023) 108725 [2205.08815].
- [130] F. Bernardo, R. G. Reinle, and P. Schicho, *Matching higher-dimensional operators at finite temperature for general models*, [2605.15176].
- [131] M. Chala, J. C. Criado, L. Gil, and J. L. Miras, *Higher-order-operator corrections to phase-transition parameters in dimensional reduction*, JHEP **10** (2024) 025 [2406.02667].
- [132] J. Fuentes-Martín, J. López Miras, and A. Moreno-Sánchez, *Matchotter: An Automated Tool for Dimensional Reduction at Finite Temperature*, [2604.21972].
- [133] J. Chakraborty, B. Siqueira Eduardo, S. Karmakar, and P. Schicho, *Finite-temperature operator basis on $\mathbb{R}^3 \times S^1$ for SMEFT*, [2605.02878].
- [134] S. Bandyopadhyay, J. Chakraborty, D. Dey, P. Schicho, and Tushar, *Higher-dimensional operators and Polyakov loop in hot Scalar QED from the heat kernel*, [2606.09779].
- [135] F. Bernardo, M. Chala, L. Gil, and P. Schicho, *Hard thermal contributions to phase transition observables at NNLO*, [2602.06962].
- [136] A. Ekstedt, O. Gould, and J. Löfgren, *Radiative first-order phase transitions to next-to-next-to-leading order*, Phys. Rev. D **106** (2022) 036012 [2205.07241].
- [137] O. Gould and T. V. I. Tenkanen, *Perturbative effective field theory expansions for cosmological phase transitions*, JHEP **01** (2024) 048 [2309.01672].

- [138] J. Hirvonen, *Intuitive method for constructing effective field theories*, [2205.02687].
- [139] M. Dine, R. G. Leigh, P. Huet, A. D. Linde, and D. A. Linde, *Comments on the electroweak phase transition*, Phys. Lett. B **283** (1992) 319 [hep-ph/9203201].
- [140] M. Dine, R. G. Leigh, P. Y. Huet, A. D. Linde, and D. A. Linde, *Towards the theory of the electroweak phase transition*, Phys. Rev. D **46** (1992) 550 [hep-ph/9203203].
- [141] J. Baacke and V. G. Kiselev, *One loop corrections to the bubble nucleation rate at finite temperature*, Phys. Rev. D **48** (1993) 5648 [hep-ph/9308273].
- [142] G. V. Dunne and H. Min, *Beyond the thin-wall approximation: Precise numerical computation of prefactors in false vacuum decay*, Phys. Rev. D **72** (2005) 125004 [hep-th/0511156].
- [143] A. Ekstedt, *Higher-order corrections to the bubble-nucleation rate at finite temperature*, Eur. Phys. J. C **82** (2022) 173 [2104.11804].
- [144] A. Ekstedt, *Convergence of the nucleation rate for first-order phase transitions*, Phys. Rev. D **106** (2022) 095026 [2205.05145].
- [145] M. Matteini, M. Nemevšek, Y. Shoji, and L. Ubaldi, *False vacuum decay rate from thin to thick walls*, JHEP **04** (2025) 120 [2404.17632].
- [146] V. Brdar, M. Finetti, M. Matteini, A. P. Morais, and M. Nemevšek, *PT2GWFinder: A Package for Cosmological First-Order Phase Transitions and Gravitational Waves*, [2505.04744].
- [147] A. Ekstedt, O. Gould, and J. Hirvonen, *BubbleDet: a Python package to compute functional determinants for bubble nucleation*, JHEP **12** (2023) 056 [2308.15652].
- [148] C. L. Wainwright, *CosmoTransitions: Computing cosmological phase transition temperatures and bubble profiles with multiple fields*, Comput. Phys. Commun. **183** (2012) 2006 [1109.4189].
- [149] V. Guada, M. Nemevšek, and M. Pintar, *FindBounce: Package for multi-field bounce actions*, Comput. Phys. Commun. **256** (2020) 107480 [2002.00881].
- [150] L. Bian, H. Wang, Y. Xiao, J.-C. Yang, J. M. Yang, and Y. Zhang, *Enhancing Phase Transition Calculations with Fitting and Neural Network*, [2510.10667].
- [151] S. Pascoli, S. Rosauero-Alcaraz, and M. Zandi, *Cosmological phase transitions: from particle physics to gravitational waves, semi-analytically*, [2602.02829].
- [152] C. Caprini *et al.*, *Detecting gravitational waves from cosmological phase transitions with LISA: an update*, JCAP **03** (2020) 024 [1910.13125].
- [153] P. Athron, L. Morris, and Z. Xu, *How robust are gravitational wave predictions from cosmological phase transitions?*, JCAP **05** (2024) 075 [2309.05474].
- [154] F. Giese, T. Konstandin, and J. van de Vis, *Model-independent energy budget of cosmological first-order phase transitions—A sound argument to go beyond the bag model*, JCAP **07** (2020) 057 [2004.06995].
- [155] F. Giese, T. Konstandin, K. Schmitz, and J. Van De Vis, *Model-independent energy budget for LISA*, JCAP **01** (2021) 072 [2010.09744].

- [156] A. Gynther and M. Vepsalainen, *Pressure of the standard model at high temperatures*, JHEP **01** (2006) 060 [hep-ph/0510375].
- [157] T. V. I. Tenkanen and J. van de Vis, *Speed of sound in cosmological phase transitions and effect on gravitational waves*, JHEP **08** (2022) 302 [2206.01130].
- [158] D. Croon, O. Gould, P. Schicho, T. V. I. Tenkanen, and G. White, *Theoretical uncertainties for cosmological first-order phase transitions*, JHEP **04** (2021) 055 [2009.10080].
- [159] M. Laine, *The Renormalized gauge coupling and nonperturbative tests of dimensional reduction*, JHEP **06** (1999) 020 [hep-ph/9903513].
- [160] A. H. Guth and E. J. Weinberg, *Cosmological Consequences of a First Order Phase Transition in the $SU(5)$ Grand Unified Model*, Phys. Rev. D **23** (1981) 876.
- [161] M. S. Turner, E. J. Weinberg, and L. M. Widrow, *Bubble nucleation in first order inflation and other cosmological phase transitions*, Phys. Rev. D **46** (1992) 2384.
- [162] K. Enqvist, J. Ignatius, K. Kajantie, and K. Rummukainen, *Nucleation and bubble growth in a first order cosmological electroweak phase transition*, Phys. Rev. D **45** (1992) 3415.
- [163] M. E. Carrington and J. I. Kapusta, *Dynamics of the electroweak phase transition*, Phys. Rev. D **47** (1993) 5304.
- [164] J. Ellis, M. Lewicki, and J. M. No, *On the Maximal Strength of a First-Order Electroweak Phase Transition and its Gravitational Wave Signal*, JCAP **04** (2019) 003 [1809.08242].
- [165] O. Gould, J. Kozaczuk, L. Niemi, M. J. Ramsey-Musolf, T. V. I. Tenkanen, and D. J. Weir, *Non-perturbative analysis of the gravitational waves from a first-order electroweak phase transition*, Phys. Rev. D **100** (2019) 115024 [1903.11604].
- [166] **LISA Cosmology Working Group** Collaboration, C. Caprini, R. Jinno, M. Lewicki, *et al.*, *Gravitational waves from first-order phase transitions in LISA: reconstruction pipeline and physics interpretation*, JCAP **10** (2024) 020 [2403.03723].
- [167] S. J. Huber and T. Konstandin, *Gravitational Wave Production by Collisions: More Bubbles*, JCAP **09** (2008) 022 [0806.1828].
- [168] W.-Y. Ai, B. Laurent, and J. van de Vis, *Model-independent bubble wall velocities in local thermal equilibrium*, JCAP **07** (2023) 002 [2303.10171].
- [169] W.-Y. Ai, B. Laurent, and J. van de Vis, *Bounds on the bubble wall velocity*, JHEP **02** (2025) 119 [2411.13641].
- [170] M. Eriksson and M. Laine, *Entropy production at electroweak bubble walls from scalar field fluctuations*, JCAP **09** (2025) 027 [2507.07755].
- [171] J. R. Espinosa, T. Konstandin, J. M. No, and G. Servant, *Energy Budget of Cosmological First-order Phase Transitions*, JCAP **06** (2010) 028 [1004.4187].
- [172] R. Jinno, T. Konstandin, H. Rubira, and I. Stomberg, *Higgsless simulations of cosmological phase transitions and gravitational waves*, JCAP **02** (2023) 011 [2209.04369].

- [173] B. Laurent and J. M. Cline, *First principles determination of bubble wall velocity*, Phys. Rev. D **106** (2022) 023501 [2204.13120].
- [174] S. De Curtis, L. D. Rose, A. Guiggiani, Á. G. Muyor, and G. Panico, *Bubble wall dynamics at the electroweak phase transition*, JHEP **03** (2022) 163 [2201.08220].
- [175] S. De Curtis, L. Delle Rose, A. Guiggiani, Á. Gil Muyor, and G. Panico, *Collision integrals for cosmological phase transitions*, JHEP **05** (2023) 194 [2303.05846].
- [176] S. De Curtis, L. Delle Rose, A. Guiggiani, Á. Gil Muyor, and G. Panico, *Non-linearities in cosmological bubble wall dynamics*, JHEP **05** (2024) 009 [2401.13522].
- [177] A. Ekstedt, O. Gould, J. Hirvonen, *et al.*, *How fast does the WallGo? A package for computing wall velocities in first-order phase transitions*, JHEP **04** (2025) 101 [2411.04970].
- [178] J. van de Vis, P. Schicho, L. Niemi, B. Laurent, J. Hirvonen, and O. Gould, *WallGo investigates: Theoretical uncertainties in the bubble wall velocity*, JHEP **04** (2026) 041 [2510.27691].
- [179] P. J. Steinhardt, *Relativistic Detonation Waves and Bubble Growth in False Vacuum Decay*, Phys. Rev. D **25** (1982) 2074.
- [180] C. Caprini and D. G. Figueroa, *Cosmological Backgrounds of Gravitational Waves*, Class. Quant. Grav. **35** (2018) 163001 [1801.04268].
- [181] M. Hindmarsh, S. J. Huber, K. Rummukainen, and D. J. Weir, *Numerical simulations of acoustically generated gravitational waves at a first order phase transition*, Phys. Rev. D **92** (2015) 123009 [1504.03291].
- [182] M. Hindmarsh, S. J. Huber, K. Rummukainen, and D. J. Weir, *Shape of the acoustic gravitational wave power spectrum from a first order phase transition*, Phys. Rev. D **96** (2017) 103520 [1704.05871].
- [183] C. Caprini, R. Durrer, and G. Servant, *The stochastic gravitational wave background from turbulence and magnetic fields generated by a first-order phase transition*, JCAP **12** (2009) 024 [0909.0622].
- [184] R. Jinno, B. Shakya, and J. van de Vis, *Gravitational Waves from Feebly Interacting Particles in a First Order Phase Transition*, Phys. Rev. Lett. **136** (2026) 131002 [2211.06405].
- [185] M. Escudero, G. Jackson, M. Laine, and S. Sandner, *Fast and flexible neutrino decoupling. Part I. The Standard Model*, JCAP **02** (2026) 046 [2511.04747].
- [186] E. W. Kolb and M. S. Turner, *The Early Universe*, vol. 69. Taylor and Francis, 5, 2019.
- [187] J. Ellis, M. Lewicki, and J. M. No, *Gravitational waves from first-order cosmological phase transitions: lifetime of the sound wave source*, JCAP **07** (2020) 050 [2003.07360].
- [188] H.-K. Guo, K. Sinha, D. Vagie, and G. White, *Phase Transitions in an Expanding Universe: Stochastic Gravitational Waves in Standard and Non-Standard Histories*, JCAP **01** (2021) 001 [2007.08537].
- [189] A. Megevand and S. Ramirez, *Bubble nucleation and growth in very strong cosmological phase transitions*, Nucl. Phys. B **919** (2017) 74 [1611.05853].

- [190] P. Athron, C. Balázs, A. Fowlie, L. Morris, and L. Wu, *Cosmological phase transitions: From perturbative particle physics to gravitational waves*, Prog. Part. Nucl. Phys. **135** (2024) 104094 [2305.02357].
- [191] J. Matuszak and C. Tasillo, *TransitionListener v2.0 – Robust gravitational wave predictions for cosmological phase transitions*, [2605.15259].
- [192] M. Hindmarsh and M. Hijazi, *Gravitational waves from first order cosmological phase transitions in the Sound Shell Model*, JCAP **12** (2019) 062 [1909.10040].
- [193] F. Ertas, F. Kahlhoefer, and C. Tasillo, *Turn up the volume: listening to phase transitions in hot dark sectors*, JCAP **02** (2022) 014 [2109.06208].
- [194] C. Caprini, R. Jinno, T. Konstandin, A. Roper Pol, H. Rubira, and I. Stomberg, *Gravitational waves from first-order phase transitions: from weak to strong*, JHEP **07** (2025) 217 [2409.03651].
- [195] A. Roper Pol, A. Neronov, C. Caprini, T. Boyer, and D. Semikoz, *LISA and γ -ray telescopes as multi-messenger probes of a first-order cosmological phase transition*, Astron. Astrophys. **708** (2026) A337 [2307.10744].
- [196] C. Caprini, R. Durrer, T. Konstandin, and G. Servant, *General Properties of the Gravitational Wave Spectrum from Phase Transitions*, Phys. Rev. D **79** (2009) 083519 [0901.1661].
- [197] T. R. Slatyer, *Indirect dark matter signatures in the cosmic dark ages. I. Generalizing the bound on s-wave dark matter annihilation from Planck results*, Phys. Rev. D **93** (2016) 023527 [1506.03811].
- [198] S. Galli, F. Iocco, G. Bertone, and A. Melchiorri, *CMB constraints on Dark Matter models with large annihilation cross-section*, Phys. Rev. D **80** (2009) 023505 [0905.0003].
- [199] T. R. Slatyer, N. Padmanabhan, and D. P. Finkbeiner, *CMB Constraints on WIMP Annihilation: Energy Absorption During the Recombination Epoch*, Phys. Rev. D **80** (2009) 043526 [0906.1197].
- [200] T. Bringmann, F. Kahlhoefer, K. Schmidt-Hoberg, and P. Walia, *Strong constraints on self-interacting dark matter with light mediators*, Phys. Rev. Lett. **118** (2017) 141802 [1612.00845].
- [201] J. Hisano, S. Matsumoto, M. Nagai, O. Saito, and M. Senami, *Non-perturbative effect on thermal relic abundance of dark matter*, Phys. Lett. B **646** (2007) 34 [hep-ph/0610249].
- [202] J. Zavala, M. Vogelsberger, and S. D. M. White, *Relic density and CMB constraints on dark matter annihilation with Sommerfeld enhancement*, Phys. Rev. D **81** (2010) 083502 [0910.5221].
- [203] M. Beneke, C. Hellmann, and P. Ruiz-Femenia, *Heavy neutralino relic abundance with Sommerfeld enhancements - a study of pMSSM scenarios*, JHEP **03** (2015) 162 [1411.6930].
- [204] I. Baldes, F. Calore, K. Petraki, V. Poireau, and N. L. Rodd, *Indirect searches for dark matter bound state formation and level transitions*, SciPost Phys. **9** (2020) 068 [2007.13787].
- [205] S. Biondini, J. Bollig, and S. Vogl, *Indirect detection of dark matter with (pseudo)-scalar interactions*, JHEP **04** (2024) 050 [2308.14594].

- [206] P.-H. Gu, M. Lindner, U. Sarkar, and X. Zhang, *WIMP Dark Matter and Baryogenesis*, Phys. Rev. D **83** (2011) 055008 [1009.2690].
- [207] J. Shelton and K. M. Zurek, *Darkogenesis: A baryon asymmetry from the dark matter sector*, Phys. Rev. D **82** (2010) 123512 [1008.1997].
- [208] M. L. Graesser, I. M. Shoemaker, and L. Vecchi, *Asymmetric WIMP dark matter*, JHEP **10** (2011) 110 [1103.2771].
- [209] P. Gondolo and G. Gelmini, *Cosmic abundances of stable particles: Improved analysis*, Nucl. Phys. **B360** (1991) 145.
- [210] A. Sommerfeld, *Über die Beugung und Bremsung der Elektronen*, Ann. Phys.(1931) **403** (1931) .
- [211] R. Iengo, *Sommerfeld enhancement: General results from field theory diagrams*, JHEP **05** (2009) 024 [0902.0688].
- [212] S. Cassel, *Sommerfeld factor for arbitrary partial wave processes*, J. Phys. **G37** (2010) 105009 [0903.5307].
- [213] B. von Harling and K. Petraki, *Bound-state formation for thermal relic dark matter and unitarity*, JCAP **1412** (2014) 033 [1407.7874].
- [214] K. Petraki, M. Postma, and J. de Vries, *Radiative bound-state-formation cross-sections for dark matter interacting via a Yukawa potential*, JHEP **04** (2017) 077 [1611.01394].
- [215] S. Biondini, N. Brambilla, G. Qerimi, and A. Vairo, *Effective field theories for dark matter pairs in the early universe: cross sections and widths*, JHEP **07** (2023) 006 [2304.00113].
- [216] S. Biondini and M. Laine, *Thermal dark matter co-annihilating with a strongly interacting scalar*, JHEP **2018** (2018) 72 [1801.05821].
- [217] T. Binder, K. Mukaida, and K. Petraki, *Rapid bound-state formation of Dark Matter in the Early Universe*, Phys. Rev. Lett. **124** (2020) 161102 [1910.11288].
- [218] T. Binder, B. Blobel, J. Harz, and K. Mukaida, *Dark Matter bound-state formation at higher order: A non-equilibrium quantum field theory approach*, arXiv (2020) [2002.07145].
- [219] S. Biondini, N. Brambilla, A. Dashko, G. Qerimi, and A. Vairo, *Effective field theories for dark matter pairs in the early universe: Debye mass effects*, JHEP **04** (2025) 091 [2501.03327].
- [220] J. Ellis, F. Luo, and K. A. Olive, *Gluino Coannihilation Revisited*, JHEP **09** (2015) 127 [1503.07142].
- [221] P. A. M. Dirac, *On the Annihilation of Electrons and Protons*, Proc. Cambridge Phil. Soc. **26** (1930) 361.
- [222] K. Petraki and R. R. Volkas, *Review of asymmetric dark matter*, Int. J. Mod. Phys. A **28** (2013) 1330028 [1305.4939].
- [223] K. M. Zurek, *Asymmetric Dark Matter: Theories, Signatures, and Constraints*, Phys. Rept. **537** (2014) 91 [1308.0338].

- [224] G. B. Gelmini, J.-H. Huh, and T. Rehgagen, *Asymmetric dark matter annihilation as a test of non-standard cosmologies*, JCAP **08** (2013) 003 [1304.3679].
- [225] L. Niemi, P. Schicho, and T. V. I. Tenkanen, *Singlet-assisted electroweak phase transition at two loops*, Phys. Rev. D **103** (2021) 115035 [2103.07467].
- [226] G. Steigman, B. Dasgupta, and J. F. Beacom, *Precise Relic WIMP Abundance and its Impact on Searches for Dark Matter Annihilation*, Phys. Rev. D **86** (2012) 023506 [1204.3622].
- [227] P. Navarrete, R. Paatelainen, K. Seppänen, and T. V. I. Tenkanen, *Cosmological phase transitions without high-temperature expansions*, [2507.07014].
- [228] L. Niemi and T. V. I. Tenkanen, *Investigating two-loop effects for first-order electroweak phase transitions*, Phys. Rev. D **111** (2025) 075034 [2408.15912].
- [229] A. Mitridate, D. Wright, R. von Eckardstein, *et al.*, *PTArcade*, [2306.16377].
- [230] W. G. Lamb, S. R. Taylor, and R. van Haasteren, *Rapid refitting techniques for Bayesian spectral characterization of the gravitational wave background using pulsar timing arrays*, Phys. Rev. D **108** (2023) 103019 [2303.15442].
- [231] M. Lewicki, M. Merchand, L. Sagunski, P. Schicho, and D. Schmitt, *Impact of theoretical uncertainties on model parameter reconstruction from GW signals sourced by cosmological phase transitions*, Phys. Rev. D **110** (2024) 023538 [2403.03769].
- [232] S. S. AbdusSalam *et al.*, *Simple and statistically sound recommendations for analysing physical theories*, Rept. Prog. Phys. **85** (2022) 052201 [2012.09874].
- [233] M. Breitbach, J. Kopp, E. Madge, T. Opferkuch, and P. Schwaller, *Dark, Cold, and Noisy: Constraining Secluded Hidden Sectors with Gravitational Waves*, JCAP **07** (2019) 007 [1811.11175].
- [234] J. C. Collins and J. A. M. Vermaseren, *Axodraw Version 2*, arXiv (2016) [1606.01177].
- [235] G. 't Hooft and M. J. G. Veltman, *Scalar One Loop Integrals*, Nucl. Phys. B **153** (1979) 365.
- [236] M. Laine, *Exact relation of lattice and continuum parameters in three-dimensional SU(2) + Higgs theories*, Nucl. Phys. B **451** (1995) 484 [9504001].
- [237] M. Laine, M. Meyer, and G. Nardini, *Thermal phase transition with full 2-loop effective potential*, Nucl. Phys. B **920** (2017) 565 [1702.07479].
- [238] S. Coleman and E. Weinberg, *Radiative Corrections as the Origin of Spontaneous Symmetry Breaking*, Phys. Rev. D **7** (1973) 1888 [0507214].
- [239] S. Biondini, P. Schicho, and T. V. I. Tenkanen, *Strong electroweak phase transition in t-channel simplified dark matter models*, JCAP **10** (2022) 044 [2207.12207].
- [240] M. Laine, P. Schicho, and Y. Schröder, *A QCD Debye mass in a broad temperature range*, Phys. Rev. D **101** (2020) 023532 [1911.09123].
- [241] Z. Capatti, V. Hirschi, A. Kurkela, *et al.*, *In preparation*. 2026.
- [242] G. T. Bodwin, E. Braaten, and G. P. Lepage, *Rigorous QCD analysis of inclusive annihilation and production of heavy quarkonium*, Phys. Rev. D **51** (1995) 1125 [hep-ph/9407339].